

Copyright © and Moral Rights for this thesis and, where applicable, any accompanying data are retained by the author and/or other copyright owners. A copy can be downloaded for personal non-commercial research or study, without prior permission or charge. This thesis and the accompanying data cannot be reproduced or quoted extensively from without first obtaining permission in writing from the copyright holder/s. The content of the thesis and accompanying research data (where applicable) must not be changed in any way or sold commercially in any format or medium without the formal permission of the copyright holder/s.

When referring to this thesis and any accompanying data, full bibliographic details must be given, e.g. Hage, S. (2019) "Turbidity current processes and products in the fjords of British Columbia, Canada", University of Southampton, School of Ocean and Earth Sciences, PhD Thesis, 0-142.

UNIVERSITY OF SOUTHAMPTON
FACULTY OF NATURAL AND ENVIRONMENTAL SCIENCES
SCHOOL OF OCEAN AND EARTH SCIENCES

**Turbidity current processes and
products in the fjords of British
Columbia (Canada)**

by
SOPHIE HAGE

A thesis submitted for the degree of Doctor of Philosophy

November 2019

UNIVERSITY OF SOUTHAMPTON
FACULTY OF NATURAL AND ENVIRONMENTAL SCIENCES
SCHOOL OF OCEAN AND EARTH SCIENCES

Doctor of Philosophy

**Turbidity current processes and products in the fjords of British Columbia
(Canada)**

by SOPHIE HAGE

ABSTRACT

Turbidity currents are volumetrically the most important process to transfer land-derived sediments offshore. Fast-moving, powerful turbidity currents can carve submarine canyons that rival some of the largest canyons on land. These submarine canyons feed deep-sea fans, which are the largest sediment accumulations on Earth. Such huge sediment accumulations sequester organic carbon across geologic times and are thus thought to play a role in the global carbon cycle. Additionally, turbidity currents pose a hazard for the ever-expanding seafloor infrastructure network that underpins our energy supply and global communication. Despite the global significance of turbidity currents and their deposits, the link between flow processes (e.g. triggering mechanisms, seafloor erosion) and depositional products is still poorly constrained. This is due to the difficulty in monitoring flows and sampling deposits directly resulting from flows. In this thesis I present direct measurements of turbidity currents and their deposits in two fjords of British Columbia (Canada), named Howe Sound and Bute Inlet. Glacier-fed rivers flow into both fjord heads; hence, these are excellent sites to study the transport and fate of particles from land to sea. This thesis uses these new measurements to answer three research questions.

First *how do extremely dilute river plumes generate turbidity currents?* The current paradigm is that rivers need to exceed a specific sediment concentration (e.g. 1 g/L) to directly generate turbidity currents at their mouths. Chapter 2 shows that rivers with extremely dilute plumes (0.07 g/L) can generate turbidity currents under certain conditions, e.g. low tide, relatively high river discharge, a turbidity maximum being forced out on a steep delta front and the availability of loose-packed fine sediment on the seabed. These results were found using direct observations of the Squamish river plume flowing into Howe Sound. This study suggests that a much wider range of rivers than previously thought can directly generate turbidity currents on our planet. The possibility of triggering turbidity currents by a much wider selection of rivers has strong implications for understanding the fate of terrestrial particles (including organic carbon and pollutants) into the sea.

Second, *what is the diagnostic deposit facies/architecture resulting from crescentic bed-forms formed by supercritical turbidity currents?* Modern observations show that submarine channels can be sculpted by supercritical (i.e. thin and fast) turbidity currents. Such flows are likely to produce upstream-migrating bedforms with a crescentic planform. The depositional signature of such bedforms is currently only constrained by outcrop observations and experimental models. These experiment and outcrop studies indicate different sedimentary structures form from supercritical flows. In order to reconcile this apparent discrepancy, Chapter 3 presents the first observations that directly link supercritical (i.e. thin and fast) turbidity currents in the real-world with their deposits. To establish the link between flow process and resulting sedimentary deposit, I combine seafloor flow measurements, time-lapse seabed mapping and sediment cores. Using these data collected in a submarine channel on the Squamish delta (Howe Sound), I show that supercritical turbidity currents initially produce back-stepping beds of sand, as seen in experimental studies. However, the field data shows how these back-stepping beds are subsequently partially eroded by later flows, resulting in the scours filled of massive sands that are commonly observed in the depositional record. Accurate recognition of supercritical flow deposits in the depositional record is important for oil and gas reservoir characterisation, past environmental reconstruction and a general understanding of sedimentary systems.

Third, *how is young terrestrial organic carbon preserved in turbidites?* Efficient burial of terrestrial organic carbon in marine sediments leads to a net CO₂ removal from the atmosphere, thus regulating climate over geological timescale. Existing studies suggest that most organic carbon is buried in association with fine sediments because clay minerals are able to bind organic matter and shield it from degradation. In contrast with these studies, Chapter 4 shows that young, coarse woody debris accounts for the majority (>70 %) of terrestrial organic carbon sequestered in sandy turbidity current deposits. These coarse organic-rich layers are rapidly buried under turbidity current mud caps, reducing their direct exposure to oxygen and thereby increasing burial efficiency. These findings are based on data collected in the sandy submarine channel of Bute Inlet. The data consist of 1) flow observations, 2) deposit sampling, 3) analysis of the composition and ages of the organic carbon contained within these deposits. These results provide important insights into the effect of hydrodynamic sorting of young terrestrial organic carbon by turbidity currents. Turbidity currents dominate sediment transport in submarine environments; therefore these results suggest that previous global organic carbon burial budgets may have been underestimated.

Finally I conclude that observations, particularly from the deep sea, are needed to test whether these scientific findings collected in fjords are applicable to the much larger deep-sea turbidity current systems.

Contents

Abstract	iii
Contents	v
List of Figures	ix
List of Tables	xi
Declaration of Authorship	xiii
Publications	xv
Acknowledgements	xvii
1 Introduction	1
1.1 Rationale	1
1.2 Aims and structure of the thesis	2
1.3 Why is there a gap in the link between turbidity current processes and their products: a brief historical timeline	4
1.4 Why study fjords to resolve the knowledge gap between turbidity current processes and products?	7
1.4.1 Focus on two British Columbia fjords: Howe Sound and Bute Inlet	7
1.4.2 Fjords are natural laboratories to study the connection of rivers with offshore sediment transport	10
1.4.3 River-fed fjords contain highly dynamic submarine channels re-worked by frequent turbidity currents	10
1.4.4 Fjords are globally significant for organic carbon burial	11
1.4.5 Fjords provide insights into larger deep ocean systems	11
2 Direct monitoring reveals initiation of turbidity currents from extremely dilute river plumes	15
2.1 Abstract	16
2.2 Introduction	16
2.2.1 Aims	18
2.3 Setting of field measurements	18
2.4 Methods	20
2.4.1 Turbidity current velocity and river-plume concentrations	20
2.4.2 Salinity, temperature and suspended sediment concentrations	22
2.4.3 Repeated water column imaging and seafloor mapping	22

2.5	Results	24
2.5.1	Water column structure and horizontal density gradients	24
2.5.2	Observations of the 15 th June turbidity current	25
2.5.3	Summary	25
2.6	Discussion	27
2.6.1	A reduced threshold sediment concentration for generating turbidity currents	27
2.6.2	How do dilute river plumes generate turbidity currents?	27
2.6.3	Global implications for more frequent and widespread turbidity currents	28
2.7	Conclusion	28
2.8	Acknowledgements	29
2.9	Supplementary material	30
3	How to recognize crescentic bedforms formed by supercritical turbidity currents in the geologic record: Insights from active submarine channels	35
3.1	Abstract	36
3.2	Introduction	36
3.2.1	Aims	37
3.3	Study site and Methods	37
3.3.1	Flow and Seafloor Observations	40
3.3.2	Sedimentary Deposit Observations	42
3.4	Results	42
3.4.1	Flow Monitoring and Seafloor Morphological Change	42
3.4.2	Deposit Geometry (Seafloor Difference Maps) and Facies (Cores)	43
3.5	Discussion	45
3.5.1	Comparison with Existing Models	45
3.5.2	Recognition of Supercritical Flow Deposits in the Geologic Record	46
3.6	Acknowledgements	49
3.7	Supplementary movies	49
4	Efficient burial of young terrestrial organic carbon by submarine turbidity currents	51
4.1	Abstract	51
4.2	Introduction	52
4.3	Results	53
4.3.1	River and turbidite sampling in Bute Inlet	53
4.3.2	Organic carbon in rivers and turbidites	55
4.4	Abundance of woody debris in turbidites	57
4.5	Discussion	58
4.6	Materials and methods	60
4.6.1	Separation of organic carbon mixtures by ramped oxidation	60
4.6.2	Identification of organic carbon types and calculation of their proportions for the turbidite	61
4.6.3	Comparison of TOC fluxes between sandy channel and fines outside the channel	62

5	Conclusions and research perspectives	73
5.1	How do extremely dilute river plumes generate turbidity currents?	73
5.1.1	Limitations and future research	74
5.1.2	Test site	74
5.2	What are the diagnostic deposits of crescentic bedforms formed by supercritical turbidity currents?	75
5.2.1	Limitations and future research	75
5.2.2	Test site	76
5.3	How is young terrestrial organic carbon preserved in turbidites?	76
5.3.1	Limitations and future research	76
5.3.2	Test sites	77
5.4	Broader research perspectives on turbidity current processes and products	77
A	Appendix	81
A.1	Field campaigns	81
A.1.1	Squamish 2015	81
A.1.1.1	Moving vessel Heron	82
A.1.1.2	Stationary Vessel RV Strickland	82
A.1.2	Squamish 2016 (Geological Survey of Canada cruise 2016003PGC)	83
A.1.3	Bute Inlet 2016 (Geological Survey of Canada cruise 2016003PGC and 2016007PGC)	91
A.1.4	Bute Inlet October 2017 (Geological Survey of Canada cruise 2017005PGC)	95
A.2	ADCP processing	96
A.2.1	General principle	96
A.2.2	Limitations and corrections	97
A.2.3	Sediment concentration inversion	99
A.3	Procedure for ADCP implicit inversion into sediment concentration	100
A.3.1	Raw backscatter to voltage \mathbf{V}	100
A.3.2	Range to the transceiver \mathbf{r}	100
A.3.3	Near-field correction factor ϕ	101
A.3.4	Backscatter properties of sediment \mathbf{K}_s	101
A.3.4.1	Creation of a normalised frequency distribution of grain size diameter f	101
A.3.4.2	Creation of a form function and scattering cross-section for all grain sizes f_{fa}	102
A.3.5	Instrument-specific constant K_t	103
A.3.6	Attenuation of sound due to water α_t	103
A.3.7	Attenuation constant ξ	104
A.3.7.1	calculation of ξ_{viscous}	104
A.3.7.2	calculation of ξ_{scatter}	105

List of Figures

1.1	Figure 1.1: Lake Geneva bathymetry maps in 1885 and 2012	5
1.2	Figure 1.2: The Bouma Sequence	6
1.3	Figure 1.3: Locatiton of Howe Sound and Bute Inlet	8
1.4	Figure 1.4: Bathymetry maps of Howe Sound and Bute Inlet	9
1.5	Figure 1.5: Seafloor features at different scales	13
2.1	Figure 2.1: Mechanisms triggering turbidity currents at river mouths . . .	17
2.2	Figure 2.2: Setting and field deployment	19
2.3	Figure 2.3: ADCP results	21
2.4	Figure 2.4: Density gradient profiles	23
2.5	Figure 2.5: Water column transects	24
2.6	Figure 2.6: Summary sketches	26
2.7	Figure 2.7: ADCP inversion results	30
2.8	Figure 2.8: Calibration of the OBS probe	31
2.9	Figure 2.9: Grain size distributions	31
2.10	Figure 2.10: Salinity and suspended sediment profiles	32
2.11	Figure 2.11: exemples of water density profiles	33
3.1	Figure 3.1: Study site and field deployment	38
3.2	Figure 3.2: Squamish river discharge	39
3.3	Figure 3.3: Field deployment	41
3.4	Figure 3.4: Observations of a turbidity current	43
3.5	Figure 3.5: Seafloor stratigraphy evolution	44
3.6	Figure 3.6: Crescentic bedform deposits	45
3.7	Figure 3.7: Summary schematic	47
4.1	Figure 4.1: Study site and materials	54
4.2	Figure 4.2: TOC vs $\delta^{13}\text{C}$ and grain size distributions	56
4.3	Figure 4.3: Ramped oxidation results	57
4.4	Figure 4.4: Summary	58
4.5	Figure 4.5: TOC vs TC	64
4.6	Figure 4.6: Grain size distributions	64
4.7	Figure 4.7: Identification of organic carbon types	65
4.8	Figure 4.8: Grain size distributions for box core samples	66
4.9	Figure 4.9: Additional Ramped Oxidation data	67
4.10	Figure 4.10: Bulk measurements on turbidite samples	68
A.1	Figure A1: Squamish field experiment (June 2015)	82
A.2	Figure A2: Squamish core 1	84

A.3	Figure A3: Squamish core 2	85
A.4	Figure A4: Squamish core 3	86
A.5	Figure A5: Squamish core 4	87
A.6	Figure A6: Squamish core 5	88
A.7	Figure A7: Squamish core 6	89
A.8	Figure A8: Squamish core 7	90
A.9	Figure A9: Squamish cores 8 and 9	91
A.10	Figure A10: Bute core 1	92
A.11	Figure A11: Bute core 2	93
A.12	Figure A12: Bute core 3	93
A.13	Figure A13: Bute core 4	94
A.14	Figure A14: Bute core 5	94
A.15	Figure A15: River sample locations	95
A.16	Figure A16: ADCP schematic	96
A.17	Figure A17: ADCP processing chart	97
A.18	Figure A18: ADCP backscatter results (Squamish June 2015)	98

List of Tables

2.1	Table 2.1: water and sediment samples collected in the Squamish river mouth	32
2.2	Table 2.2: Propoerties of the monitored turbidity current	34
3.1	Table 3.1: Flow properties and seabed changes at Squamish	40
3.2	Table 3.2: Instrument specifications	41
3.3	Table 3.3: Comparison with outcrops	48
4.1	Table 4.1: TOC burial estimations	59
4.2	Table 4.2: OC types budget calculations	62
4.3	Table 4.3: Box cores samples: metadata and measurements (part 1) . . .	70
4.4	Table 4.4: Box cores samples: metadata and measurements (part 2) . . .	71
4.5	Table 4.5: River samples: metadata and measurements	72

Declaration of Authorship

I, Sophie Hage declare that this thesis and the work presented in it are my own and has been generated by me as the result of my own original research.

Turbidity current processes and products in the fjords of British Columbia (Canada)

I confirm that:

1. This work was done mainly while in candidature for a research degree at this University;
2. Where any part of this thesis has previously been submitted for a degree or any other qualification at this University or any other institution, this has been clearly stated;
3. Where I have consulted the published work of others, this is always clearly attributed;
4. Where I have quoted from the work of others, the source is always given. With the exception of such quotations, this thesis is entirely my own work;
5. I have acknowledged all main sources of help;
6. Where the thesis is based on work done by myself jointly with others, I have made clear exactly what was done by others and what I have contributed myself;
7. Parts of this work has or will be published in peer-reviewed scientific journals: see "Publication" section

Sophie Hage

November 2019

Publications

Journal publications arising from this thesis

*Note: * indicates submitted manuscripts*

Hage, S., Cartigny, M. J. B., Clare, M. A., Sumner, E. J., Vendettuoli, D., Hughes Clarke, J. E., Hubbard, S. M., Talling, P. J., Lintern, G. D., Stacey, C. D., Englert, R. G., Vardy, M. E., Hunt, J. E., Yokokawa, M., Parsons, D. R., Hizzett, J. L., Azpiroz-Zabala, M., Vellinga, A. J. (2018). How to recognize crescentic bedforms formed by supercritical turbidity currents in the geologic record: Insights from active submarine channels. *Geology* 46(6): 563-566. <http://dx.doi.org/10.1130/G40095.1>

Hage, S., Cartigny, M.J.B., Clare, M.A., Sumner E.J., Hughes Clarke, J.E., Vardy, M.E., Talling, P.J., Lintern D.G., Simmons, S.M., Vellinga, A. J., Silva Jacinto, R., Vellinga, A. J., Allin, J.R, Azpiroz-Zabala, M., Gales, J.A., Hizzett, J. L, Hunt, J. E., Mozzatto, A., Parsons, D. R., Pope, E.L., Stacey, C.D., Symons, W.O., Vardy, M.E., Watts, M. (2019). Direct monitoring reveals triggering of turbidity currents by extremely dilute river plumes. *Geophysical Research Letters* <https://doi.org/10.1029/2019GL084526>

* **Hage, S.**, Galy, V., Cartigny, M. J. B., Acikalin, S., Clare, M. A., Grocke, D.R., Hilton, R.G., Hunt, J.E., Lintern, D.G., McGhee, C.A., Parsons, D. R., Stacey, C.D., Sumner, E.J., Talling, P. J. (in review in *Geology*). Efficient preservation of young terrestrial organic carbon by submarine turbidity currents.

Other Journal publications

Hage, S., Hubert-Ferrari, A., Lamair, L., Avsar, U., El Ouahabi, M., Van Daele, M., Boulvain F., Ali Bahri, M., Seret, A., Plenevaux, A. (2017). Flow dynamics at the origin of thin clayey sand lacustrine turbidites: Examples from Lake Hazar, Turkey. *Sedimentology* (64), 1929-1956.

Vendettuoli, D., Clare, M.A., Clarke, J.H., Vellinga, A., Hizzett, J., **Hage, S.**, Cartigny, M.J.B., Talling, P.J., Waltham, D., Hubbard, S.M. and Stacey, C. (2019). Daily

bathymetric surveys document how stratigraphy is built and its extreme incompleteness in submarine channels. *Earth and Planetary Science Letters*, 515, pp.231-247.

Acknowledgements

I'd like to thank my supervisors Matthieu Cartigny, Michael Clare, Esther Sumner and Peter Talling who all gave me more guidance and support than I could ever have wished for. Matthieu, thank you for believing in me and for giving me the opportunity to start a Phd at NOCS. Thank you also for your patience (especially on my start with Matlab) and for showing endless motivation for all the data sets I've wanted to work with. Mike, thank you for your countless support and dedication in all the steps of my Phd. Thank you for organising the "Sed gatherings/coffee/pub" which gave me the chance to grow scientifically and socially. Esther, you are a "lady scientist model" to me. Thank you for your encouragements and support as a scientist and as a person. Pete, you often made me venture to the edge of my scientific limits, thank you for the trust you placed in me.

Special thanks go to Valier Galy who dedicated with passion a lot of his time teaching me the fascinating world of Geochemistry during my 3 month internship at the Woods Hole Oceanographic Institution. Thank you Valier for all your advices and support even after my time at WHOI.

Thank you to my examiners Christopher Pearce and Michi Strasser for assessing my thesis and for a very enjoyable viva. I acknowledge the funding resources of my PhD project: ExxonMobil and the Graduate School of the National Oceanography Centre Southampton. I also thank Durham University and the International Association of Sedimentologists for additional financial support.

I am extremely grateful to the fruitful discussions I had with Steve Hubbard, John Hughes Clarke, Gwyn Lintern, Cooper Stacey, Peter Neeland and Mark Vardy. Thank you to my panel chair Justin Dix who kept track of my Phd journey with dedication. Big thanks also to the long list of co-authors and colleagues from the UK, Canada, USA, France, Japan. I acknowledge the captains and crews of the research vessels I've had the chance to sail with: RV Strickland, RV Heron and Canadian Coast Guard Ship Vector. Thank you to the WHOI and NOSAMS team for their help and support during my internship: Mary Lardie, Al Gagnon, Carl Johnson, Ann McNichol.

A big thank you to my colleagues (or rather friends) who have closely followed my thesis evolution and who I shared amazing sea/conference/science time with: the gang Mariabala, Age and Jamie, as well as Daniela and Maarten.

I could not have gone through all the ups and downs of a Phd without the true friendship and love given by my NOCS girls, the "superwomen" Adeline, Aude, Delphine, Maria. Girls, although we don't share the same science interests, you have formed a pillar of my Phd thesis. Massive thanks also go to my friends Dada, Jay and Marla.

Je voudrais remercier Aurélia Hubert-Ferrari, ma promotrice de mémoire en géographie à l'ULiège, qui m'a donné gout à la sédimentologie et encouragée dans la voie d'une thèse de doctorat. Merci à mes amis belges qui ne m'ont jamais oubliée malgré la distance, et qui ont parfois même traversé la Manche pour me rendre visite: Gauthier mon cher beauf', Anne, Cassi, mes Cécile, Martial, Mél', Manon, Sarah, Tamtam, et j'en passe! Merci aussi à Johan, un soutien particulièrement précieux durant la fin de ma thèse.

Enfin, merci à ma famille à qui je dois tout. Mamy, Papy, merci d'avoir toujours été présents et intéressés par tout ce que j'entreprends. Maman, Papa, vous êtes des parents en or, toujours prêts à me soutenir. Merci pour vos messages, appels et voyages réguliers lors de mon aventure doctorale aux 4 coins du globe. Christelle, voilà que je te rejoins probablement dans le titre de Dr Hage... pour semer davantage la confusion chez les gens! Merci, L'autre. Je suis fière de ce que nous, "les jumelles", avons accompli séparément tout en restant toujours liées.



My first memory as a phd student (June 2015): a long hike with Esther Sumner to see the Squamish River plume flowing into Howe Sound, British Columbia.



"Million dollar view" of the head of Bute Inlet from the CCGS Vector, British Columbia, Canada (October 2016). Photo © Matthieu Cartigny

Chapter 1

Introduction

1.1 Rationale

Turbidity currents are subaqueous density flows that travel downslope due to the higher density of sediment they carry in suspension compared to the ambient water (Daly, 1936; Middleton and Hampton, 1973). Suspended sediment settle down as turbidity currents decelerate, resulting in sedimentary successions called turbidites (Bouma, 1962). These often-powerful flows can transport large quantities of sediment over several thousands kilometres to the deep sea (Piper et al., 1999; Talling et al., 2007). Turbidity currents are important for at least two reasons. First, turbidity currents rival sediment-fluxes of rivers on land, and are therefore one of the dominant processes for sediment transport on our planet (Talling et al., 2012). Turbidity current systems often connect to terrestrial river systems, hence they are important conduits for the offshore transfer of not only sediment but also organic carbon (Liu et al., 2013) and pollutants such as plastic debris (Jambeck et al., 2015; Kane and Clare, 2019). Second, fast-moving, powerful turbidity currents can damage crucial seafloor infrastructure, such as the global network of telecommunication cables and hydrocarbon pipelines (Carter et al., 2014), and carve extensive submarine channels (Fildani et al., 2006; Covault et al., 2014; de Leeuw et al., 2016). Such submarine channels supply sediment to deep sea fans; the largest sediment accumulations on Earth (Bouma et al., 2012).

The deposits left behind by turbidity currents are called turbidites (Bouma, 1962) and have been studied from both modern and ancient systems for a number of reasons. First, as a result of their often-large volumes and interconnected stratigraphy, ancient turbidites can form valuable oil and gas reservoirs (Weimer and Pettingill, 2007). Second, turbidite sequences are commonly used to reconstruct past changes in Earth history (e.g. climate evolution, past earthquakes, tsunamis, Reeder et al., 2002; Moernaut et al., 2014; Hunt et al., 2011). Third, there is an increasing realisation that turbidity currents are

responsible for transporting and subsequently burying large volumes of organic carbon, allowing atmospheric CO₂ drawdown over geological timescales (Galy et al., 2007).

Direct measurements of turbidity currents in natural settings has proved challenging (Inman et al., 1976; Sumner and Paull, 2014). As a result, our present understanding of turbidity currents is largely based upon models derived from their deposits (Talling et al., 2007; Hubbard et al., 2014), supplemented by scaled-down laboratory experiments (e.g. Spinewine et al., 2009; Cartigny et al., 2013), and uncalibrated numerical models (e.g. Cantero et al., 2012; Vellinga et al., 2017). Recent advances in technology have enabled the first detailed direct measurements of field-scale turbidity currents (e.g. Paull et al., 2002; Xu et al., 2004; Khripounoff et al., 2012; Xu et al., 2013; Hughes Clarke, 2016; Azpiroz-Zabala et al., 2017; Paull et al., 2018), however, there is a paucity of studies that link these flow observations with their deposits (e.g. Symons et al., 2017). As a result, inferences made about turbidity currents from their deposits are largely unvalidated. This missing link has implications as it can bias Earth history reconstructions and global carbon fluxes estimations. There is thus a need for direct field observations to bridge the gap between turbidity current processes and their depositional products, which constitutes the overarching objective of this thesis.

1.2 Aims and structure of the thesis

The overall aim of this thesis is to bridge the gap between turbidity current processes (i.e. initiation, flow properties and interaction with the seafloor) and their depositional products (e.g. sediment and buried organic carbon). To achieve this aim I use datasets collected in two fjords located in British Columbia (Canada), named Howe Sound and Bute Inlet (Figure 1.3). To date these datasets comprise the most extensive measurements of flows, seafloor mapping and sampling of the seafloor ever obtained in river-connected turbidity current systems anywhere in the world. Using these three types of data, I address the following research questions, which form part of three science chapters (chapters 2, 3 and 4).

a. How do extremely dilute river plumes generate turbidity currents? Existing models suggest that a threshold of sediment concentration exists, above which river will directly feed into turbidity currents (e.g. 40 g/L, 1g/L Mulder and Syvitski, 1995; Parsons et al., 2001, resp.). However, this threshold is based on calculations and laboratory experiments that need validation. Chapter 2 presents data collected by a series of acoustic instruments deployed from a combination of stationary and moving vessels on the river plume on the Squamish Prodelta (Howe Sound, Canada). These data are the first field measurements of this phenomenon, and show that existing studies overestimate this sediment concentration threshold and that turbidity currents may be more abundant than previously thought at river deltas around the world.

b. What are the diagnostic deposits of crescentic bedforms formed by supercritical turbidity currents? Supercritical (i.e. thin and fast) turbidity currents have been shown to produce crescentic bedforms that migrate upstream on the seabed (Hughes Clarke, 2016). Such bedforms are prevalent on the ocean floor (Symons et al., 2016) and are suggested to enhance sediment transport efficiency towards the deep sea (Sun and Parker, 2005). Given the significance of supercritical flows and associated bedforms for sediment transport, their deposits are important to identify. However, there is a general discrepancy between the deposits produced in experimental models (regular back-stepping beds of sediment, Kostic, 2011; Cartigny et al., 2011) and the observations described in outcrops interpreted as supercritical flow deposits (irregular lens-shaped beds of massive sands, Bain and Hubbard, 2016; Dietrich et al., 2016). Chapter 3 resolves this discrepancy by using a novel combination of flow monitoring, repeated seafloor mapping providing the architecture, and sediment cores providing the facies of supercritical flow deposits in a modern system (Squamish submarine delta).

c. How is young terrestrial organic carbon preserved in turbidites? Burial of young terrestrial organic carbon in marine sediments leads to a drawdown of atmospheric CO₂ and thereby regulates climate over geologic timescales (Bernier, 1982). The current paradigm is that most organic carbon is associated with fine sediments because the physical association of organic matter with clays allows persistence of terrestrial organic carbon in marine sediment (Mayer, 1994). In contrast with this paradigm, Chapter 4 demonstrates that young, coarse debris of wood accounts for the majority of terrestrial organic carbon sequestered in sandy fjord sediments emplaced by turbidity currents. This result is found in Bute Inlet (Canada) using a combination of 1) direct observations of turbidity currents, 2) sampling of their deposits (including samples into the river sources) and 3) detailed study of organic carbon reactivity and age based on a novel method called ramped oxidation – radiocarbon analysis (Hemingway et al., 2019).

All three science chapters have been submitted for publication; and are presented in their ‘journal format’ in this thesis. Chapter 2 has been published in *Geophysical Research Letters*. Chapter 3 has been published in *Geology*. Chapter 4 is in review in *Geology*. In addition a detailed description of scientific methods, data processing and instrument specifications is provided in the Appendix. Together, chapters 2, 3 and 4 enable better constraint of the link between turbidity current processes and their depositional products in fjords of British Columbia. More specifically, all three science chapters cover the full pathway of turbidity currents: from flow initiation by rivers (Chapter 2), flow interaction with the seafloor to the deposits left behind (Chapter 3), with a focus on the organic carbon composition of these deposits (Chapter 4). All three chapters include flow observations acquired by acoustic instruments as well as high resolution seafloor maps collected by multibeam systems. Chapters 3 and 4 both include sediment cores and log descriptions of turbidites. Finally, chapter 5 synthesises the findings demonstrated in the three science chapters and provides future research perspectives.

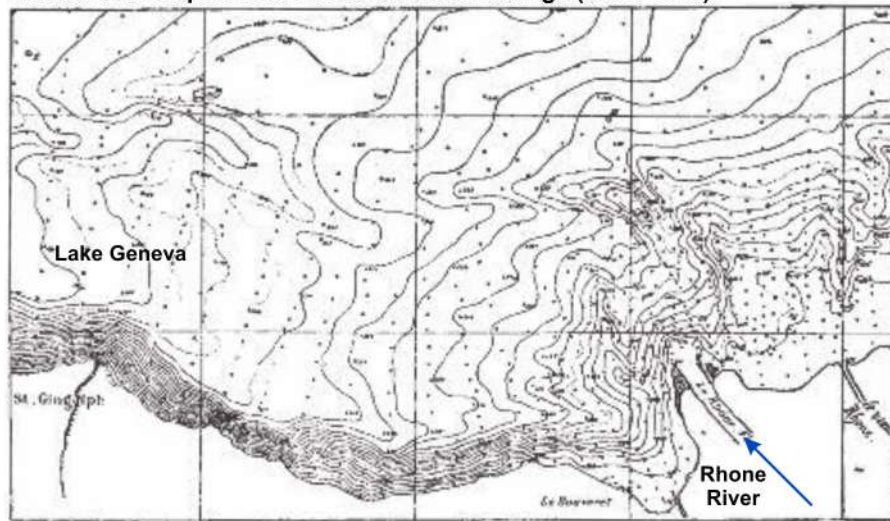
The present chapter provides a brief historical timeline of research on turbidity currents and their deposits that explains the general gap in understanding between turbidity current processes and products (section 1.3). Section 1.4 then presents the research carried out more specifically in British Columbia fjords in relation to the three science questions addressed in chapters 2, 3 and 4.

1.3 Why is there a gap in the link between turbidity current processes and their products: a brief historical timeline

The general knowledge gap between turbidity current processes and products reflects the lack of direct observations of turbidity currents during the past century. This section briefly reviews seminal studies carried out from the 19th century, to the present day to trace where the gap between turbidity current processes and products originates.

The first description of turbidity currents was reported by Francois-Alphonse Forel who used individual point soundings to describe the presence of a submarine channel in Lake Geneva, Switzerland (Forel, 1885). Forel attributed this submarine channel to the action of an underwater flow sourced from the Rhone River and which would erode the seafloor as it was flowing downslope (Figure 1.1a). Such flows were later on called *turbidity currents* by (Daly, 1936). These pioneering studies were the starting point in the realisation that dynamic sedimentary processes influence the subaqueous environment.

A. Seafloor map in 1885 from manual soundings (Forel 1895)



B. Seafloor map in 2012 from multibeam echosounding (Girardclos et al. 2012)

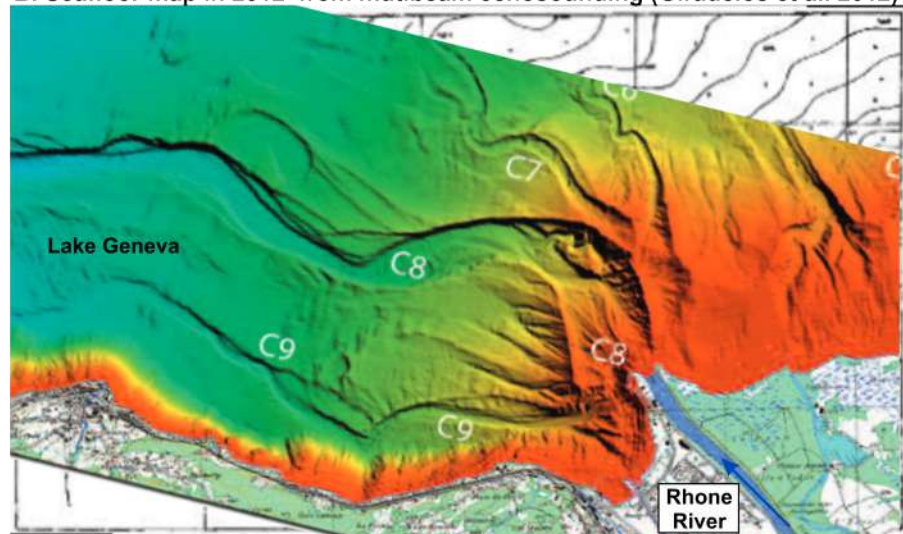


FIGURE 1.1: Comparison of the mapping performed downstream of the Rhone River in Lake Geneva (Switzerland) in 1885 (a) and in 2012 (b), modified from (Forel, 1885; Girardclos et al., 2012)

About 50 years after the work of Forel, (Kuenen, 1950) provided the first experiments on turbidity currents. Other experiments in flume tanks (e.g. Middleton, 1966; Lowe, 1982; Postma et al., 1988) served as the basis for interpreting turbidite deposits observed in sediment cores (e.g. Normark and Piper, 1972; Bowen et al., 1984) and the rock record (e.g. Shanmugam, 1980; Pickering and Hilton, 1998). The Bouma sequence (Figure 1.2, Bouma, 1962) was then formulated to describe the vertical sedimentary sequence typically resulting from a decelerating turbidity current. This model is still widely used to describe turbidites in the sedimentary record.

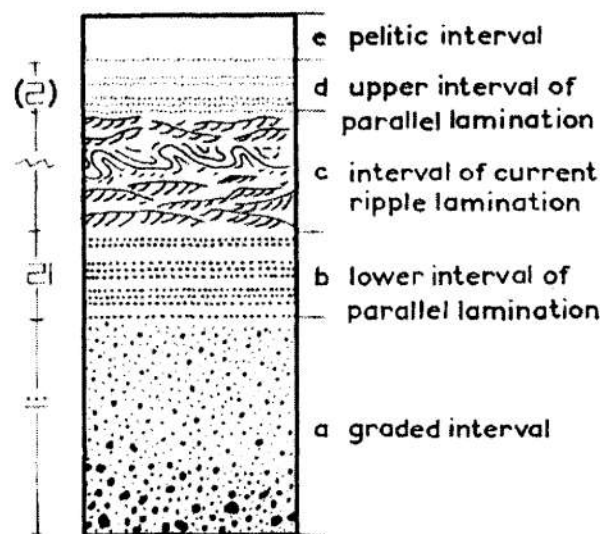


FIGURE 1.2: The Bouma Sequence shows the typical sedimentary deposit of a decelerating turbidity current divided into Ta, Tb, Tc, Td, Te units (Bouma, 1962).

The use of multibeam echosounders in the 1990's has allowed extensive and better mapping of the sea and lake floors worldwide. For example, the sublacustrine channel initially described by (Forel, 1885) was revealed in much greater detail one century later using a multibeam echosounder (Girardclos et al., 2012, Figure 1.1b). Bathymetric maps produced by multibeam systems elsewhere have revealed that submarine channels are abundant in lakes, fjords, and in the ocean (e.g. Normandeau et al., 2016; Conway et al., 2012; Wynn et al., 2014). The morphology of submarine channels has since then been used as another tool to infer about flow properties that potentially characterize the turbidity currents at their origin (Symons et al., 2016).

There has been a significant step forward in our understanding of turbidity current processes in the past few years thanks to the advent of technologies used to image flows in action (e.g. Xu et al., 2004; Khripounoff et al., 2012; Sumner and Paull, 2014; Hughes Clarke, 2016; Azpiroz-Zabala et al., 2017; Paull et al., 2018). Such direct observations have enabled better understanding of how turbidity currents interact with the seabed (Hughes Clarke, 2016) and also of their internal structure (Azpiroz-Zabala et al., 2017; Paull et al., 2018).

However, despite these remarkable advances in understanding flow processes, the link between active flows and resulting deposits is still poorly understood because it is challenging to predict when flows occur. This thesis thus builds upon flow observations previously acquired in British Columbia fjords (Bornhold et al., 1994; Hughes Clarke, 2016) and links them to the resulting depositional products, with a particular interest in the organic carbon preserved in these products.

1.4 Why study fjords to resolve the knowledge gap between turbidity current processes and products?

Fjords are deep, high latitude estuaries which have been (or are presently being) excavated by land-based ice (Syvitski et al., 1987). Fjords typically extend from a mountainous hinterland down to the sea, and are closed at their mouth by a sill. One or more glacier-influenced rivers are usually the major freshwater inflow into fjords (Syvitski and Murray, 1981). Therefore fjords constitute relatively small systems at the border between the land and the sea, that are sufficiently small scale to enable study of the whole turbidite system from their origin at the river mouth to their deposits in a seafloor fan. This thesis uses observations of turbidity current systems in fjords and thus aims to link flow processes with their products in submarine systems that are directly connected to land.

In the following sections I first report on the environmental setting and research background of the two fjords used in this thesis (section 1.4.1). I then explain why these fjords were chosen to resolve the three research questions addressed in this thesis (sections 1.4.2 to 1.4.4). I finally briefly discuss the concept of fjords as analogues to turbidity current processes and products occurring in larger oceanic settings that are directly connected to land (section 1.4.5).

1.4.1 Focus on two British Columbia fjords: Howe Sound and Bute Inlet

Canada has more fjords than all other countries combined and has the widest range of fjord types (Syvitski et al., 1987); e.g. temperate drainage basins free of snow, permanent ice-covered fjords, tide-/wave-/river- dominated fjords, permanently anoxic fjords, continuously oxygenated fjords, and low to high sedimentation rate fjords. In this thesis I focus on two temperate, river-dominated fjords characterised by high sedimentation rates (between 1 and 300 mm/year, Syvitski et al., 1987), which are part of the 75 mainland fjords of British Columbia (Howe Sound and Bute Inlet, Figure 1.3).

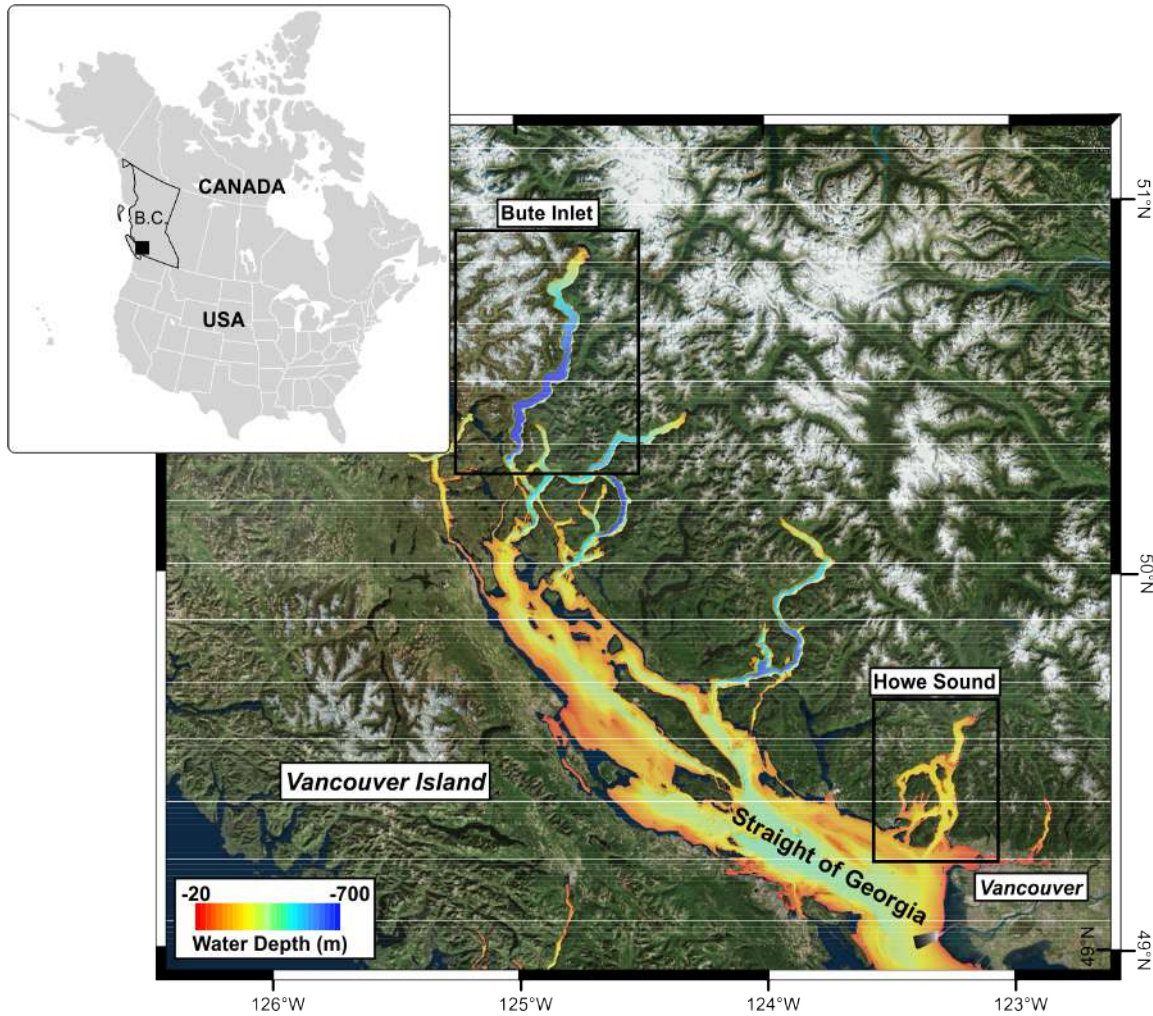


FIGURE 1.3: Location of the two fjords used in this thesis in British Columbia Canada.

The first fjord, named Howe Sound, is located on the southwest coast of British Columbia, close to the city of Vancouver (Figure 1.3 and 1.4a). Howe Sound is 42 km long and comprises several submarine valleys that form deep basins enclosed by two submerged sills (Hickin, 1989). Up to 600 m thick deposits of Quaternary sediments cover the basins (Syvitski and Macdonald, 1982). The maximum water depth (325 m) of Howe Sound occurs north of the first sill, half way down the fjord. Tides in Howe Sound are mixed semidiurnal, with a mean range of 3.2m and a macrotidal range of 5 m maximum (WaterSurveyCanada, 2018).

The second fjord, named Bute Inlet, is located 200 km to the North-West of Howe Sound (Figure 1.3). Bute Inlet is about 80 km long and 4 km wide (Figure 1.4b). Water depths range between 200 and 650 m, with maximum water depths terminating at a single sill (Prior et al., 1986). The mean tidal range of Bute Inlet is 3.6 m, with tidal height sometimes exceeding 5.5m (Water Survey of Canada, 2018).

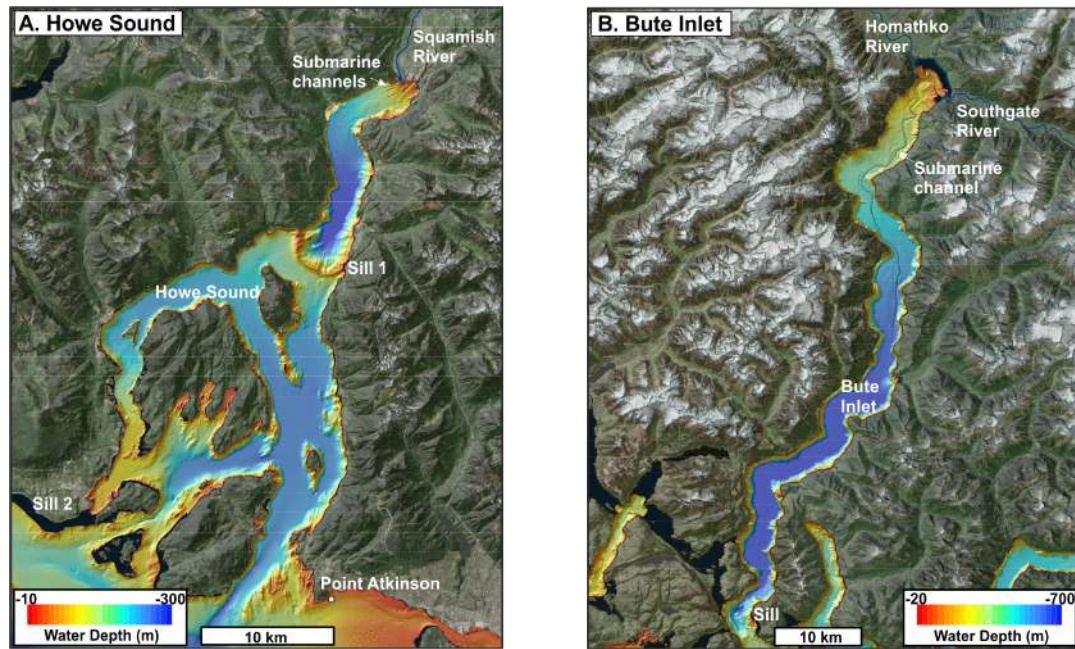


FIGURE 1.4: a. Bathymetry map of Howe Sound, fed by the Squamish River. b. Bathymetry map of Bute Inlet, fed by the Homathko and Southgate Rivers.

Scientists from the Canadian Hydrographic Service and Geological Survey performed the first detailed mapping of British Columbia fjords about 30 years ago using single beam echosounders, side-scan sonars and seismic profilers. Submarine channels were revealed, incised into the fjord seafloors (e.g. Howe Sound, Bute Inlet, Prior and Bornhold, 1984; Prior et al., 1986, resp.). Such submarine channels were associated with turbidity current activity directly observed in Bute Inlet by a suite of instruments composed of current meters, tilt meters, flow deflection vanes, sediment traps and turbidity event detectors (Prior et al., 1987; Bornhold et al., 1994). Flows were characterised by peak velocities in excess of 3 m/s, and run-out distances sometimes longer than 25 km and flow thicknesses of up to 30 metres. Some of the flows observed were powerful, and caused damage to moorings (Prior et al., 1987). However, these early studies did not consider the initiation of turbidity currents, their interaction with the submarine channels, and the character of their resulting deposits. While direct monitoring of flows has not been attempted in Bute Inlet since these early studies, flows were recently observed using groundbreaking technologies in Howe Sound (Hughes Clarke et al., 2014; Hughes Clarke, 2016). This thesis thus builds upon the early work in Bute Inlet and the recent flow observations in Howe Sound by addressing the three research questions presented in section 1.2 and further developed in the following sub-sections.

1.4.2 Fjords are natural laboratories to study the connection of rivers with offshore sediment transport

Howe Sound and Bute Inlet are ideal locations to study the link between rivers and offshore sediment transport because they are directly connected to glacier-fed rivers. The Squamish River flows into Howe Sound at the head of the fjord. It has an annual river discharge of $250 \text{ m}^3/\text{sec}$, with maximum discharges of up to $1000 \text{ m}^3/\text{sec}$ in the freshet due to the snow melt from the surrounding glaciers (Water survey of Canada, 2018). Bute Inlet is fed by the Homathko and Southgate Rivers which contribute 75 % and 19 % of the annual water inflow respectively (Zeng et al., 1991). Homathko River can reach $1600 \text{ m}^3/\text{s}$ in summer and has an average of $200 \text{ m}^3/\text{sec}$ annually (Water Survey of Canada, 2018).

The instruments deployed in the 1980's demonstrated that flows are frequent during the freshet period (25-30 events per year), yet how turbidity currents are initiated by rivers remained unresolved (Bornhold et al., 1994). Recent studies in Howe Sound have shown that turbidity currents predominantly occur at low tide when the river discharge exceeds $250 \text{ m}^3/\text{sec}$ (Clare et al., 2016). 27 % of flows were further shown to be initiated from delta slope failures while the remaining 73 % of flows were associated with settling of dilute plumes (Hizzett et al., 2018). However, the mechanism by which dilute plumes can trigger turbidity currents is unknown. Chapter 2 of this thesis resolves the mechanism by which dilute plumes trigger turbidity currents, and provide the first direct observations of a very dilute river plume generating turbidity current.

1.4.3 River-fed fjords contain highly dynamic submarine channels re-worked by frequent turbidity currents

The use of swath multibeam bathymetric surveys over the last 10 years has enabled detailed characterisation of the channels formed by turbidity currents in British Columbia fjords (Fig. 1.4, Conway et al., 2012; Brucker et al., 2007; Hughes Clarke et al., 2012; Gales et al., 2019). Submarine channels were revealed to be covered by highly dynamic features such as upslope-migrating knickpoints (e.g. in Bute Inlet Conway et al., 2012, Fig. 1.5) and trains of upslope-migrating crescentic bedforms (e.g. in Howe Sound, Hughes Clarke et al., 2014, Fig. 1.5). The very recent development of flow monitoring technologies has enabled direct links between such upslope-migrating bedforms and confined supercritical (i.e. thin and fast) turbidity currents in a submarine channel downstream of the Squamish Delta in Howe Sound (Hughes Clarke, 2016).

Besides submarine channel mapping and turbidity current monitoring, seafloor deposits have been sampled in British Columbia fjords (e.g. Zeng et al., 1991; Stacey et al., 2019). Coarse grained sediment (massive sands Bouma Ta) were revealed to cover the submarine channel thalwegs of Bute Inlet and Howe Sound. Cored sedimentary deposits

were further shown to fine downslope from the confined submarine channels to the distal lobes. These sets of sediment cores have enabled flow properties and recurrence intervals of turbidity currents in Bute Inlet and Howe Sound to be inferred (Zeng et al., 1991; Stacey et al., 2019).

Despite the major progress in understanding seafloor morphology and sedimentary products in British Columbian fjords, the link between flows, bedforms and deposits is still largely unresolved. Chapter 3 of this thesis focuses on the deposit facies/architecture produced by supercritical turbidity currents observed to form upstream-migrating bedforms in the proximal channels of Howe Sound.

1.4.4 Fjords are globally significant for organic carbon burial

While British Columbia fjords have been recognized as potentially important sinks for organic carbon (Syvitski et al., 1987), the role of turbidity currents in distributing and preserving organic carbon particles has not been addressed in these fjords. Fjords are considered to be efficient sinks for organic carbon for two main reasons. First, fjords are directly connected to terrestrial rivers and mountains which can deliver large amounts of organic carbon over short time periods (Hilton et al., 2012). Second, subaqueous fjord deposits have a great burial potential due to high sedimentation rates (between 0.1 and 9000 mm/year, Syvitski et al., 1987). For these reasons, fjords were shown to account for 11 % of the annual organic carbon burial globally, based on 573 surface sediment samples and 124 sediment cores taken from all types of fjords worldwide (Smith et al., 2015). Following this global study, it has been proposed that 55 to 62 % of the organic carbon buried in fjords is terrestrial (as opposed to marine; Cui, Bianchi, Savage and Smith, 2016), biospheric (as opposed to rock-derived; Cui, Bianchi, Jaeger and Smith, 2016), and modern (Cui et al., 2017). Such findings are important as the burial of young biospheric terrestrial organic matter in marine sediment directly inhibits the escape of organic carbon as atmospheric CO₂, which influences the global climate over geological timescales (Bernier, 1982; Hayes and Waldbauer, 2006; Blair and Aller, 2012).

However, those studies have largely ignored the dynamic sedimentary processes that occur in fjords, in particular within turbidity current channels. In chapter 4 of this thesis I aim to test the role of turbidity current channels in organic carbon transport and burial by using direct observations of turbidity current processes and products in Bute Inlet.

1.4.5 Fjords provide insights into larger deep ocean systems

Fjords are often seen as mini-oceans where particle inputs and outputs can be more easily constrained compared to ocean systems (Syvitski et al., 1987). Fjords are indeed

relatively accessible due to their close location to the shore and their sheltered nature. Furthermore, the occurrence of turbidity currents can be relatively well predicted because many sub-annual flows are associated with the relatively higher sediment delivery during the freshet period (Prior et al., 1986; Bornhold et al., 1994; Clare et al., 2016). I suggest that the science demonstrated in chapters 2, 3, and 4 can serve as analogues larger oceanic basins for the following reasons.

First, although the scale (i.e. general extent and depth) of fjords is an order of magnitude smaller than oceanic settings, fjords share similarities with larger settings in terms of seafloor morphology (Figure 1.5). For instance, detailed mapping of submarine channels in Bute Inlet and Howe Sound reveals the presence of scours (named knick-points) and trains of crescentic bedforms which migrate upstream (e.g. Conway et al., 2012; Hughes Clarke et al., 2014). These features are commonly found in ocean canyons (Symons et al., 2016) with similar scale and shapes to the ones observed in fjords, e.g. Monterey and Var canyons (Paull et al., 2011; Migeon et al., 2012). The formative processes of such features were first studied using experimental models (e.g. Spinewine et al., 2009; Yokokawa et al., 2009; Toniolo and Cantelli, 2007, Fig. 1.5). Relatively easy access to fjords systems now allows these experimental findings to be tested and further expanded in natural environments (e.g. Hughes Clarke, 2016).

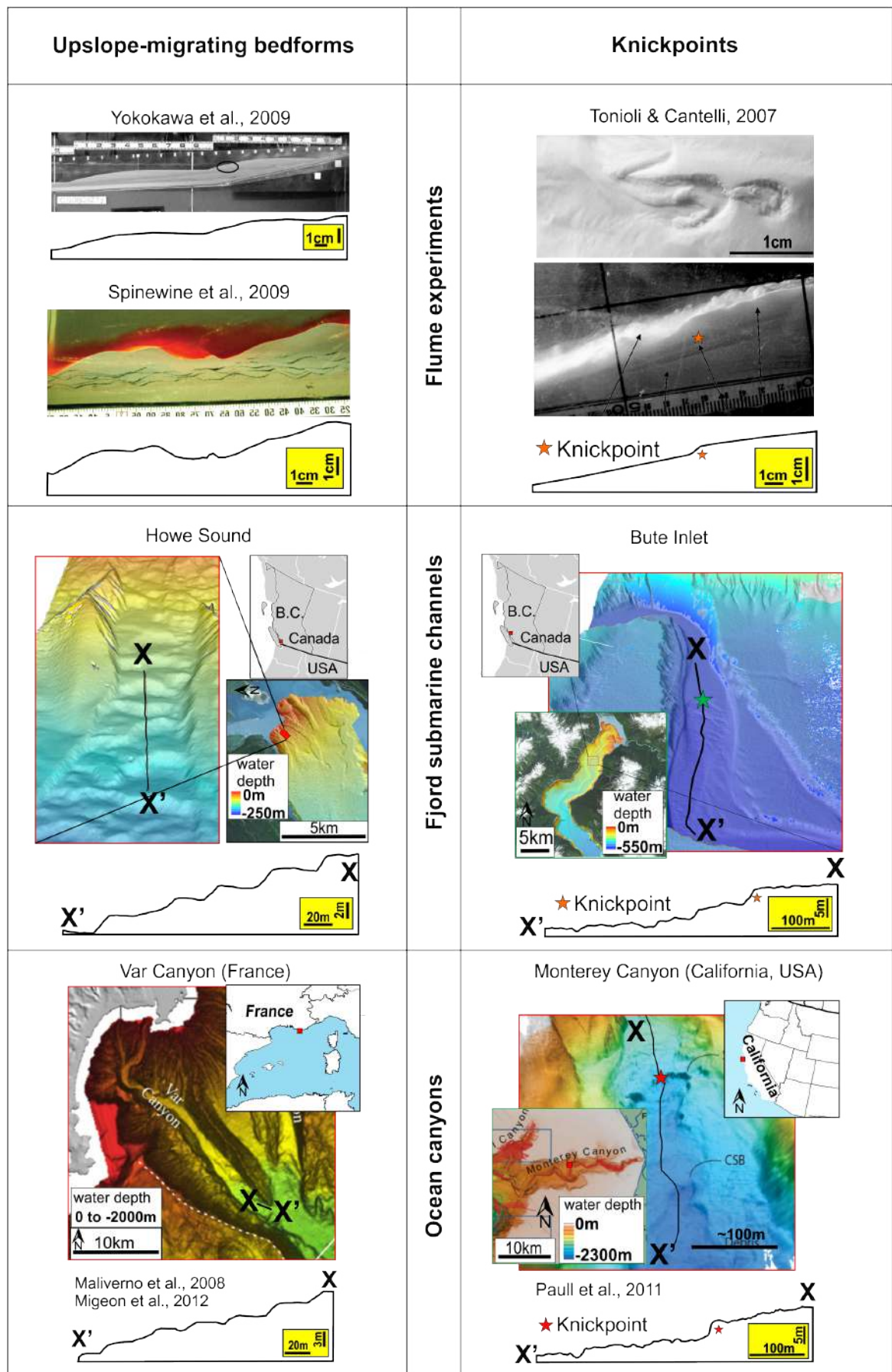


FIGURE 1.5: Seafloor geomorphological features modelled in flumes and observed in fjords and ocean settings.

Second, fjords are comprehensive systems where sedimentary inputs can be tracked from source (i.e. rivers) to sink (due to the confinement of the distal sill) due to their direct connection with the rivers and their relatively small scale compared to oceanic systems. The distribution of river-derived, i.e. terrestrial, materials by turbidity currents can thus be characterised in unprecedented detail in fjords. Given that fjords contribute 11 % of the annual organic carbon burial globally (Smith et al., 2015) and that carbon burial in marine sediments controls atmospheric CO₂ levels (Blair and Aller, 2012), it is particularly key to be able connect the terrestrial to the marine environment in fjords.

It has to be noted that source to sink studies made in fjords may not upscale to all ocean systems. I thus suggest that source to sink observations made in this thesis will apply in the proximal parts of coarse-grained ocean submarine channels directly fed by rivers influenced by tides and surrounded by woody vegetation. The upscale of the scientific findings demonstrated in chapters 2, 3, and 4 to ocean settings will be further discussed in all three chapters and in the final chapter 5.

Chapter 2

Direct monitoring reveals initiation of turbidity currents from extremely dilute river plumes

This chapter forms a peer-reviewed paper published in *Geophysical Research Letters*: **Hage, S.**, Cartigny, M.J.B., Clare, M.A., Sumner E.J., Hughes Clarke, J.E., Vardy, M.E., Talling, P.J., Lintern D.G., Simmons, S.M., Vellinga, A. J., Silva Jacinto, R., Vellinga, A. J., Allin, J.R, Azpiroz-Zabala, M., Gales, J.A., Hizzett, J. L, Hunt, J. E., Mozzatto, A., Parsons, D. R., Pope, E.L., Stacey, C.D., Symons, W.O., Vardy, M.E., Watts, M. (2019). Direct monitoring reveals triggering of turbidity currents by extremely dilute river plumes. *Geophysical Research Letters* <https://doi.org/10.1029/2019GL084526>

Author contributions: J.R.A., M.A., M.J.B.C., M.A.C., S.H., J.E.H.C., J.E.H., J.A.G., J.L.H., D.G.L., A.M., D.R.P., E.L.P., C.D.S., E.J.S., W.O.S., M.E.V., C.W. collected the data as part of the June 2015 Squamish field experiment. S.H. processed the ADCP, OBS, CTD data. J.E.H.C. processed the water column transect images by the M3. S.H., A.J.V., S.M.S. inverted the ADCP backscatter into sediment concentration. S.H., M.J.B.C., E.J.S., M.A.C., J.E.H.C., D.G.L., R.S.J. analysed the data. S.H., M.J.B.C., E.J.S., M.A.C. wrote the manuscript. All authors read and agreed on the final version of this manuscript.

2.1 Abstract

Rivers (on land) and turbidity currents (in the ocean) are the most important sediment transport processes on Earth. Yet, how rivers generate turbidity currents remains poorly understood. The current paradigm, based on laboratory experiments, is that turbidity currents are triggered when river plumes exceed a threshold sediment concentration of 1 kg.m^{-3} . Here we present direct observations of an exceptionally dilute river-plume, with sediment concentrations one order of magnitude below this threshold (0.07 kg.m^{-3}), that generated a fast (1.5 m/s), erosive, short-lived (6 min) turbidity current. However, no turbidity current occurred during subsequent similar river-plumes. We infer that turbidity currents are generated when fine-sediment, accumulated in a tidal turbidity maximum is released during spring tide. This means that very dilute river-plumes can generate turbidity currents more frequently and in a wider range of locations than previously thought.

2.2 Introduction

Turbidity currents are seafloor hugging flows that are driven by their suspended sediment (Daly, 1936; Middleton and Hampton, 1973). These flows are the main process transporting terrestrial sediment from river mouths into the deep-sea. The combination of rivers and turbidity currents accounts for the majority of global sediment transport (Talling, 2014). However, the link between rivers and turbidity currents is poorly understood because there are few direct measurements of how turbidity currents are generated at river mouths (Ayranci et al., 2012; Hizzett et al., 2018). Understanding this link is important for understanding the global redistribution of sediment, organic matter (Liu et al., 2012) and pollutants such as plastic (Kane and Clare, 2019).

Three main processes have been proposed for the initiation of turbidity currents from river plumes (Piper and Normark, 2009; Clare et al., 2016). First, delta slope failures generate submarine landslides that evolve into turbidity currents (Figure 2.1a; Piper and Savoye, 1993; Clare et al., 2016; Obelcz et al., 2017). Second, river plumes that are denser than seawater ($>40 \text{ kg.m}^{-3}$ of sediment) directly feed turbidity currents (Figure 2.1b; Mulder and Syvitski, 1995; Liu et al., 2012); this is commonly called a plunging hyperpycnal flow. Only 9 out of 150 rivers studied by Mulder and Syvitski (1995) have sufficient sediment concentrations to enable the formation of plunging hyperpycnal flow. Third, experiments suggest that turbidity currents can be generated by dilute river plumes with sediment concentrations as low as 1 kg.m^{-3} (Figure 2.1c; Parsons et al., 2001) if the plume locally becomes denser than ambient seawater (by either double diffusion or settling-driven convection; Hoyal et al., 1999a,b; Jazi and Wells, 2016; Parsons et al., 2001; Sutherland et al., 2018). This 1 kg.m^{-3} threshold implies that 61 of the 150 rivers studied by Mulder and Syvitski (1995) can generate turbidity currents.

In this paper we define that a river plume has initiated a turbidity current at the point that the flow is able to erode the seabed. A small number of field studies have suggested that rivers with suspended sediment concentrations less than the 1 kg.m^{-3} threshold can generate turbidity currents. For example, turbidity currents were reported offshore from the Sepik River (sediment concentrations 0.04 to 0.25 kg.m^{-3} Kineke et al., 1995), and the Fraser River (sediment concentration of 0.18 kg.m^{-3} Ayranci et al., 2012; Lintern et al., 2016). This implies that there could be a fourth mechanism for generating turbidity currents at river mouths. Importantly, such very dilute sediment concentrations characterise 144 of the 150 rivers studied by Mulder and Syvitski (1995), implying that almost all rivers might be able to directly initiate offshore turbidity currents.

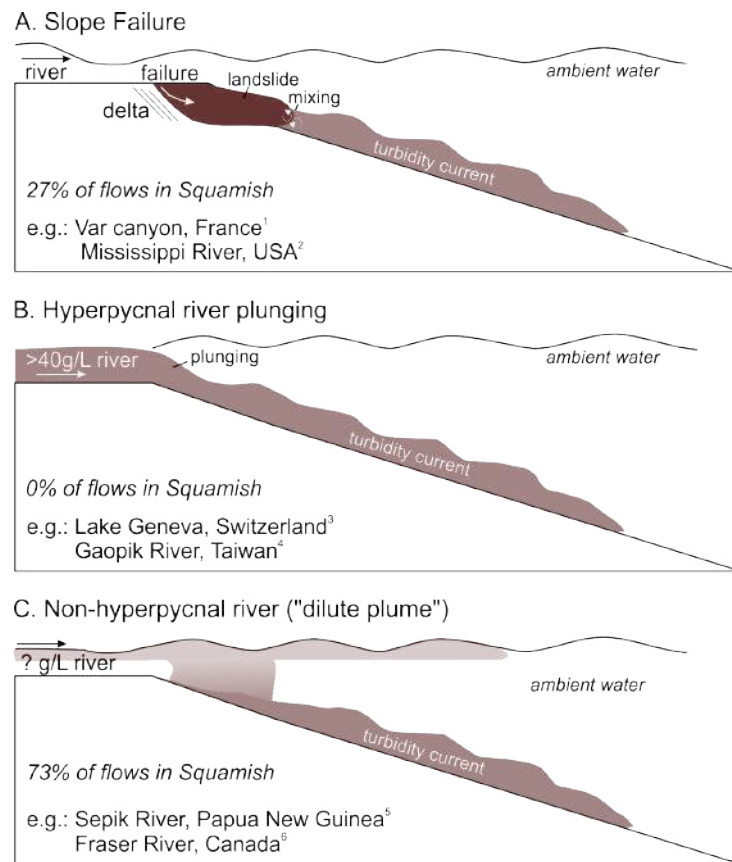


FIGURE 2.1: Mechanisms triggering turbidity currents at river mouths proposed in the literature. Statistics in Squamish are based on Hizzett et al., 2017. References for given examples: 1: Piper and Savoye, 1993, Mulder et al., 1997. 2: Obelcz et al., 2017. 3: Girardclos et al., 2012. 4: Carter et al., 2012, Liu et al., 2012. 5: Kineke et al., 2000. 6: Lintern et al., 2016

The physical process(es) that generate turbidity currents from very dilute river-plumes are not yet understood, primarily due to the absence of direct real-world observations. Here we present the first detailed observations of how a turbidity current is generated by a dilute river-plume. This was achieved by deploying an innovative array of sensors from both stationary and moving vessels at a fjord-head delta.

2.2.1 Aims

Our first aim is to understand how very dilute rivers generate turbidity currents. We document the temporal evolution of a dilute river plume throughout multiple tidal cycles. We propose a new mechanism that explains the formation of a single 6-minute-long self-accelerating turbidity current from this dilute river plume. Our second aim is to understand the wider implications of this new mechanism for triggering of turbidity currents globally.

2.3 Setting of field measurements

The Squamish Delta lies at the mouth of the Squamish River in Howe Sound, a fjord in British Columbia, Canada (Figure 2.2a). This fjord has a shallow surface layer ($\sim 2\text{m}$) composed of turbid fresh water due to discharge of the Squamish River, which is underlain by saline marine water (Syvitski and Murray, 1981). Tides in Howe Sound are mixed semidiurnal, with a macrotidal range of $\sim 5\text{m}$ (Buckley, 1977).

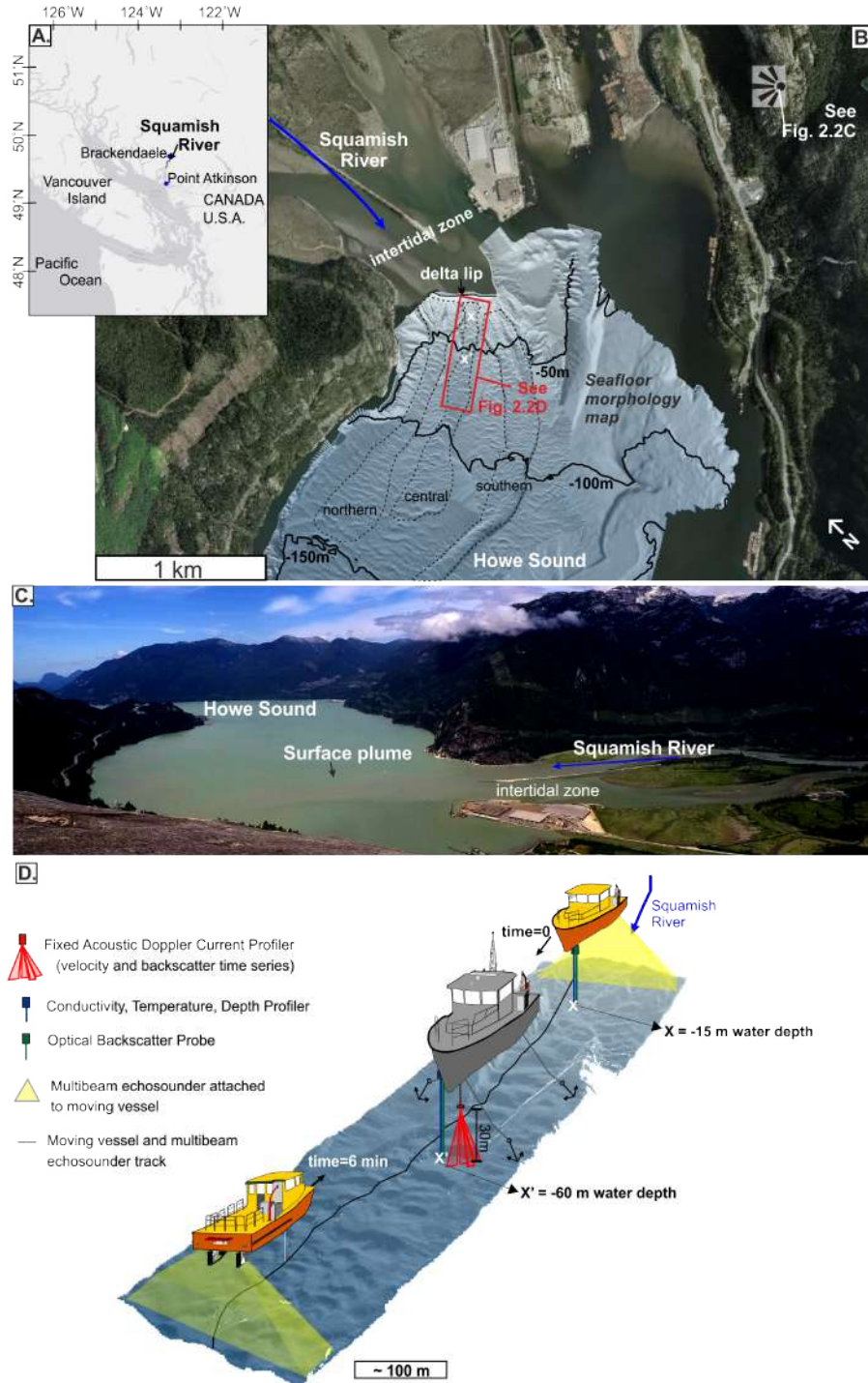


FIGURE 2.2: Setting and field deployment. a. Location of Squamish in British Columbia (Canada). b. Squamish river entering Howe Sound Fjord and bathymetric map of the seafloor. c. Photograph showing the Squamish River entering Howe Sound fjord as a surface plume. d. 3 dimensional view of the instrument set-up in the central submarine channel.

Three sandy submarine channels lie downstream of the delta lip. These channels have been mapped repeatedly since 2011 (Figure 2.2b, Hughes Clarke, 2016; Hage et al., 2018), and several self-accelerating turbidity currents have been observed (with typical

velocities: $0.5 - 3 \text{ m.s}^{-1}$; Hughes Clarke, 2016). These turbidity currents are erosional because they are documented as causing movement of upstream-migrating bedforms within the channels (Hughes Clarke, 2016; ?; Hage et al., 2018). Turbidity currents predominantly occur at low tide, and when the river discharge exceeds $250 \text{ m}^3.\text{s}^{-1}$ (Clare et al., 2016). In 2011, 106 turbidity currents were monitored; 27% of flows were triggered by slope failures on the delta lip; and 73% of flows were associated with settling of dilute plumes (Hizzett et al., 2018). The Squamish River does not reach the sediment concentrations (40 kg.m^{-3}) needed for wholesale plunging (Mulder and Syvitski, 1995), or the 1 kg.m^{-3} threshold to undergo double-diffusion related settling (Parsons et al., 2001). The Squamish delta is thus a well-suited natural laboratory to measure how very dilute river-plumes generate turbidity currents.

We collected observations from 13th - 17th June 2015 in the central submarine channel (Figures 2.2b, d). River discharge was relatively low ($300 - 400 \text{ m}^3.\text{s}^{-1}$) for summer time, yet higher than the minimum river discharge associated with occurrence of turbidity currents ($250 \text{ m}^3.\text{s}^{-1}$, Clare et al., 2016). Our observations took place during several tidal cycles, when the tidal amplitude (3.5 to 4m) was gradually building toward spring tide (Figure 2.3a).

2.4 Methods

We deployed instruments from two research vessels to study the river plume and its associated turbidity currents for five days (Figure 2.2d). The first vessel (RV Strickland) was moored by four anchors, and was located above the southern channel, 300 m downstream of the delta -lip, at a water depth of 60 m. This stationary vessel was used to: suspend a down-looking 600 KHz Acoustic Doppler Current Profiler (ADCP) 30 m above seafloor to detect turbidity currents and measure their velocity; and collect suspended sediment samples from the water column to calibrate our acoustic measurements. The second moving vessel (RV Heron) repeatedly surveyed the central channel every 12 minutes, for a three-hour period around low tide. The RV Heron carried two multibeam echosounders, an Optical Backscatter probe (OBS) and Conductivity Temperature Depth probe (CTD) that were raised and lowered to profile the water column.

2.4.1 Turbidity current velocity and river-plume concentrations

The ADCP deployed from the stationary vessel was used to: 1) detect turbidity currents and measured flow velocity; and 2) measure acoustic backscatter of the plume and turbidity current, which we inverted to suspended sediment concentration using established methods (e.g. Downing et al., 1995; Thorne and Hurther, 2014; Azpiroz-Zabala et al., 2017). Backscatter was corrected for water attenuation and for spherical spreading of

the acoustic waves (Downing et al., 1995). Corrected backscatter was then correlated with sediment concentration of the flow, assuming a uniform grain-size distribution (40 μm D_{50} in the dilute plume; 200 μm D_{50} in the turbidity current based on the sediment samples collected in the water column). There is good agreement ($\pm 0.005 \text{ kg.m}^{-3}$) between the concentration calculated from the inversion and the physical measurements from sediment sampling (suppl. Fig. 2.7).

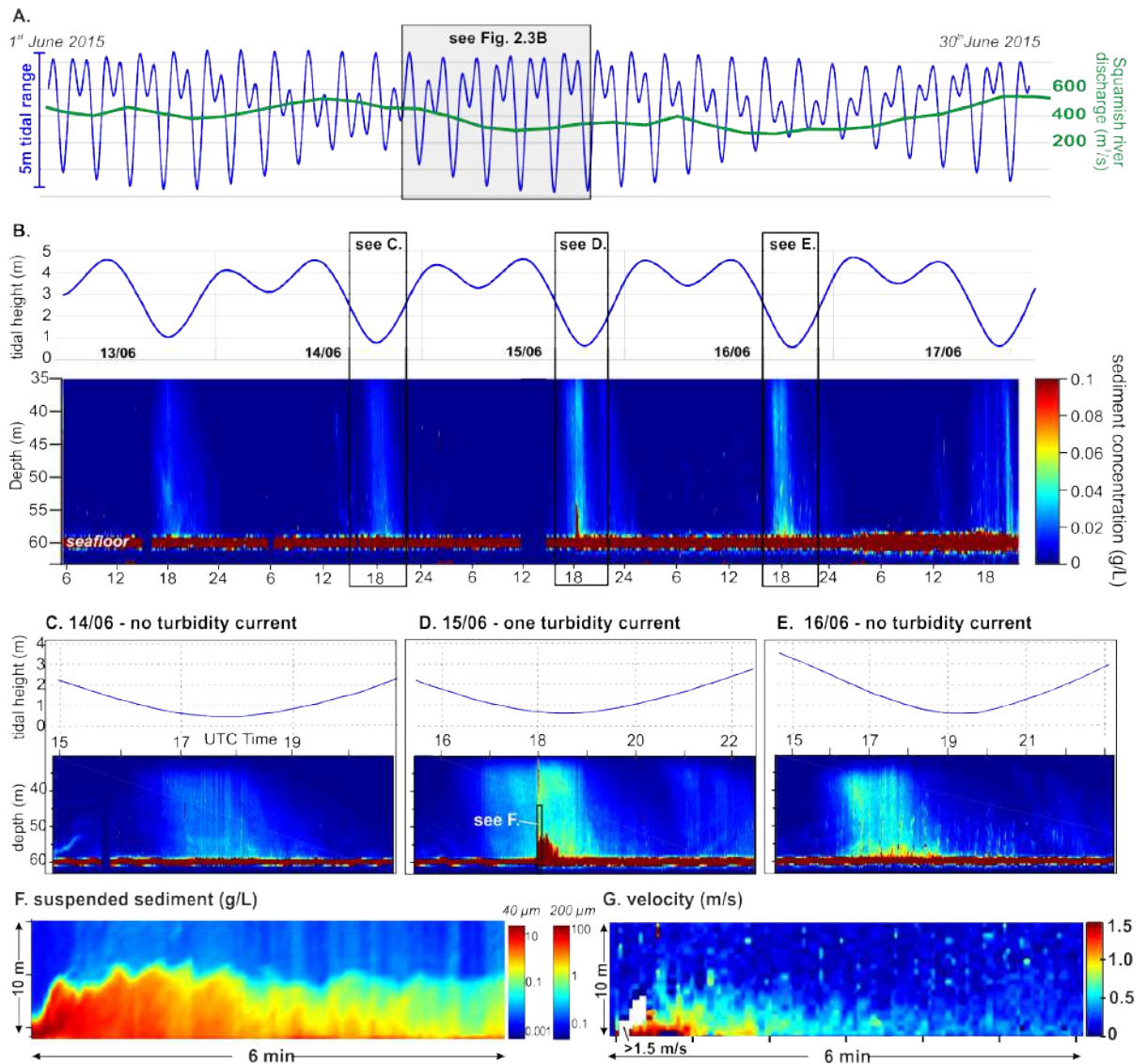


FIGURE 2.3: Acoustic Doppler Current Profiler (ADCP) results. a. Tides observed at Atkinson Station and Squamish River discharge measured at Brackendaele in June 2015. b. Tides and suspended sediment time series at fixed vessel location (see Fig. 2.2) from 13th to 17th June 2015. Suspended sediment was obtained after inversion of a 600 KHz ADCP backscatter (assuming grain size distribution with $D_{50} = 40 \mu\text{m}$). c. Tide and suspended sediment time series on 14th June. d. Tide and suspended sediment times series on 16th June. e. Tide, suspended sediment time series on 15th June. f. Suspended sediment in the turbidity current (assuming grain size distribution with 1) $D_{50} = 40 \mu\text{m}$, 2) $D_{50} = 200 \mu\text{m}$). g. velocity magnitude of the turbidity current. Note: These time series images cover 35m to 60m of water depth and thus only show the lower layer imaged in Fig. 2.5a.

2.4.2 Salinity, temperature and suspended sediment concentrations

CTD and OBS probes were deployed from the moving vessel at two locations in the central channel. The *proximal location* was 100 m off the delta lip, at 15 m water depth. A *distal (background) location* was situated 500 m off the delta lip, in 60 m water depth (Figure 2.2d). CTD profiles enabled derivation of ambient water density (Figure 2.5a). OBS probe voltages were converted to sediment concentration by calibration with suspended sediment samples (see suppl. Fig. 2.8 for calibration curve). Salinity, temperature and suspended sediment concentrations were combined to derive the density profiles at the proximal and distal locations in the river plume.

Based on these total water densities, we computed horizontal density gradients through the uppermost 10 m of the water column. This was achieved by comparing density values at the same water depth within the river plume (proximal location) and the ambient saline background (distal location, Figure 2.4). A density gradient <1 corresponds to the river plume (at the proximal location) being lighter than the saline background water, implying that the sediment laden water is confined against the delta by the salt water. A density gradient >1 corresponds to the river plume being denser than the saline background water, such that the sediment-laden water can migrate offshore.

2.4.3 Repeated water column imaging and seafloor mapping

We used a 70-100 kHz multibeam echosounder attached to the moving vessel to map the seafloor and detect any erosion/deposition caused by turbidity currents. A second 500 KHz multibeam echosounder also attached to the moving vessel imaged the suspended sediment (expressed as higher, white backscatter on Figure 2.5) throughout the depth of the water column from the delta-lip to 800 m offshore.

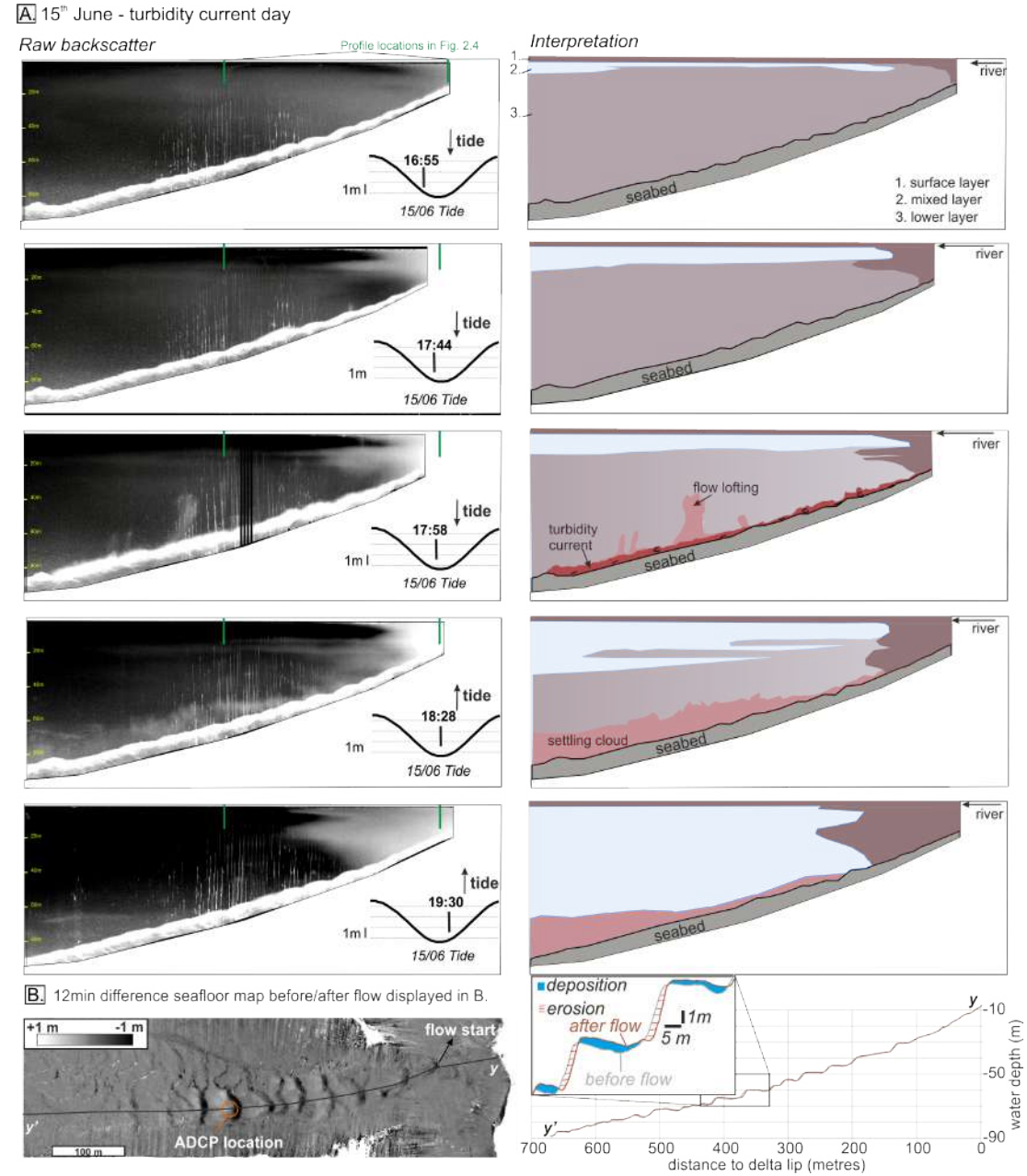


FIGURE 2.5: a. Left panel: 5 water column transects imaged by a 500 KHz M3 echosounder on 15th June 2015 along profile track shown in Fig. 2.2c. Right panel: Interpretation and transects timing according to tides. b. Difference map between seafloor morphology 12 min before/after the turbidity current. The turbidity current caused up to 2 m of erosion and up to 1 m of deposition

2.5 Results

2.5.1 Water column structure and horizontal density gradients

We divide the water column into three layers (Figures 2.5a and 2.6a): 1) the *surface layer* is 2 m thick, water is fresh (0-5 PSU), temperature is variable (10-15 °C) and

suspended sediment concentrations are high (0.04 to 0.05 kg.m^{-3}); 2) the *mixed layer* is from 2 to 5 m in the water column, salinity and temperature increase to 30 PSU and 14°C respectively, and suspended sediment decreases to 0.02 kg.m^{-3} ; 3) the *lower layer* extends to the seabed, water is saline (29-30 PSU), temperature is 11 to 12°C , and suspended sediment concentrations are low (0.01 to 0.02 kg.m^{-3}).

Here we describe the horizontal density gradients in each of the three layers (Figures 2.2d, 2.4 and 2.6a). The *surface layer* had a density gradient <1 during our study period, as the distal brackish water distally was always denser than the proximal fresh water in the river plume. The *mixed layer* had density gradients fluctuating from <1 to >1 on 15th and 16th June, due to a strong mixing between salt water and the river plume. The *lower layer* had neutral density gradients on 14th June, with density gradients in excess of 1 for about 2 h at low tide on the 15th and 16th June. Density gradients >1 are due to enhanced sediment concentrations in the saline lower water close to the delta.

Importantly, although the >1 density gradient in the lower layer occurs for several hours at low tide on 15th and 16th June, only one 6-minute-long turbidity current was triggered on 15th June at 17:58 UTM, when the density gradient first exceeded 1 (Figure 2.4).

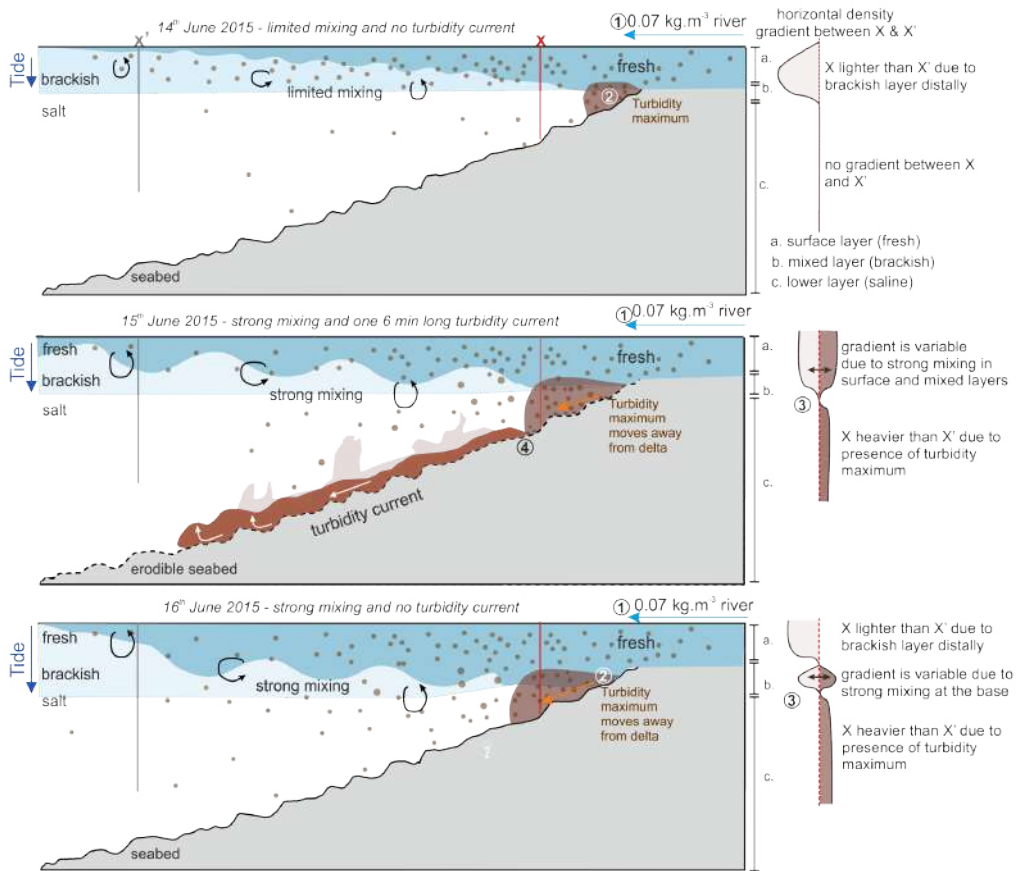
2.5.2 Observations of the 15th June turbidity current

The turbidity current (peak internal velocity = 1.5 m/s) lasted 6 minutes, was up to 6 m thick, and was confined within the 10 m deep channel (Figure 2.3f). Seafloor surveys 12 min before, and 12 min after the turbidity current (Figure 2.5b) reveal that the turbidity current started eroding 100 m downstream of the river mouth (at our proximal water-sampling location). These time-lapse surveys show the turbidity current was most erosive at a site 500 m downstream of the river mouth (at our ADCP location). Sediment-laden water samples taken from the top of the turbidity current two minutes after the flow began reveal that the turbidity current was at least 40 kg.m^{-3} ; which is corroborated by the ADCP backscatter data (Figure 2.3f). The total volume of sediment carried by the turbidity current is estimated to be less than 670 m^{-3} from sequential seafloor surveys, and more than 180 m^{-3} from the acoustic inversion (which excludes the bottom meter of the flow; Table 2.2).

2.5.3 Summary

Our results show that sediment settling from a very dilute (0.07 kg.m^{-3}) river plume generated a turbidity current that self-accelerated over a distance of 500 metres and became >200 times denser than the initial surface plume. Importantly, this turbidity current initiated from a plume that was an order of magnitude less concentrated than previously thought possible (Parsons et al., 2001); however similar subsequent plumes did not trigger any more turbidity currents.

A. Summary sketches of the observations described in this study at low tide



B. River discharge versus suspended load in 150 rivers worldwide (modified from Mulder & Syvitski, 1995)

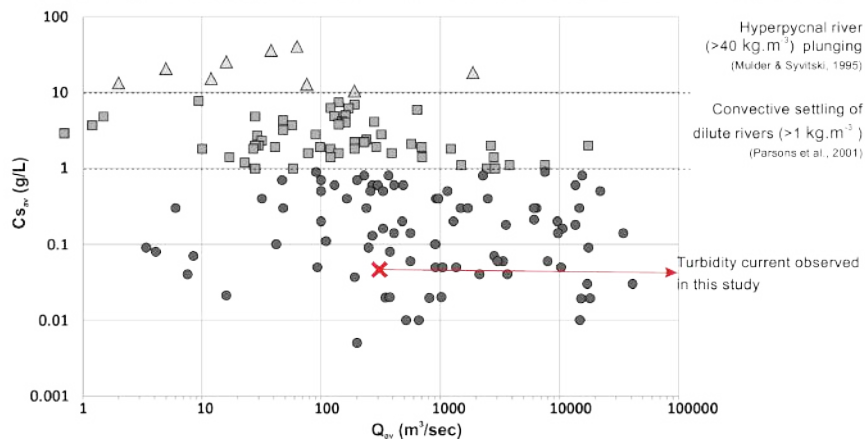


FIGURE 2.6: a. Summary sketches of the observations described in this study. Density ratio sketches correspond to the density difference at the proximal location X compared to the distal location X'. One turbidity current occurred on 15th June in the following steps: 1. dilute river creates a plume at the fjord surface; 2. higher sediment concentration occurs at X in the lower layer due to downslope movement of the turbidity maximum; 3. higher sediment concentration at X generates a positive density gradient, triggering the lower layer to move away from the delta; 4. if the sediment cloud in the lower layer moves away from the delta on an erodible substrate, it can erode and accelerate into a turbidity current. b. River discharge versus suspended load in 150 rivers worldwide (based on Mulder and Syvitski, 1995), with corresponding mechanisms described in previous studies and in this study.

2.6 Discussion

We compare our observations with previously suggested trigger mechanisms and thresholds and consider when and how dilute river plumes generate turbidity currents. We then discuss the wider implications of our work for the global frequency of turbidity currents offshore from rivers.

2.6.1 A reduced threshold sediment concentration for generating turbidity currents

Experiments have shown that dilute ($0.5\text{--}7\text{ kg.m}^{-3}$) river plumes entering saline water can settle towards the seabed by either double diffusion or settling-driven convection (Hoyal et al., 1999*a,b*; Parsons et al., 2001; Jazi and Wells, 2016; Sutherland et al., 2018). In these experiments turbidity currents were only generated when the settling plume had a concentration $>1\text{ kg.m}^{-3}$ (Parsons et al., 2001). At Squamish Delta, we show that the sediment concentration threshold needed for sediment to reach the lower layer in the water column, and to trigger a turbidity current, can be much lower (0.07 kg.m^{-3}) than in the previous experimental models ($>1\text{ kg.m}^{-3}$; Parsons et al., 2001).

However, our study shows that we should not simply consider a fixed river-plume sediment concentration threshold because a series of other environmental factors is involved in the generation of turbidity currents by rivers. Below we discuss a new mechanism that explains how dilute river plumes generate turbidity currents.

2.6.2 How do dilute river plumes generate turbidity currents?

Turbidity currents have been generated by the Squamish plume during heightened river discharge ($>250\text{ m}^3.\text{s}^{-1}$) and at low tide (preferentially spring tides) (Hughes Clarke et al., 2014; Clare et al., 2016; Hizzett et al., 2018). Here we discuss the role of these two processes in turbidity current generation. Our results reveal that sediment concentrations are highest in the lower saline layer at low-water during spring tides (Figure 2.6a). Local increased levels of sediment concentration in tidal deltas occur at the interface between the fresh river water and the saline fjord water, this is called the turbidity maximum (Dyer, 1997). Sediment accumulates in this area by the combination of offshore river transport and onshore sediment transport by saline underflow. Where the fresh and salt water meet, they mix and are advected upwards into the mixing layer and away from the delta. The lower velocities in this mixing zone allow sediment accumulation, forming the turbidity maximum; this is often associated with the formation of a fine sediment or fluid mud layer on the seafloor (Allen et al., 1980). Increased river discharge and low tide conditions result in faster flows at the river mouth because more water has to flow through a shallower channel. The higher velocities of the river water pushes the

turbidity maximum away from the delta lip and onto the steeper part of the delta. The ADCP backscatter data shows that increased tidal amplitude results in earlier arrival and a higher concentration turbidity maximum (Figure 2.3). The turbidity maximum on the 15th June is sufficiently concentrated to produce the first positive density gradient (Figure 2.4) in this spring-neap tidal and thus trigger a turbidity current.

Despite more concentrated turbidity maxima at the same location on the 15th and the 16th June, no further turbidity currents were generated. An explanation for this is that episodic remobilisation of seafloor sediment is also needed to trigger (and maintain) a turbidity current. We thus propose that a layer of fine and mobile sediment is deposited on the delta front by turbidity maxima during the neap part of tidal cycle. The first turbidity current removes this sediment and as a result no further turbidity currents are generated. Unconsolidated seafloor sediment have been observed in other active submarine channels (Lintern et al., 2016; Paull et al., 2018).

2.6.3 Global implications for more frequent and widespread turbidity currents

The major implication of our study is that almost all rivers in the global database of Mulder and Syvitski (1995) may be able to generate turbidity currents. We therefore suggest that there are many settings in which turbidity maxima generated turbidity currents may be important. However, because we also show that turbidity current generation is not determined by a simple sediment threshold there is a need for further research in different locations that considers factors such as river discharge, tidal range, seabed-gradient, and sediment settling rates.

More frequent generation of turbidity currents at a wider range of locations globally has important implications. Turbidity currents offshore from river mouths often carry large amounts of organic carbon (Liu et al., 2012). This new mechanism for turbidity current generation will increase the dispersal and burial of terrestrial organic carbon in the deep sea. Our work also has implications for how turbidity currents form thick deltaic deposits within the geological record (Hage et al., 2018), as this new triggering mechanism is likely to have been important during sea-level low stand conditions, when a far larger share of the world's rivers flowed directly on to the continental slope. We thus outline an important new mechanism that links the two most important sediment transport mechanism on our planet - rivers and turbidity currents.

2.7 Conclusion

It was previously thought that rivers needed to exceed a sediment concentration threshold to generate turbidity currents offshore river mouths (e.g. 40 kg.m⁻³, 1 kg.m⁻³ Mulder

and Syvitski, 1995; Parsons et al., 2001). Here we show that rivers with far lower sediment concentrations (0.07 kg.m^{-3}) can produce local turbidity maxima dense enough to generate fast and erosive turbidity currents.

However, these turbidity currents are only generated when fine-sediment, which settled from the dilute plume during lower tidal amplitudes or reduced river discharge levels, is available on the seafloor to be remobilised. Our findings are important because they imply that a far wider range of rivers than previously thought, have the potential to generate turbidity currents, because there is no fixed sediment threshold that must be exceeded. Understanding the mechanism that initiate turbidity currents offshore other river mouths is crucial as this mechanism is the starting point for delivery of terrestrial particles (e.g. pollutants, organic carbon, micro plastics) to the deep sea.

2.8 Acknowledgements

We thank the captains and crews of RV Strickland and RV Heron. The field campaign was supported by Natural Environment Research Council grants NE/M007138/1, NE/M017540/1. S.H. was funded by the National Oceanography Centre (UK) and ExxonMobil. M.J.B.C. was funded by a Royal Society Research Fellowship. D.R.P. acknowledges funding received from the European Research Council (ERC) under the European Union's Horizon 2020 research and innovation programme (Grant agreement No. 725955)". E.LP. was supported by a Leverhulme Trust Early Career Fellowship (ECF-2018-267). The authors declare no conflicts of interest. All data supporting the results of this paper are presented in the paper and/or the supporting information. Additional data and raw values used to produce plots related to this paper are available online at "NOAA data repository" (<https://accession.nodc.noaa.gov/0202076>).

2.9 Supplementary material

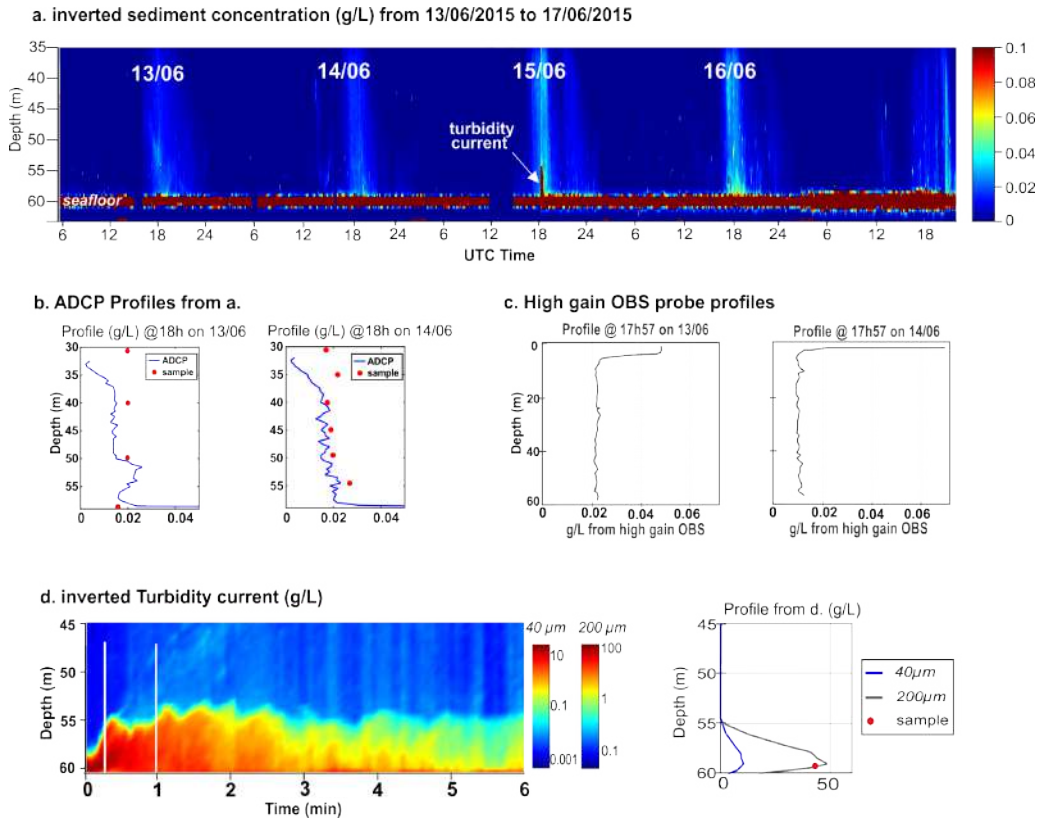


FIGURE 2.7: Acoustic Doppler Current Profiler inversion results (see Fig. 2.1b for ADCP location). a. sediment concentration for 5 days of measurements (mean grain size used for inversion = $40\mu\text{m}$). b. profiles from a. plotted against sediment samples taken at same time/location. c. suspended sediment (g/L) after calibration of high gain probe. d. zoom into turbidity current sediment concentration (D50 grain size used for inversion = 40 and $200\mu\text{m}$)

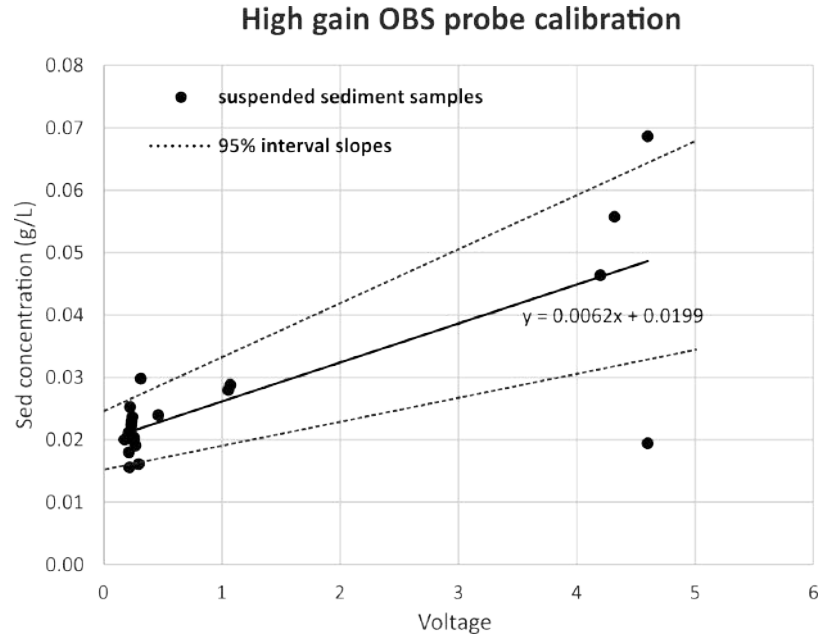


FIGURE 2.8: Calibration curve for the high gain Optical Backscatter probe deployed from the Moving vessel (Fig. 2.1c). Dots are physical samples collected in the water column at the same time as the OBS deployment.

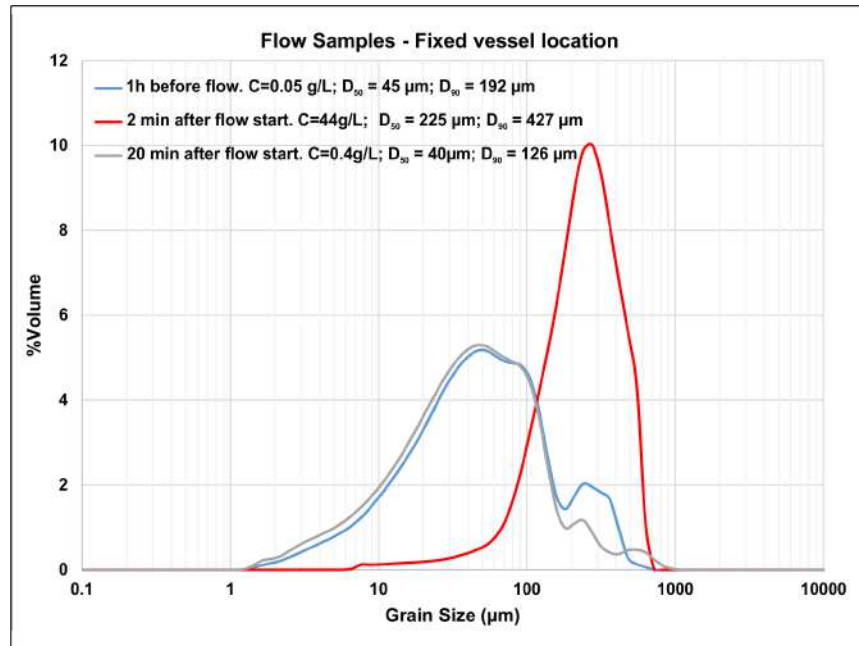


FIGURE 2.9: Grain size distributions of samples taken in the turbidity current from the fixed vessel (see Location in Fig. 2.2). Measurements were performed with a Malvern Mastersizer 2000.

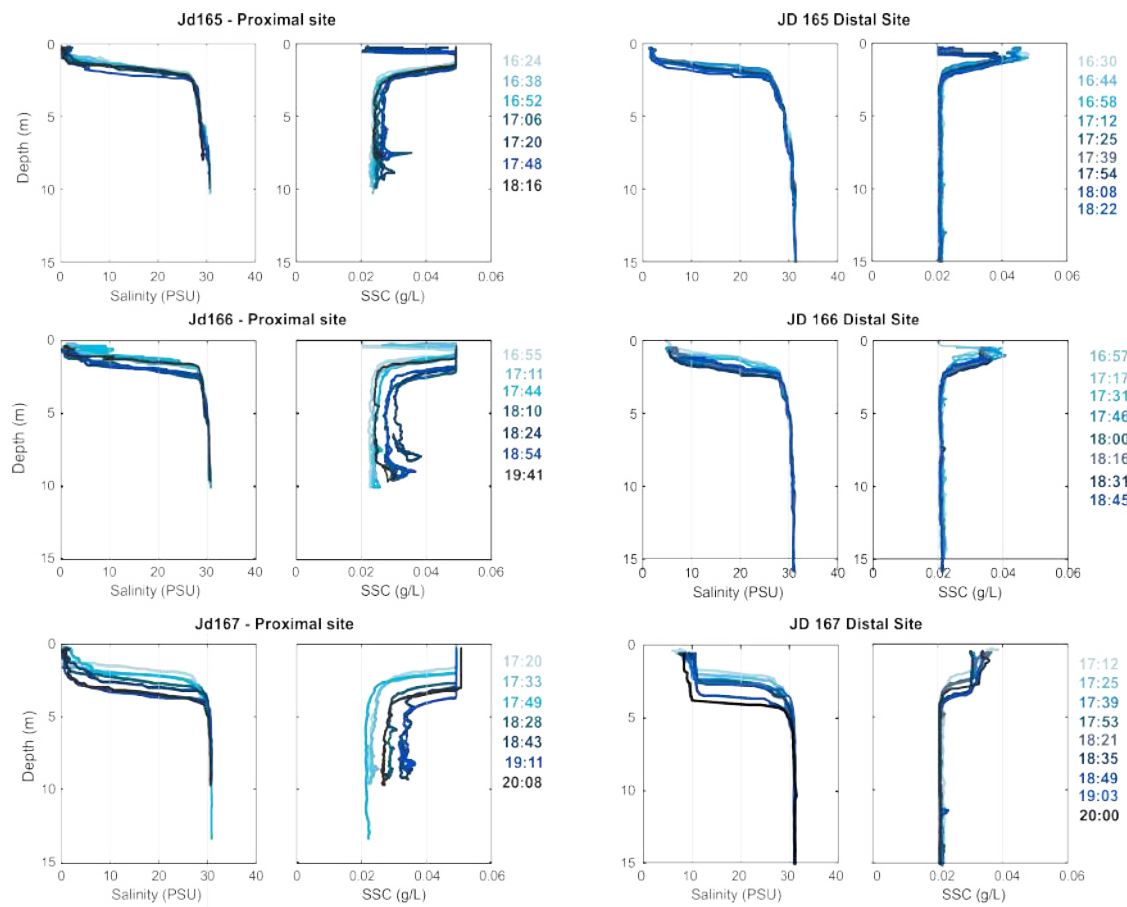


FIGURE 2.10: Salinity and suspended sediment concentration profiles measured at the proximal (15 m water depth) and distal (60 m water depth) compared to the Squamish delta (see Fig. 4 for location). Note: the abrupt cut-off at 0.07 g/L at the proximal site indicates saturation of the instrument. The maximum suspended sediment values are further constrained by direct samples collected in the river shown in Table 2.1.

Date	Time	Location	Depth (m)	g/L
15/06/2015	16:12	River channel exit	0	0.069
15/06/2015	18:15	Plume edge, just downstream of river mouth	0	0.046
16/06/2015	Low tide	River mouth (depth transect)	0	0.084
16/06/2015	Low tide	River mouth (depth transect)	1	0.132
16/06/2015	Low tide	River mouth (depth transect)	2	0.065

TABLE 2.1: Water and sediment samples collected in the Squamish river mouth.

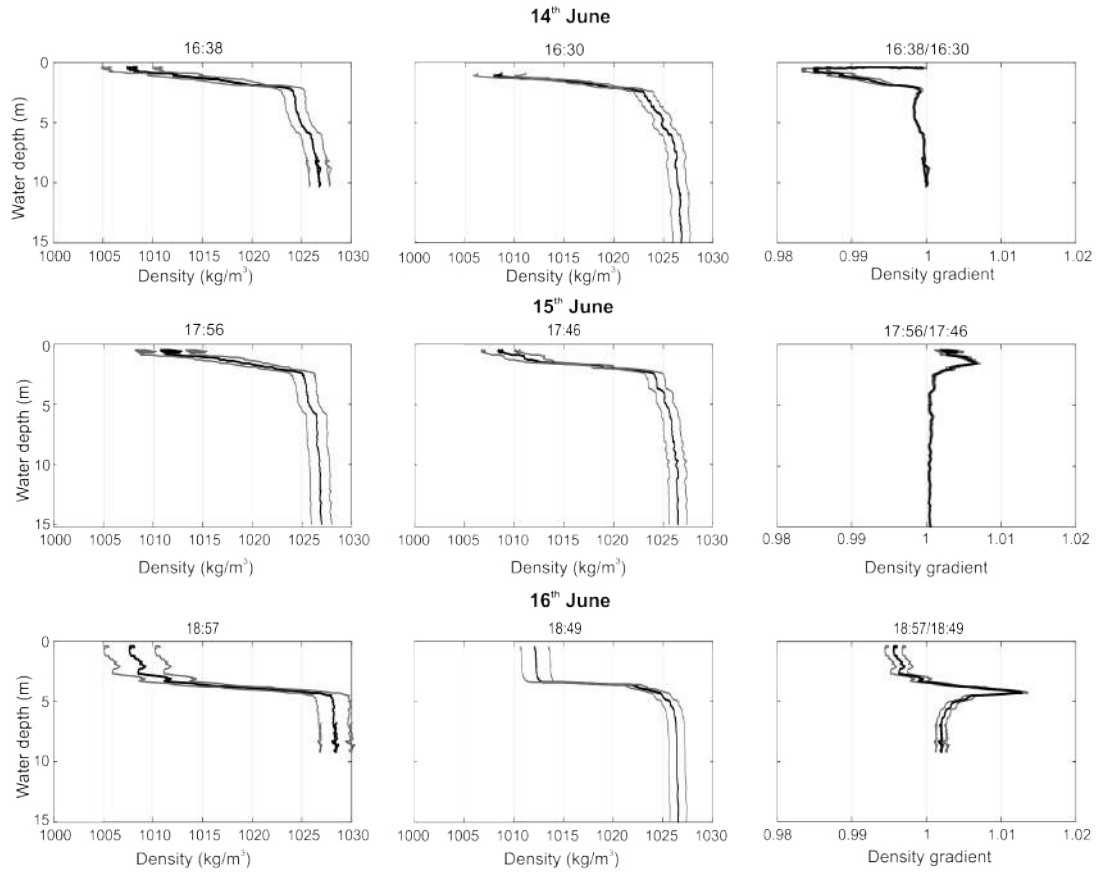


FIGURE 2.11: Examples of water densities and confidence intervals used to compute density gradients shown in Fig. 2.4. Left and central columns: Water density based on salinity, temperature and suspended sediment data for proximal and distal locations. Dashed lines represent the 95% confidence interval based on the suspended sediment values obtained after calibration of the Optical Backscatter Probe. Right column: density gradients shown in Fig. 2.4. Dashed lines are the 95% confidence intervals.

15 th June 2015 turbidity current properties						
a. Max velocity	b. Max sediment concentration measured from physical sample	c. Max thickness	d. Duration	e. Max width	f. Total sediment missing from difference map (Fig. 5B)	g. Total sediment carried by turbidity current based on ADCP inversion (excluding bottom 1 m*)
1.7 m/s	44 kg/m ³	6 m	6 min	80 m	~670 m ³	~180 m ³

TABLE 2.2: Properties of the turbidity current monitored on 15th June 2015 and presented in this study. a. Maximum velocity of the flow front imaged by a forward-looking echosounder as presented in Hage et al. (2018). b. Maximum sediment concentration measured from a sample taken 2 min after the flow started (Fig. S9). c. Maximum thickness documented using acoustic Doppler current profiler backscatter (Fig. 3F). d. Turbidity current duration measured by the acoustic Doppler current profiler (Fig. 3G). e. Maximum width of the flow imaged by a forward-looking echosounder, as presented in Hage et al. (2018). Flow remained confined within the 90 m long submarine channel. f. Total sediment volume lost from the seabed, based on a comparison between two bathymetric surveys collected before and after the turbidity current, Fig. 5B). * Note that this method does not include thin deposits below the resolution of bathymetric mapping, which may reduce this estimate of total sediment volume lost. g. Total sediment volume carried by the turbidity current, based on inversion of backscatter data from the acoustic Doppler current profiler. * Note that the ADCP did not image the bottom meter of the flow, due to acoustic interference with the seabed, and this method may thus underestimate sediment volumes transported by the flow.

Chapter 3

How to recognize crescentic bedforms formed by supercritical turbidity currents in the geologic record: Insights from active submarine channels

This chapter forms a peer-reviewed paper published in *Geology*:

Hage, S., Cartigny, M. J. B., Clare, M. A., Sumner, E. J., Vendettuoli, D., Hughes Clarke, J. E., Hubbard, S. M., Talling, P. J., Lintern, G. D., Stacey, C. D., Englert, R. G., Vardy, M. E., Hunt, J. E., Yokokawa, M., Parsons, D. R., Hizzett, J. L, Azpiroz-Zabala, M., Vellinga, A. J. (2018). How to recognize crescentic bedforms formed by supercritical turbidity currents in the geologic record: Insights from active submarine channels. *Geology* 46(6): 563-566.

Author contributions: M.A-Z., M.J.B.C., M.A.C., S.H., J.L.H., J.E.H.C., J.E.H., D.G.L., C.D.S., E.J.S., P.J.T., M.E.V., A.J.V., M.Y. collected the Squamish field data. S.M.H., R.E., S.H. collected the Gabriola outcrop data. D.V. produced the stratigraphic profile based on repeated time-lapse bathymetry. S.H., M.J.B.C., M.A.C., E.J.S. analysed the data and wrote the manuscript. All authors developed ideas and agreed on the final version of this manuscript.

3.1 Abstract

Submarine channels have been important throughout geologic time for feeding globally significant volumes of sediment from land to the deep sea. Modern observations show that submarine channels can be sculpted by supercritical turbidity currents (seafloor sediment flows) that can generate upstream-migrating bedforms with a crescentic planform. In order to accurately interpret supercritical flows and depositional environments in the geologic record, it is important to be able to recognize the depositional signature of crescentic bedforms. Field geologists commonly link scour fills containing massive sands to crescentic bedforms, whereas models of turbidity currents produce deposits dominated by back-stepping beds. Here we reconcile this apparent contradiction by presenting the most detailed study yet that combines direct flow observations, time-lapse seabed mapping, and sediment cores, thus providing the link from flow process to depositional product. These data were collected within the proximal part of a submarine channel on the Squamish Delta, Canada. We demonstrate that bedform migration initially produces back-stepping beds of sand. However, these back-stepping beds are partially eroded by further bedform migration during subsequent flows, resulting in scour fills containing massive sand. As a result, our observations better match the depositional architecture of upstream-migrating bedforms produced by fluvial models, despite the fact that they formed beneath turbidity currents.

3.2 Introduction

Turbidity currents transfer vast amounts of sediment from land to the deep sea via submarine channels. Deposits of turbidity currents that filled ancient submarine channels are important because they record past fluxes of sediment, organic carbon, and nutrients. There are few direct observations from turbidity currents in action. Even fewer studies have linked direct observations to detailed time-lapse mapping of seafloor change (e.g. Hughes Clarke, 2016) or sedimentary deposits (e.g. Symons et al., 2017). This means that links between flow processes and deposits are much debated (e.g. Ventra et al., 2015; Kane and Hodgson, 2015), with direct implications for reconstructing flows, past environments, and larger-scale sedimentary systems. Here we enable accurate interpretation of these deposits by providing the most detailed study yet of turbidity currents that combines direct flow monitoring, time-lapse seafloor mapping, and sediment coring.

Seafloor mapping has revealed that proximal, sandy submarine channels are often characterized by crescentic bedforms that migrate upstream (Symons et al., 2016). Flow observations in submarine channels (Hughes Clarke, 2016) have connected these upstream-migrating bedforms to flow instabilities, termed cyclic steps (Kostic and Parker, 2006; Spinewine et al., 2009), which can occur at the base of supercritical stratified turbidity

currents (Postma and Cartigny, 2014). Such upstream-migrating bedforms are important, as they can enhance sediment transport efficiency (Sun and Parker, 2005), and may initiate and maintain submarine channels (Fildani et al., 2013; Covault et al., 2014). Prevalence of these upstream migrating bedforms on the modern seafloor (Symons et al., 2016) suggests their deposits should be abundant in the geologic record. However, their depositional signature is poorly constrained due to discrepancies between modeling results and outcrop observations.

Numerical and physical experiments with supercritical turbidity currents suggest they deposit regular back-stepping (dipping up-slope) beds (Spinewine et al., 2009; Postma and Cartigny, 2014; Covault et al., 2017). In contrast, outcrops interpreted as cyclic step deposits are predominantly characterized by scour fills containing massive sand, occasionally in combination with back-stepping beds (Dietrich et al., 2016; Lang et al., 2017; Ono and Bjorklund, 2017). Modern analogues for these massive sands are reported in sediment cores collected from crescentic bedforms in Monterey Canyon (offshore California, USA) (Paull et al., 2011); and similar bedforms have been associated with cyclic steps on Squamish Delta, Canada (Hughes Clarke, 2016). Integration of synoptic measurements from supercritical turbidity currents, associated bedforms, and deposits from a single system are needed to resolve these discrepancies between model predictions and outcrop observations.

3.2.1 Aims

Here we present the first combination of detailed (sub-minute resolution) flow monitoring, high-frequency (near daily) time-lapse seabed mapping, and sediment core data from an active proximal turbidity current system. Our aims are to (1) understand how proximal crescentic bedforms that formed beneath sandy supercritical flows are recorded in the sedimentary record; (2) use these observations to reconcile discrepancies between existing experimental depositional models and outcrop observations; and (3) provide diagnostic criteria to identify crescentic bedforms in the geologic record.

3.3 Study site and Methods

Three turbidity current channels lie on the Squamish River Delta front, which flows into Howe Sound, British Columbia (Figure 3.1). Here we focus on the proximal section of the central channel, which stretches for 600 m, from 40 to 100 m water depth, and contains crescentic bedforms with a wavelength of 20–30 m and height of 2–3 m. In this location, flow observations show that crescentic bedforms result from supercritical flow conditions at the base of turbidity currents (Hughes Clarke, 2016). We studied these bedforms in the central channel over three field seasons (2011, 2015, and 2016)

and now integrate these data to link flow processes with their sedimentary deposits. Ideally, all data would be recorded in the same field season; however, such a data set does not yet exist in any location. Instead, we integrate data collected during three field seasons in which river discharges, turbidity current characteristics, and changes in seafloor morphology were similar (Figure 3.2, Table 3.1) (Hughes Clarke et al., 2014; Clare et al., 2016; Hughes Clarke, 2016).

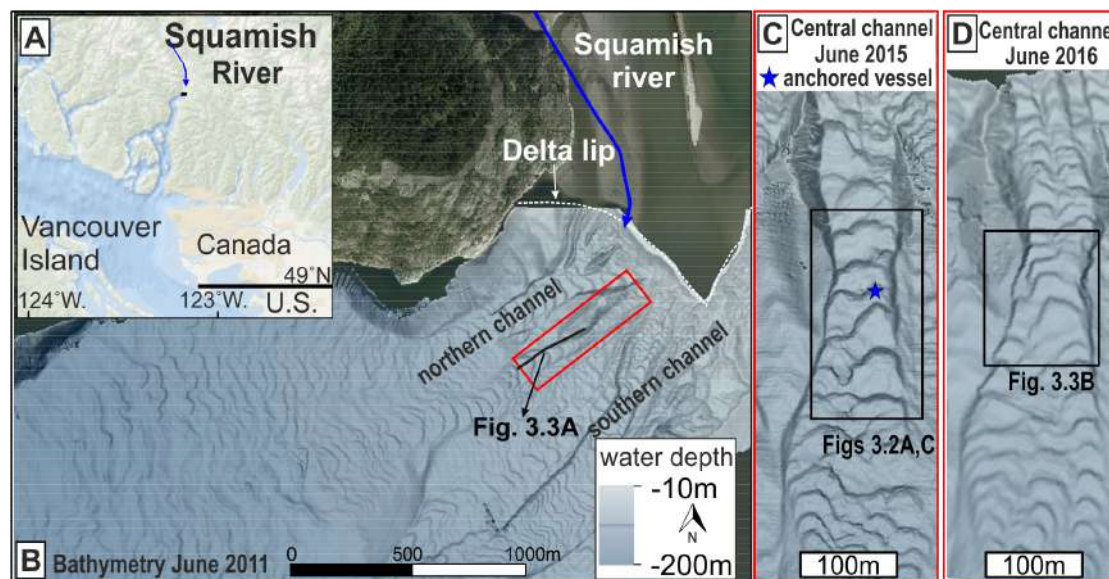


FIGURE 3.1: a: Squamish River location, British Columbia, Canada. b: Three submarine channels covered by crescentic bedforms occur offshore from river-mouth. c: Location of flow dynamics observations in June 2015. d: Location of coring expedition in June 2016.

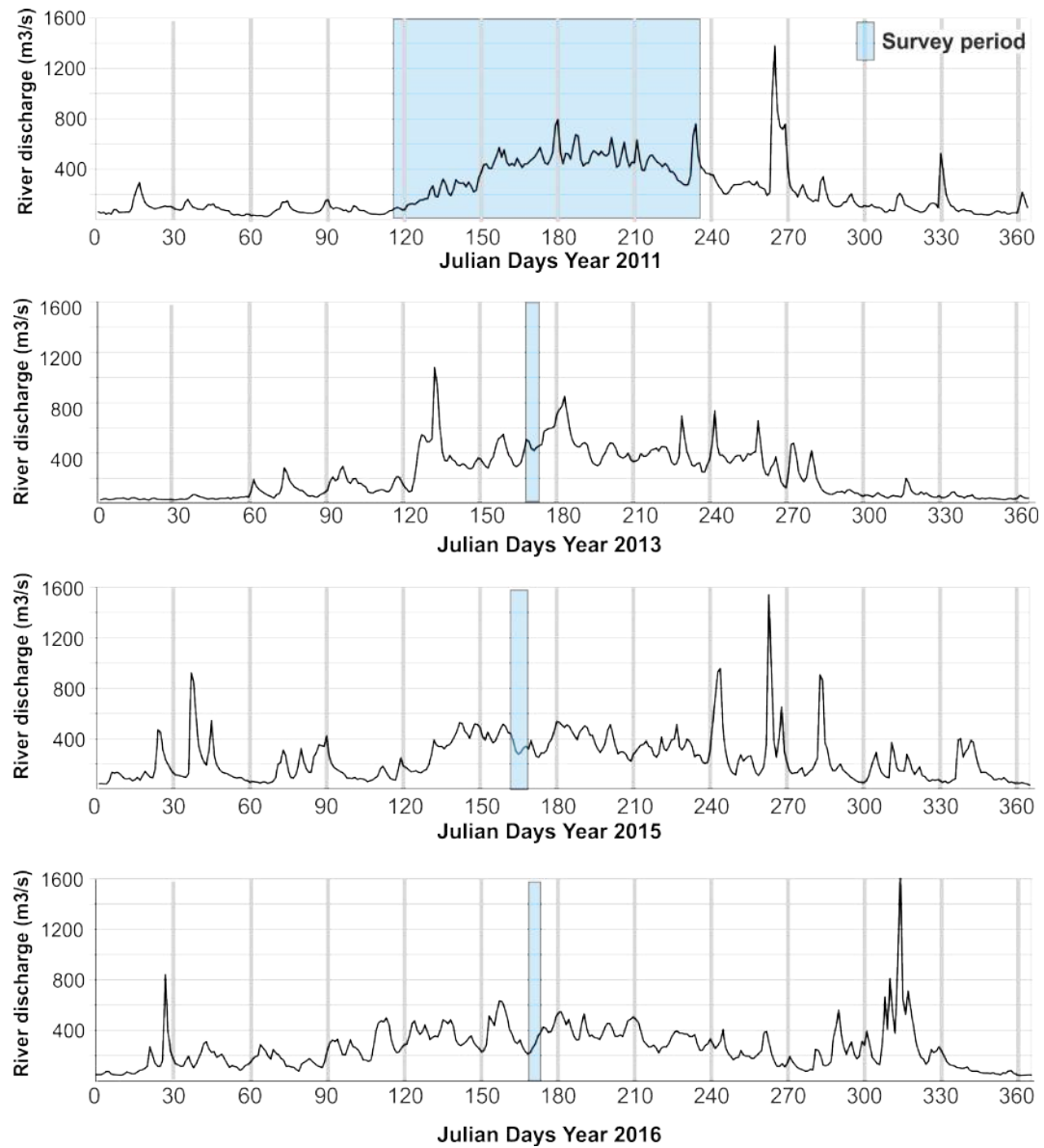


FIGURE 3.2: Squamish River discharge during survey periods at the Squamish Delta presented in this study

Hughes Clarke (2016) monitored 14 flows over 6 days in June 2013. 7 of these flows occurred on 21 st June 2013. 4 (i.e. Flows A, B, C, E) of these 7 flows are presented here.	Hughes Clarke (2016)				This Study
	Flow A	Flow B	Flow C	Flow E	Flow 1
Average Speed (based on forward-looking sonar)	1.9 m/s	2.6 m/s	2.5 m/s	1.6 & 2.5 m/s	1.8 m/s
Planform	~7 m wide leading edge	~8 m wide leading edge	~20 & 10 m wide leading edges	~30 m & 20 m wide leading edges	~20 m wide leading edge
Maximum thickness	6 m	6 m	8.5 m	8 m	7 m
Flow Duration	~7 min	~15 min	~20 min	~8 min	~15 min
Seabed change	5-7 m bedform upstream migration: > 0.1-0.8 m of deposition on stoss sides > up to 1.6 m of erosion on lee sides				1-2 m bedform upstream migration: > 0.25-1 m of deposition on stoss sides > up to 1.0 m of erosion on lee sides

TABLE 3.1: Comparison between flow properties and seabed change described in Hughes Clarke (2016) and in this study

3.3.1 Flow and Seafloor Observations

Flow dynamics were measured in June 2015 using two vessels. The first vessel was moored using four anchors in a water depth of 60 m (Figure 3.1 ; Figure 3.3). Three acoustic instruments were suspended 30 m above the seafloor from this fixed vessel, to measure turbidity currents in three dimensions (c.f. Hughes Clarke, 2016, Table 3.2). Two acoustic sonars imaged flows in both cross section and plan view (Figure 3.2a, 3.3, Movies DR1 and DR2). A 600 kHz acoustic doppler current profiler (ADCP) recorded flow velocity and echo (acoustic backscatter) intensity counts, imaging the current every 3.5 s (Figure 3.4c) . The second vessel enabled mapping of the 250 × 100 m study area every 12 min (Figure 3.5b) using an EM710 multibeam system operating at 70–100 kHz. This repeat survey enabled seafloor changes (e.g., bedform migration) to be directly related to turbidity current measurements.

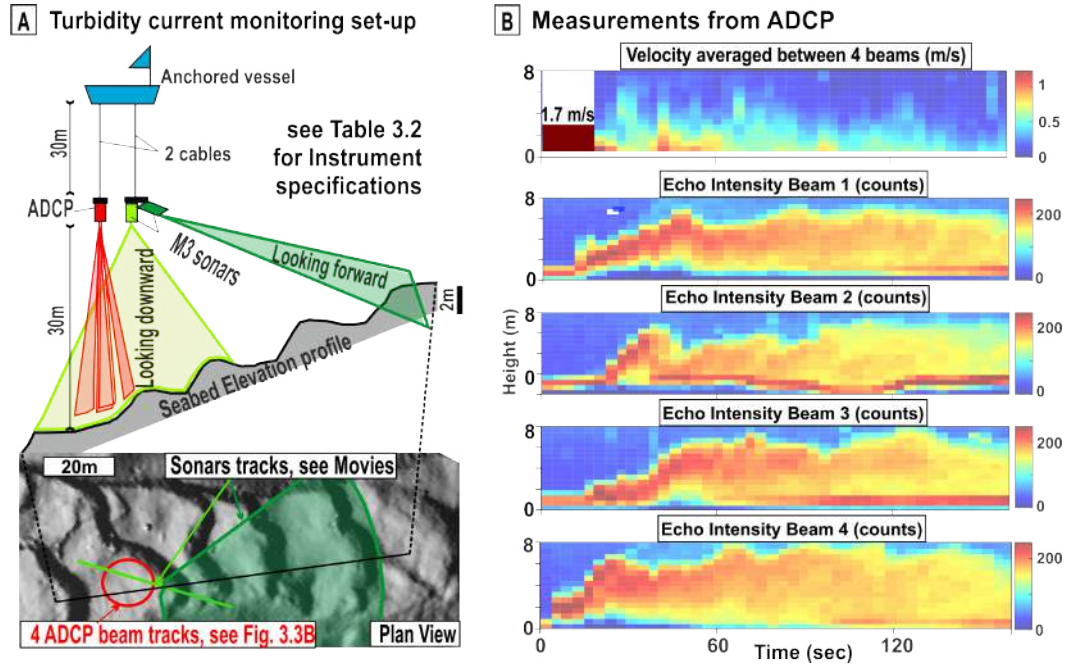


FIGURE 3.3: a. Instrument setup of the turbidity current monitoring carried out in June 2015 in the central submarine channel downstream of Squamish Delta (See Fig. 3.1 for location). Three acoustic instruments were suspended 30 m above the seafloor. Two fixed echosounders imaged the turbidity current every second in a profile view (see Movie DR1) and plan view (see Movie DR2). An Acoustic Doppler Current Profiler comprised of 4 beams measured the flow every 3.5 sec. b. ADCP Measurements on the first 3 min of the flow (see Fig. 3.4b): internal velocities of the flow averaged between the 4 beams (top panel); raw echo intensity returned by each ADCP beam (4 bottom panels).

Instrument Name	Vessel	Configuration	Frequency	Spatial Resolution	Time Interval	Field of view
Teledyne Acoustic Doppler Current Profiler	Anchored	30m above the seafloor Downward-looking	614 kHz	Vertical: 50cm	3.5sec	20°
Kongsberg Multibeam MultiMode (M3) sonar	Anchored	30m above the seafloor Downward-looking	500 KHz	Vertical: 6cm	1sec	3°
Kongsberg Multibeam MultiMode (M3) sonar	Anchored	30m above the seafloor Facing up the Squamish delta (at 45°)	500 KHz	Vertical: 6cm	1sec	30°
EM710 Multibeam Sonar	Survey	Hull-mounted Downward-looking	70-100 kHz	Vertical: 20cm Horizontal: 50cm	12-min repetitive survey	1°

TABLE 3.2: Instrumentation used to monitor turbidity current and associated seafloor evolution

3.3.2 Sedimentary Deposit Observations

Depositional architecture resulting from successive flows was computed using time-lapse seafloor surveys collected in 2011. This data set comprises 93 weekday repeat bathymetric maps of the bedform-covered channel floor (Hughes Clarke et al., 2014). By subtracting each bathymetric survey from the previous day, we detected temporal changes in seafloor elevation during a 4 month period. Sediment gains and losses were then stacked to reconstruct the stratigraphic evolution associated with the upstream-migrating bedforms (Figure 3.3a). Finally, a series of closely spaced cores were collected in June 2016 across two crescentic bedforms (Figure 3.3b). These cores were logged visually and photographed to document the sedimentary facies that characterize upstream-migrating bedforms.

3.4 Results

3.4.1 Flow Monitoring and Seafloor Morphological Change

Here we focus on an individual flow monitored on 15 June 2015 in the central channel (Figures 3.1, 3.3 and 3.4). This 15 min flow was characterized by a maximum frontal velocity of 2 m/s, a maximum thickness of 7 m, and a maximum width of 100 m (Figures 3.4a and c; Movies DR1 and DR2). Echosounder images show that the leading edge of the flow accelerated over the steep lee side of the bedforms (Figure 3.4a; Movies DR1 and DR2). This flow has similar properties to flows previously observed in the northern channel (velocity, dimensions, and duration; Table 3.1). It caused similar movement of bedforms to those shown to result from cyclic steps at the base of supercritical turbidity currents in the 2013 surveys (Hughes Clarke, 2016). Detailed seafloor mapping was conducted simultaneously with the flow observations on 15 June 2015. The observed flow is linked with up to 1.5 m of upstream bedform migration (Figure 3.4b). Deceleration of the flow promoted deposition of 0.25–0.5-m-thick upstream-dipping beds of sediment on the stoss side of bedforms, as shown in the 12 min difference maps (Figure 3.4b).

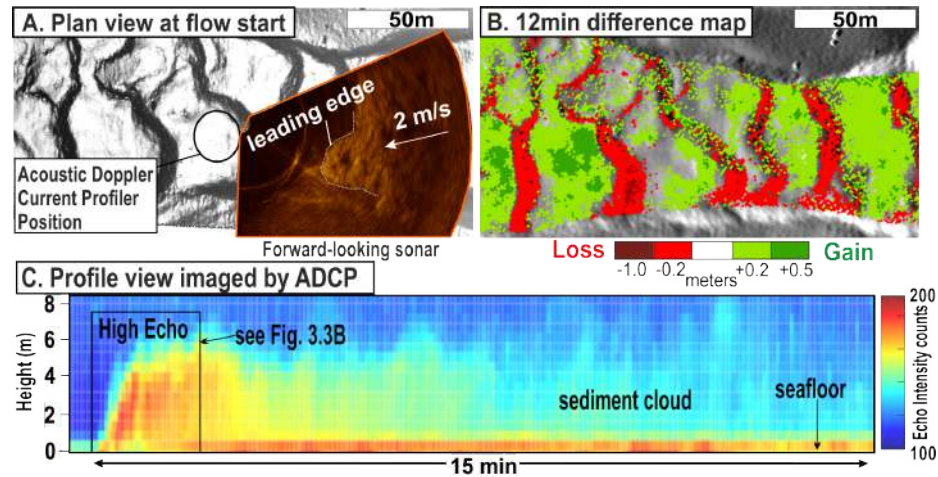


FIGURE 3.4: Observations of a turbidity current linked to crescentic bedforms. A: Snapshot showing a plan view of flow traveling over bedforms. B: Seafloor change during 12 min period after the flow snapshot in A and C. C: Time series of echo intensity recorded by acoustic doppler current profiler (ADCP) backscatter showing turbidity current (location in A).

3.4.2 Deposit Geometry (Seafloor Difference Maps) and Facies (Cores)

Four months of near-daily bathymetric surveys in 2011 allow us to study the stratigraphic architecture that results from upstream migration of crescentic bedforms (Figures 3.5, 3.6a). The uppermost part of the stratigraphy (Figure 3.6a) contains up to 3-m-thick successions of back-stepping beds. Individual back-stepping beds are 0.1–0.5 m thick. These back-stepping beds result from the most recent turbidity current depositing sediment on the stoss side of bedforms, causing bedforms to migrate upstream. Occasionally, large flows cause more significant upstream bedform migration, and erode the seafloor more deeply, producing thicker (1 to 2.5 m) backstepping beds (see Figure 3.5). The lower portion of these thicker backstepping beds is preserved typically as 1–2-m-thick scour fills, as seen in the lower part of the final stratigraphy (Figures 3.5, 3.6a).

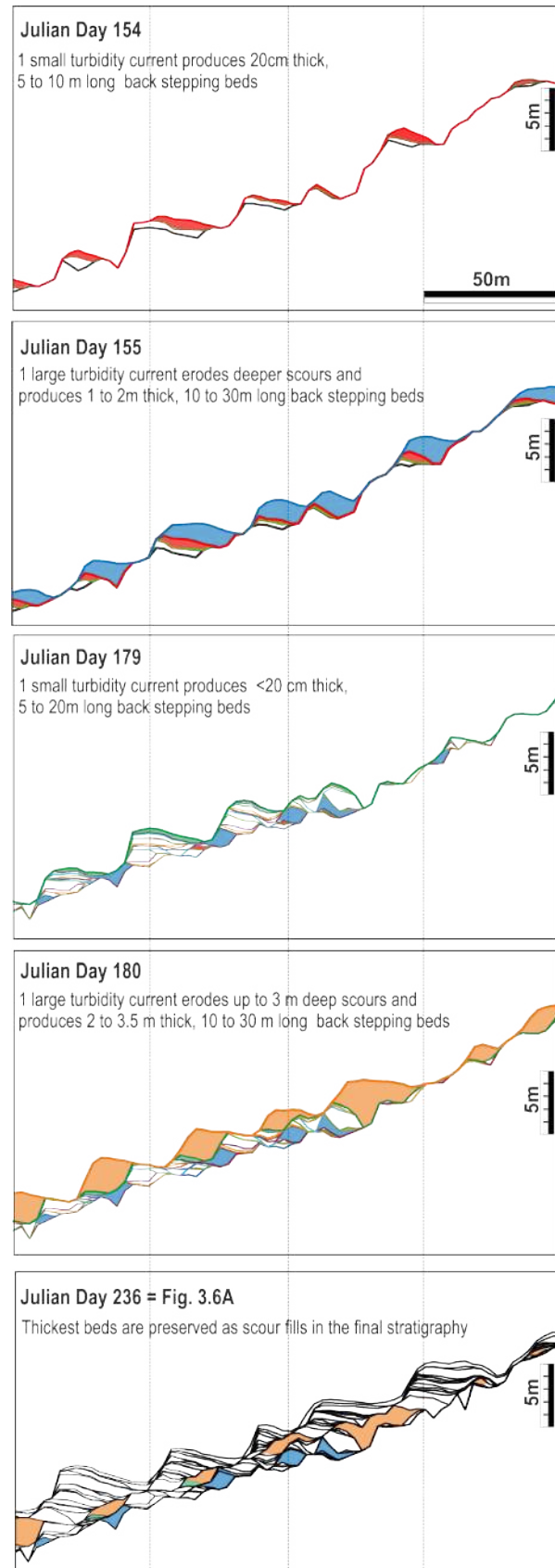


FIGURE 3.5: Seafloor stratigraphy highlighted in colour for 4 turbidity current events, which occurred during the 4-month repeat survey performed in 2011. Each line represents one day of bathymetric survey.

Lastly, we used a set of piston and box cores to sample the sedimentary facies that are associated with both back-stepping beds and scour fills (Figure 3.6b). The sediment cores all contain multiple units of massive sands, which are ungraded to poorly graded, and lack visible sedimentary structures (e.g. laminations). The uppermost sands in two box cores were faintly laminated (cores 8 and 9; Figure 3.6b). The uppermost parts of piston cores can be lost or disturbed during coring, potentially explaining the lack of laminations. Contacts between beds are typically sharp and erosive. Individual beds are therefore inferred to result from individual turbidity currents. Core bases are commonly characterized by 1–2-m-thick sand beds, which likely record infilling of deep scour fills during large flow events. The tops of cores display amalgamated sand beds with thicknesses that correspond to those of backstepping beds recorded by repeat bathymetric surveys (0.1–0.5 m; Figure 3.6a).

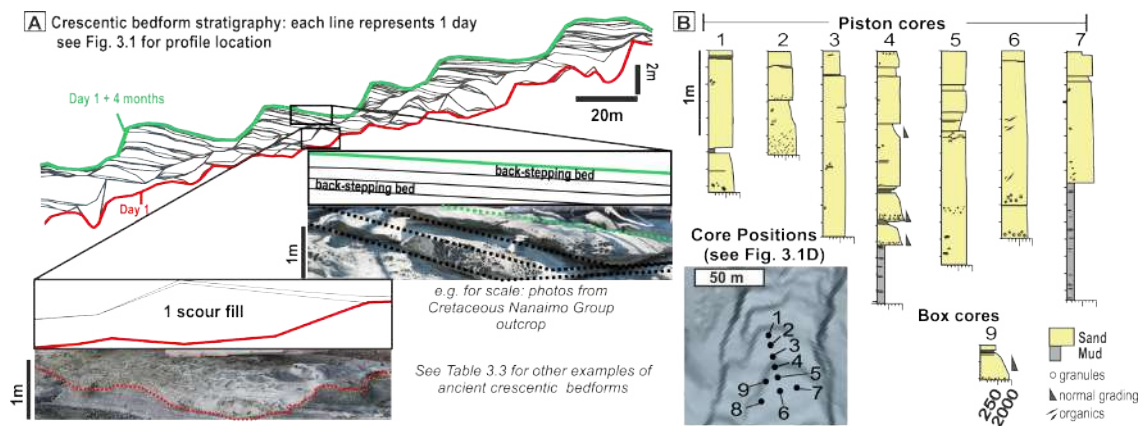


FIGURE 3.6: Crescentic bedform deposits. A: Along-strike stratigraphy computed from 106 bathymetrical surveys, and comparison of the features with ancient crescentic bedform deposits (see Table 3.3). B: Sediment cores showing the facies associated with crescentic bedforms in our study site.

3.5 Discussion

3.5.1 Comparison with Existing Models

Cyclic steps and their deposits have been modeled both in turbidity current settings (e.g. Fildani et al., 2006; Spinewine et al., 2009; Kostic, 2011; Cartigny et al., 2011; Covault et al., 2017) and in fluvial settings (e.g. Yokokawa et al., 2009; Cartigny et al., 2014; Vellinga et al., 2017). Surprisingly, and as described below, our observations better match the depositional architecture of cyclic steps produced by fluvial models rather than those produced by turbidity current models.

Studies of turbidity current bedforms have focused either on the depositional architecture (e.g. Spinewine et al., 2009; Kostic, 2011; Covault et al., 2017), or on the facies characteristics (e.g. Migeon et al., 2001; Postma and Cartigny, 2014) resulting from

cyclic steps. Existing architectural models predict regular back-stepping beds that form via deposition by the thick and slow part of the flow on the stoss side of bedforms. Our observations are consistent with this model, as they show back-stepping beds in the uppermost part of the stratigraphy. However, we also show that these back-stepping beds are subsequently eroded, as bedforms continue to migrate upstream. Thus, ultimately, only the lowest parts of the thickest back-stepping beds are preserved as scour fills. An existing model of cyclic step facies (Postma and Cartigny, 2014) relates the thick and slow part of turbidity currents, located downstream from hydraulic jump, to laminated sands (Bouma, 1962, Bouma's Tb). This model suggests that massive sands (Bouma's Ta) can be formed near the hydraulic jump. In agreement with this model, our cores contain units composed of visually massive sands (Figure 3.6b). However, in contrast to the model, these cores do not contain continuous units of laminated sands visible to the naked eye (Bouma's Tb). The lack of such laminated sand units suggests that near-bed sediment concentrations of individual turbidity currents were sufficiently high to suppress turbulence, thereby depositing massive sands (e.g. Sumner et al., 2008).

Previous models in fluvial settings demonstrate that aggradation rate affects deposit characteristics in supercritical flows (Yokokawa et al., 2009; Cartigny et al., 2014; Vellinga et al., 2017). At one end of the spectrum, high net aggradation rates produce regular back-stepping beds; at the other end of the spectrum, low net aggradation rates produce scour fills. The only geometries preserved in our final stratigraphy are scour fills that result from large flows. Based on analogies with fluvial models, we infer that large flows produce higher aggradation rates, thus producing thicker sands that have better preservation potential.

3.5.2 Recognition of Supercritical Flow Deposits in the Geologic Record

We synthesize the three data sets into a single block diagram to illustrate the relationships among flow, seafloor morphology, and subsurface deposit architecture (Figure 3.7). This diagram provides diagnostic criteria to recognize crescentic bedform deposits produced by cyclic steps beneath sandy turbidity currents. Deposit architectures can range between two end-members: (1) regular back-stepping beds that correspond to a more complete preservation, and (2) scour fills containing massive sands that correspond to less-complete preservation. The preservation potential of these bedforms depends on both the magnitude of the turbidity currents and net aggradation rates.

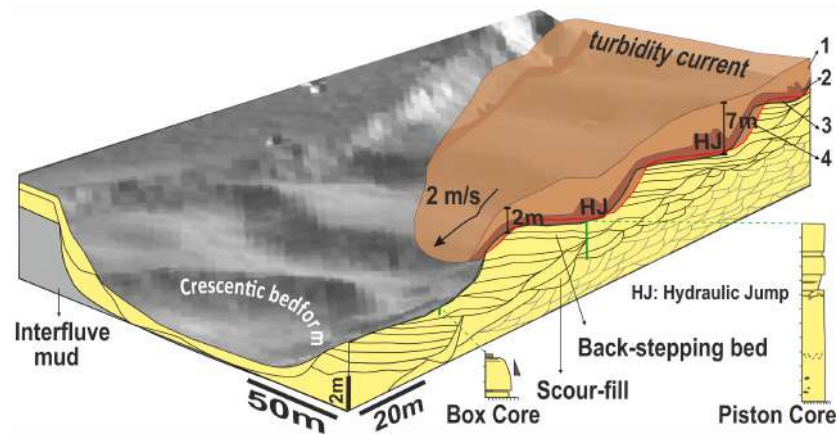


FIGURE 3.7: Summary schematic of crescentic bedforms formed by supercritical turbidity currents and their depositional architecture. 1— low-density upper part of the flow; 2—high-density lower part of the flow, with hydraulic jumps due to changing gradient over bedforms; 3—deposition; 4—erosion by active event. Red line corresponds to the resulting bathymetry after a single flow. Black lines are observations from Figure 3.6a. Gray lines are predictions.

Comparable architectures have been described in many paleo-environments, such as deltas, submarine channels, and glaciolacustrine settings (e.g. Ponce and Carmona, 2011; Lang and Winsemann, 2013; Postma et al., 2014; Ventra et al., 2015; Bain and Hubbard, 2016; Dietrich et al., 2016; Lang et al., 2017; Ono and Bjorklund, 2017). For example, individual 1–2-m-thick and 5–15-m-long scour fills containing massive sandstone have been observed in multiple outcrops worldwide (Figure 3.6a, Table 3.3) Lang and Winsemann, 2013; Postma et al., 2014; Bain and Hubbard, 2016; Dietrich et al., 2016; Lang et al., 2017). These examples also feature back-stepping beds that are 0.5–3.0 m thick and 10–40 m long (Figure 3.6a, Table 3.3). We infer that these examples formed from supercritical flows with variable net aggradation rates and magnitude, since they show both back-stepping beds and scour fills composed of massive deposits. Outcrops characterized exclusively by back-stepping beds that are suggestive of purely aggradational conditions are rare (e.g. Ponce and Carmona, 2011; Ventra et al., 2015, Table 3.3).

In conclusion, this unique combination of flow monitoring, repeat mapping, and deposit sampling enables accurate identification of crescentic bedforms and supercritical flow deposits within proximal submarine channels.

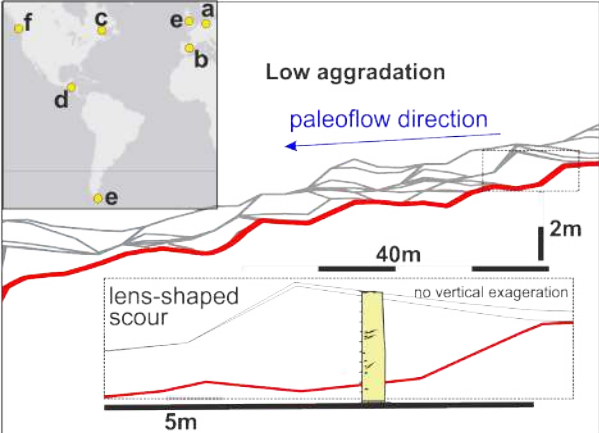
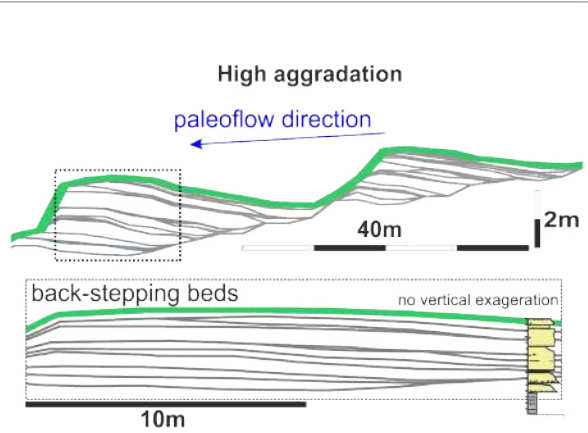
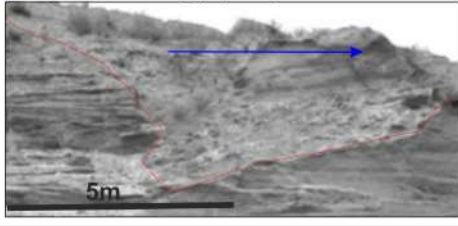
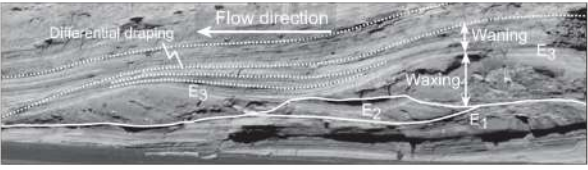


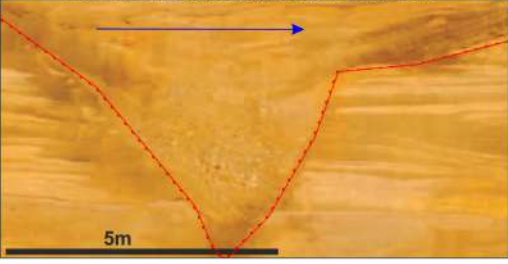
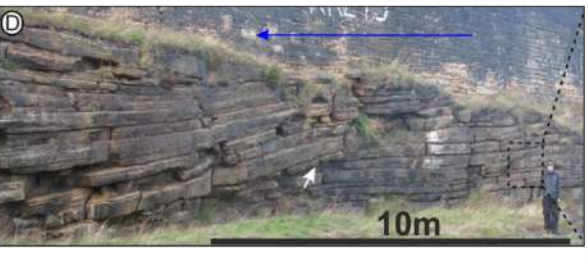

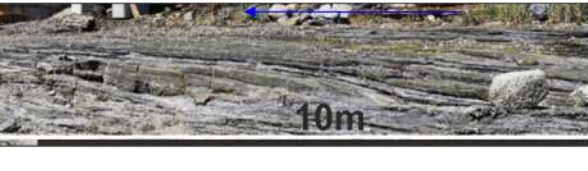
 <p>Low aggradation</p> <p>paleoflow direction</p> <p>lens-shaped scour</p> <p>no vertical exaggeration</p> <p>40m</p> <p>2m</p> <p>5m</p>	 <p>High aggradation</p> <p>paleoflow direction</p> <p>back-stepping beds</p> <p>no vertical exaggeration</p> <p>40m</p> <p>2m</p> <p>10m</p>
<p>1. Middle Pleistocene glacial lake-outburst flood deposits, Germany (a) Lang and Winseman, 2013</p>  <p>5m</p>	<p>6. Hyperpycnal clinoform systems, Miocene deposits of the Austral foreland basin, Argentina (e) Ponce and Carmona, 2011</p>  <p>Flow direction</p> <p>Differential draping</p> <p>Waning</p> <p>Waxing</p> <p>E₃</p> <p>E₂</p> <p>E₁</p>
<p>2. OGEX mega bed in distal part of the Miocene Buho canyon, Spain (b) Postma et al., 2014</p>  <p>5m</p>	<p>7. Mateo outcrop, Late Miocene turbidite sequence of the Sorbas Basin, Spain (b) Postma et al., 2014</p>  <p>10m</p>
<p>3. Proglacial sandur Pleistocene delta, Gulf of St Lawrence, Quebec (c) Dietrich et al., 2016</p>  <p>5m</p>	<p>9. Late Carboniferous delta front deposits, Pennine Basin, United Kingdom (e) Ventra et al., 2015</p>  <p>10m</p>
<p>5. deepwater channel-levee complex from Sandino Forearc Basin, Nicaragua (d) Lang et al., 2017</p>  <p>5m</p>	<p>10. Late Cretaceous deep-water strata from the Nanaimo Group, BC Canada (f) Bain and Hubbard, 2016</p>  <p>10m</p>

TABLE 3.3: Comparison between deposits of this study and examples of outcrop studies interpreted as sandy supercritical flow deposits

3.6 Acknowledgements

Hage is funded by the National Oceanography Centre (UK) and ExxonMobil. We thank the captains and crews of CCGS Vector, RV John Strickland, and CSL Heron. We thank D. Piper, Z. Sylvester, A. Normandeau, and Editor J. Schmitt for insightful reviews. We acknowledge Natural Environment Research Council funding (grants NE/M007138/1, NE/M017540/1, NE/P009190/1, and NE/P005780/1).

3.7 Supplementary movies

Supplementary movies showing the turbidity current in plan view and cross-section views can be accessed on the Geology Journal data repository: <http://www.geosociety.org/datarepository/2018/>

Chapter 4

Efficient burial of young terrestrial organic carbon by submarine turbidity currents

This chapter forms a paper currently in review in *Geology*: **Hage, S.**, Galy, V., Cartigny, M. J. B., Acikalin, S., Clare, M. A., Grocke, D.R., Hilton, R.G., Hunt, J.E., Lintern, D.G., McGhee, C.A., Parsons, D. R., Stacey, C.D., Sumner, E.J., Talling, P. J. (in review, *Geology*). Efficient preservation of young terrestrial organic carbon in sandy turbidity current deposits.

Author contributions: M.J.B.C, M.A.C., S.H., J.E.H., D.G.L., D.R.P., C.D.S, E.J.S., P.J.T carried out turbidity current monitoring, coring and sampling in Bute Inlet. S.A., D.R.G., S.H., C.A.M. performed bulk organic carbon geochemistry. S.H. and V.V.G. performed analysis by ramped oxidation. S.H., V.V.G., M.J.B.C analyzed the data. S.H., V.V.G, M.J.B.C. wrote the manuscript. All authors developed ideas, commented and approved the final version of this manuscript.

4.1 Abstract

Burial of terrestrial biospheric organic carbon in marine sediments removes CO₂ from the atmosphere, regulating climate over geologic timescales. Rivers deliver terrestrial organic carbon to the sea, whilst turbidity currents transport river sediment further offshore. Previous studies have suggested most organic carbon resides in mud-dominated marine sediment deposits. However, turbidity currents can carry a significant component of coarser sediment, which is often assumed to be organic carbon poor. Here, using data from a Canadian fjord, we show that young woody debris is rapidly buried within the upper-sand layers of turbidity current deposits (turbidites). These layers have organic

carbon contents that are 10 times higher than the overlying mud layer and overall, woody debris makes up >70 % of the organic carbon preserved in the turbidity current deposits. Burial of woody debris in sand-layers overlain by mud-caps reduces their exposure to oxygen, thus turbidity currents increase organic carbon burial efficiency. Sandy turbidity current channels are common and widespread in fjords and the deep sea; therefore previous global organic carbon burial budgets may have been underestimated.

4.2 Introduction

Burial of terrestrial biospheric particulate organic carbon (POC) in marine sediments is key to constrain as it represents the second largest sink of atmospheric CO₂ after weathering of silicate minerals (Gaillardet et al., 1999), and thereby contributes to the long-term regulation of climate (Berner, 1982; Hayes and Waldbauer, 2006). Rivers transfer terrestrial organic carbon to the marine environment, and contribute up to about half of the global organic carbon burial flux to the oceans (Galy et al., 2015; Burdige, 2007). Previous work concerning preservation of terrestrial organic carbon in oceanic sediments has generally focussed on fine-grained marine mud (e.g. Mayer, 1994). Indeed, organic carbon preferentially binds to fine-grained phyllosilicates which are characterized by high specific area, thus facilitating terrestrial organic carbon export and preservation (e.g. Keil et al., 1997). Conversely, coarser-grained marine sands are thought to play a negligible role in global organic carbon burial (Burdige, 2007). However, woody debris associated with coarse sands is important for terrestrial organic carbon budgets in some highly erosive rivers (West et al., 2011; Turowski et al., 2016). Furthermore, sand often makes up a significant fraction of terrigenous material delivered to the coast, e.g. sand can be up to 50 % of the total suspended sediment load during high river discharge (Milliman and Meade, 1983). These coastal sands can be transported offshore by turbidity currents, which dominate the deposition of sediment across vast areas of the seabed (Bouma et al., 2012). The importance of coarse woody debris was recently shown to be important in one of the largest fan worldwide (Bengal fan, Lee et al., 2019). Despite this, the relative contribution of coarse POC transported by sandy turbidity currents have compared to fine sediment has not been considered.

In contrast to turbidity currents, river transport of particulate organic carbon (POC) from land to the coast is relatively well-studied (Galy et al., 2015). POC transported by rivers typically is a mixture of (Blair and Aller, 2012): 1) young carbon currently produced by photosynthesis in the biosphere (e.g. plant and woody debris); 2) old biospheric carbon issued from degraded soil organic matter and; 3) petrogenic carbon, i.e. ancient (¹⁴C free) carbon derived from erosion of rocks. In contrast to biospheric carbon, the burial of petrogenic carbon recycles carbon between different geologic reservoirs, and does not affect long-term CO₂ levels (Galy, Beyssac, France-Lanord and Eglinton, 2008). It is thus crucial to differentiate between the types of POC, as they have different

effects on atmospheric CO₂ levels. The fluxes of POC mixtures have been constrained in rivers where the POC composition is controlled by erosion rates and sediment yield (Galy, France-Lanord and Lartiges, 2008; Hilton et al., 2012; Clark et al., 2013; Turowski et al., 2013; Galy et al., 2015). However, less is known about the relative fluxes of POC types beyond the coast; in particular the effect of hydrodynamic sorting of POC by the turbidity currents.

Turbidity currents form many of the largest sediment accumulations on Earth (Bouma et al., 2012). Suspended particles (including POC) settle out as turbidity currents decelerate, resulting in deposits called turbidites (Bouma, 1962). Turbidites are typically subdivided into a basal massive coarse sand (Ta), overlain by sequence of an upward fining sand (Tb), followed by cross-laminated sands (Tc), parallel laminated fine sand (Td) finally draped by mud (Te). While terrestrial organic carbon has been identified through presently active submarine canyons (e.g. Biscara et al., 2011; Kao et al., 2014; Stetten et al., 2015), so far, no study has systematically assessed the distribution of POC types into each unit of recent (<2 months old) turbidites. The turbidite units in which each POC type resides affects its burial depth, and hence exposure to oxidants and final burial efficiency. The distribution of POC mixtures in turbidites is of global significance, as a single turbidity current can transport more sediment than the annual suspended sediment flux of the world's rivers combined (Talling et al., 2007; Hunt et al., 2013).

For the first time, here we assess, the distribution of three POC types (sand-sized young biospheric, old biospheric, and petrogenic POC) buried in turbidites that resulted from a turbidity current monitored in Bute Inlet, Canada. These new results determine the preservation potential of coarse, young, terrestrial POC in a modern sandy system, where turbidites are linked to their parent flows initiated from two rivers.

4.3 Results

4.3.1 River and turbidite sampling in Bute Inlet

Bute Inlet is a 80 km long, 4 km wide fjord in British Columbia, Canada (Figure 4.1). Water depths range between 200 and 650 m. Waters are density-stratified throughout the year, with very low dissolved oxygen values (<2 ml/L) in deep water (Pickard and Giovando, 1960). At the fjord head are two deltas associated with the Homathko River and the Southgate River, which provide 75 % and 19 % of the freshwater input to the fjord, respectively (Farrow et al., 1983). The Homathko River has an average annual sediment load of 4.3×10^6 t/yr (Milliman and Syvitski, 1992). The major source of sediment for both rivers is glacial till of granitic composition. River discharges are controlled by the annual melt of glaciers (Prior et al., 1987). Seafloor mapping reveals

a 50 km long submarine channel which is maintained by turbidity currents during the
freshet (Prior et al., 1987; Bornhold et al., 1994; Conway et al., 2012).

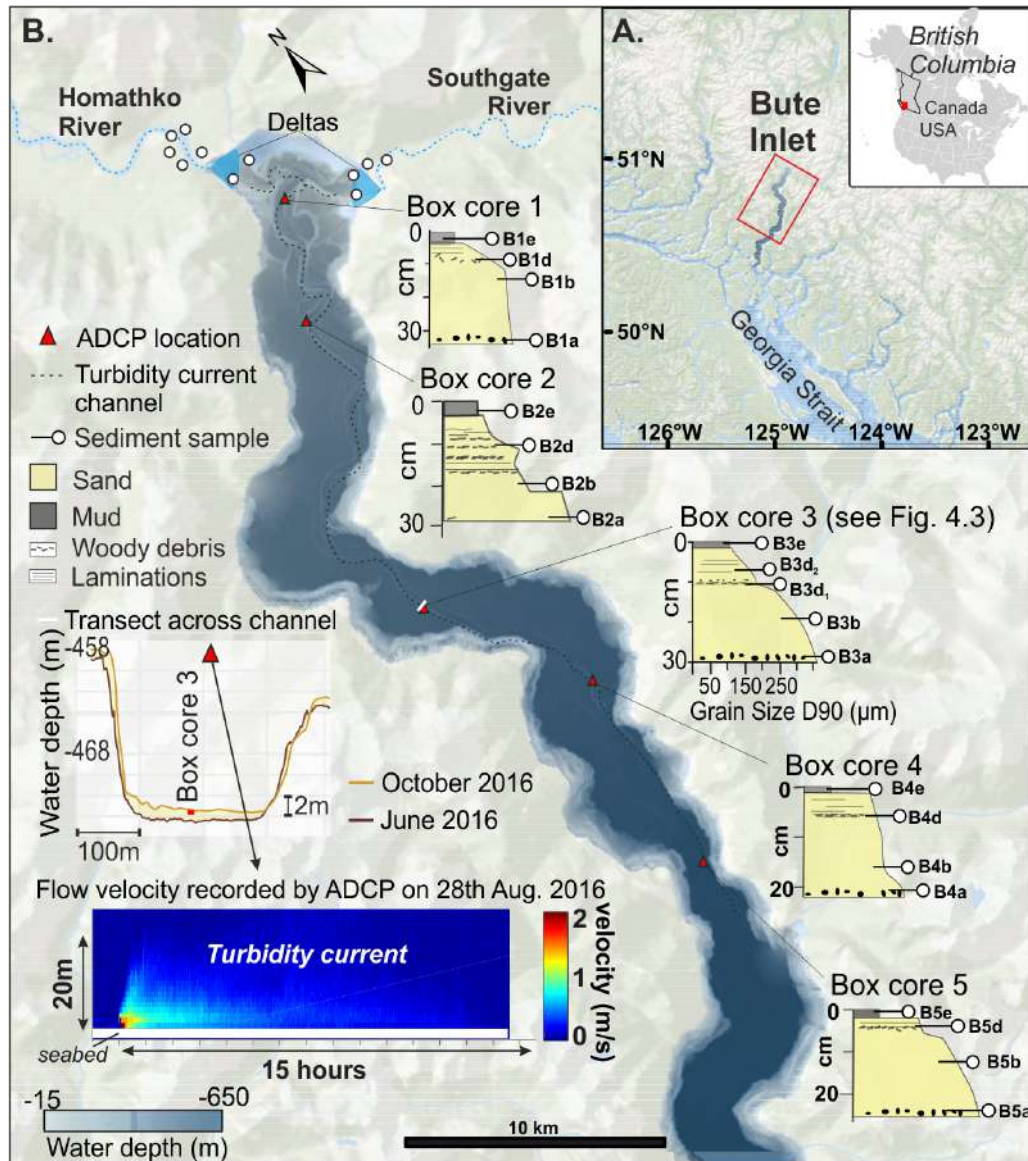


Figure 1. A. Bute Inlet location. B. Bute Inlet bathymetry showing the incised submarine channel starting at the river deltas and terminating ~40 km downstream of the rivers; Example of 1 turbidity current measured by an Acoustic Doppler Current Profiler (ADCP) suspended 20 m above the seabed; Sediment cores and samples used in this study.

FIGURE 4.1: a. Bute Inlet location. b. Bute Inlet bathymetry showing the incised submarine channel starting at the river deltas and terminating 40 km downstream of the rivers; Example of 1 turbidity current measured by an Acoustic Doppler Current Profiler suspended 20 m above the seabed; Sediment cores and samples used in this study. Box cores were collected at the following water depths (from Core 1 to 5): -216 m; -315 m; -478 m; -555 m; -615 m.

To characterize the composition of POC flushed into the fjord, we sampled both rivers (deltas, river banks, and suspended sediments along river depth profiles, Figure 4.1b). Samples were analysed for grain size, total organic carbon (TOC) content and carbon

stable isotopes ($\delta^{13}\text{C}$ expressed in ‰). $\delta^{13}\text{C}$ values are commonly used to characterize organic matter provenance (e.g. discriminate marine from terrestrial sources, Gaines et al., 2009). Similar bulk analyses were performed on samples from box cores collected on the fjord seafloor. Box cores reveal 30-cm-thick turbidites which resulted from turbidity currents that were measured by five Acoustic Doppler Current Profilers (ADCP) deployed in the fjord from June to October 2016 (Figure 4.1b).

In order to characterize the distribution of multiple OC sources in river sediments and turbidites, we used the ramped oxidation system (RPO; Hemingway et al., 2017). This system identifies POC fractions based on thermal lability by heating each sample from 20 °C to 1000 °C in an oxygenated carrier gas, thus sequentially combusting POC into CO_2 . The CO_2 collected between user-defined temperature intervals (“fractions”) was measured for carbon stable isotopes and radiocarbon content (expressed as Fraction modern, Fm) on selected sample (i.e. 2 river samples and samples from Box core 3; ??) to characterize the distribution of OC source and age. Finally, we used RPO combustion profiles to calculate the distribution of the energy needed to combust OC (i.e. activation energy, E_a ; Hemingway et al., 2017). E_a is used as a proxy to characterize OC bond-strength, which reflects the thermal energy required to oxidize each carbon atom when exposed to a particular reaction pathway (Hemingway et al., 2019).

4.3.2 Organic carbon in rivers and turbidites

Bulk measurements for total carbon and total organic carbon (TOC) content reveal that all samples from rivers and turbidites contain exclusively organic carbon (i.e. no carbonates; suppl. Figure 4.5), which is consistent with 1) the absence of carbonate rocks in the Homathko and Southgate river catchments and 2) negligible contributions of marine productivity to turbidites. We describe below the composition of POC in the rivers, the properties of the turbidity currents flowing down the fjord and the composition of POC in the resulting turbidites.

Suspended sediment samples from rivers have relatively elevated TOC (up to 1%) while sands samples from banks and deltas show lower TOC values (Figure 4.2b; down to 0.01 %). River banks and deltas show POC mixtures spanning a higher range of activation energy and becoming more complex (i.e. containing more CO_2 spikes in the ramped oxidation thermograms, Figure 4.3), compared to the river suspended sediment samples. Bulk carbon stable isotope compositions are depleted (-28 to -25.5‰) for all river samples (Figure 4.2a), which is in line with a terrestrial plant origin of POC (Gaines et al., 2009). Although all sampling occurred in October, the samples cover a wide range of grain size and environments (banks, suspended load, deltas).

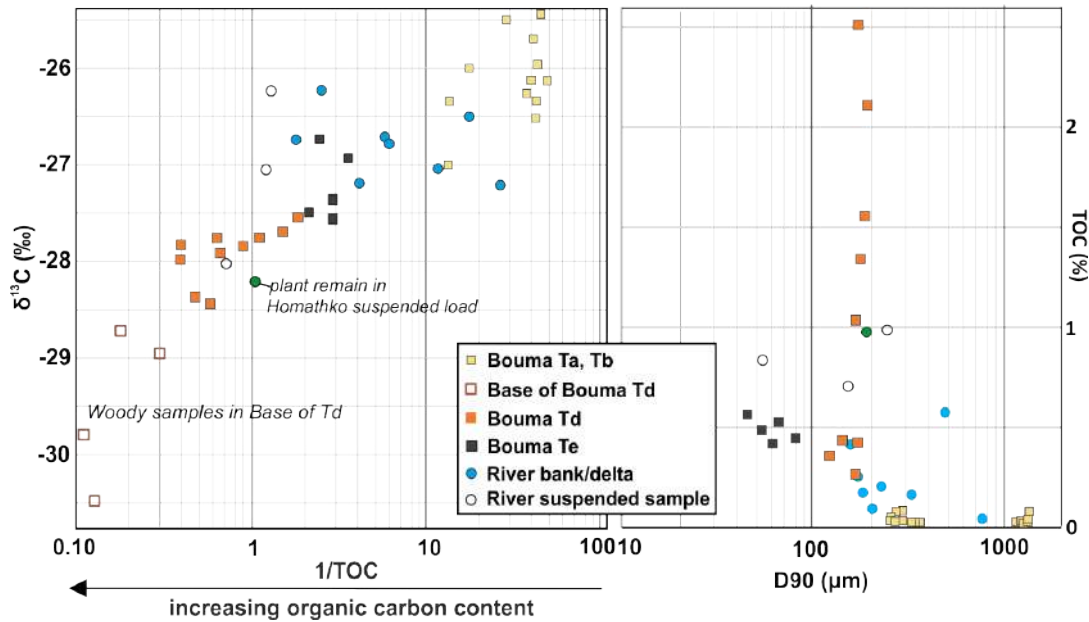


FIGURE 4.2: a. Total organic carbon (TOC) content versus carbon stable isotopes ratios ($\delta^{13}\text{C}$) for bulk samples displayed in Figure 4.1b. b. Sample grain size (D_{90} in micrometers) versus total organic carbon content.

Once those riverine POC mixtures reach the fjord head, they are carried offshore by turbidity currents (Bornhold et al., 1994). Turbidity currents in Bute Inlet are up to 20 m thick, run out for up to 40 km, last for more than 15 hours and reach velocities of 2.5 m/s (e.g. Figure 4.1b). Difference maps between June and October 2016 reveal that the 16 measured flows produced areas of net erosion or net deposition of more than 1m (Figure 4.1b).

We now describe the distribution of POC mixtures found in the turbidites, sampled by five box cores through those areas of recent deposition. We infer that the turbidites were emplaced by the last monitored flow, which was detected by five Acoustic Doppler Current Profilers on 28th August 2016 (Figure 4.1b). A layer of pebbles at the base of the turbidites is interpreted as a gravel lag that represents the first sediment deposited by the turbidity current (Mutti et al., 2003).

Turbidites in the five box cores shows low bulk stable isotope compositions ($\delta^{13}\text{C} = -31$ to -25.5 ‰), which implies negligible addition of marine organic carbon (Figure 4.2a). The relationship between TOC and grain size in turbidites differs starkly from that observed in rivers. The turbidite fine sands (Td) show a TOC enrichment (TOC = 2 to 5 %) compared to their riverine counterpart (TOC = 0.5 to 1 %). This enrichment is due to the presence of woody debris that is visible to the naked eye in the turbidites. Wood-rich samples show depleted $\delta^{13}\text{C}$ values (-32 to -28 ‰), have modern radiocarbon signatures ($\text{Fm} > 1$, based on box core 3), and comprise POC fractions that span low to mid activation energy ($E_a < 225$ kJ/mol; Figures 4.3, ??). Similarly to the sandy samples from the rivers, sand units at the turbidite base (Bouma Ta, Tb) show low

TOC content and span mid to high activation energy (E_a between 150 and 290 kJ/mol; Figure 4.3). ^{14}C compositions from box core 3 reveal that those coarse sandy samples are dominated by aged carbon ($F_m = 0.65$ and 0.73 in Bouma Ta and Tb resp.). Finally, the turbidite mud cap (Te) has a similar composition to the muddy samples collected in the suspended sediments from the rivers (TOC = 0.5 to 0.8 %, $\delta^{13}\text{C} = -27.5$ to -26.5 ‰, $E_a < 210$ kJ/mol, Figure 4.3). ^{14}C activities reveal that POC found in this mud cap is older ($F_m = 0.92$) compared to the underlying silt.

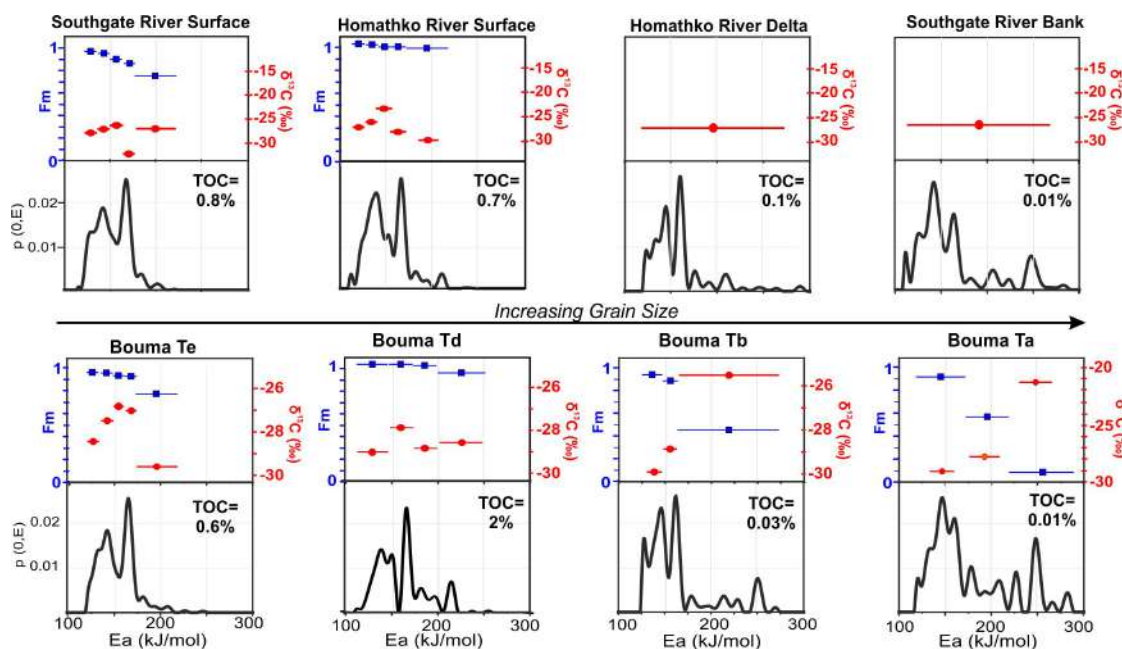


FIGURE 4.3: Separation of Organic Carbon mixtures by ramped oxidation for river and turbidite samples (from Box core 3, Figure 4.1b). Black lines: distribution of activation energy (thermogram). Blue squares: radiocarbon ages (Fraction modern) measured for each collected fraction. Red dots: carbon stable isotopes ($\delta^{13}\text{C}$ in ‰) for each collected gas fraction. TOC = Total Organic Carbon content for each sample.

4.4 Abundance of woody debris in turbidites

We found three types of organic carbon, which are defined based on $\delta^{13}\text{C}$, E_a and ^{14}C from Box core 3 (Figure 4.4, suppl. Figure 4.7). We note that the ramped oxidation method does not result in a perfect separation of POC mixtures into highly resolved peaks representing pure carbon types, hence the following three types correspond to the major component included in each mixture. First, young biospheric terrestrial carbon dominates (≥ 90 %) Bouma Td, and corresponds to non-degraded woody debris. Second, old biospheric terrestrial carbon is found in all Bouma intervals but in different proportions. This second type shows F_m values < 1 , suggesting it results from POC aging in soils. Third, petrogenic carbon (derived from erosion of rocks) is found in significant amounts in coarse Bouma intervals Ta and Tb.

We extrapolated the proportions of those three carbon types to each turbidite divisions and TOC content of the studied turbidites. We found that a turbidite sequence captures: (Figure 4.4c): 1) 75 % of non-degraded woody debris mostly associated with fine sand (Bouma Td); 2) 24 % of aged and altered carbon from soil dominantly found in the fine mud cap (Bouma Te); 3) 1 % of petrogenic carbon mainly associated with sand (Bouma Ta,b). Hydrodynamic sorting of particles by turbidity currents thus concentrates wood-derived young organic carbon in the uppermost layer (Td), which are rapidly buried under 2-6 cm thick mud units (Te). This is important because the young organic carbon associated with woody debris is then protected from oxidation by the mud cap that prevents O₂ penetration thus drastically decreasing oxic exposure time, a key driver of OC degradation in marine sediments (Hartnett et al., 1998; Hemingway et al., 2019). This protection will depend on the thickness of overlying (Te) mud, which can range from a few centimetres to tens of meters in other locations globally (e.g. Rothwell et al., 1998; Sumner et al., 2012).

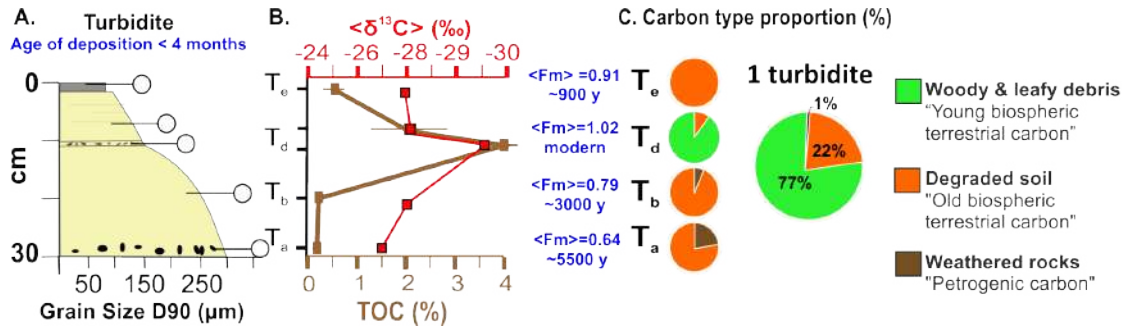


FIGURE 4.4: Summary. a. Turbidite sequence with sample location. b. Total organic carbon content, carbon stable isotopes and radiocarbon ages measured on bulk samples collected in Bouma units from a. v. Carbon types proportions based on Bouma unit thickness, TOC content and separation by ramped oxidation (see Figure 4.3 and suppl. Figure 4.7)

Our results contrast with the general idea that most of the organic matter preserved in marine sediments is associated with mud, whose inorganic matrix would physically protect the organic matter from oxidation (Mayer, 1994; Burdige, 2007). Physical protection is likely to occur in the mud cap described at the top of the studied turbidite and it is supported by ¹⁴C depletion (Fm = 0.92) of the mineral-bound organic matter present in the mud cap. In contrast, here we show that most (75 %) of the organic matter found in a turbidite sequence is made of young, undegraded woody debris associated with silt to fine sand sediments protected by the mud cap.

4.5 Discussion

Although our findings relate to the deposit of one turbidity current in a sandy channel, which is likely to be reworked by successive turbidity currents (Conway et al., 2012;

Vendettuoli et al., 2019), they provide important insights into the hydrodynamic sorting of POC by sandy turbidity currents. Constraining such processes in fjords (e.g. Bute Inlet) is key, as fjords are estimated to account for 11 % of organic carbon burial in marine sediments globally (Smith et al., 2015). Here we suggest that this budget could have been underestimated because the sampling locations of the global study did not consider the seafloor morphology and notably ignored the sandy slopes (as mentioned by Smith et al., 2015). The sandy turbidity current channel in Bute Inlet has a high sedimentation rate (>40 mm/year, Table 4.1; Milliman and Syvitski, 1992; Syvitski et al., 1987) but only covers 16 % of the total fjord area. While this areal proportion seems small, the sandy channel preserves large quantities of terrestrial undegraded organic matter (up to 5 % TOC) in rapidly deposited thin layers of silt to fine sands (i.e. a few hours, see Figure 4.1). These young organic carbon-rich fine sands are buried within a turbidite deposit that has an overall weighted mean of 0.7 % TOC (suppl. Figure 4.7). The rest of the fjord area (84 %) is made of mud, which potentially includes older and less abundant TOC (0.5 %, see mud cap in Figure 4.1), with a sedimentation rate of 10 mm/year (Syvitski et al., 1987; Stacey et al., 2019, see Materials and Methods). We thus estimate that the turbidity current channel buries at least the same amount of organic carbon as the mud in the remaining fjord area (Table 4.1). Such estimates remain to be tested for other turbidites in Bute and for other fjords that could be characterised by different O₂ levels, water stratification and seafloor morphology.

	Sandy channel/Lobe	Fines outside the channel
Weighted mean TOC (%)	0.7	0.5
Surface area (km²)	58	295
Sedimentation rate (mm/year)	41	10
Volume of organic carbon annually (m³/year)	16,646	14,750

TABLE 4.1: Comparison between sandy channel and fine sediments outside the channel in terms of total organic carbon (TOC) content, surface area, sedimentation rate and total organic carbon buried per year. See Materials and methods for sedimentation rates estimates

Global estimates of carbon fluxes in the ocean (e.g. Burdige, 2007; Blair and Aller, 2012) currently posit that sandy fractions are free of terrestrial POC. Yet a recent study (Lee et al., 2019) has found abundant woody debris associated with sand in the Bengal fan for the last 19My. Other studies have reported the presence of organic-rich layers in

sandy deep-sea turbidites (Saller et al., 2006; Zavala et al., 2012; Sparkes et al., 2015), sometimes even within Ta and Tb sands, depending on the organic debris density and size (McArthur et al., 2016; Schnyder et al., 2017). In order to update the current global carbon fluxes (Burdige, 2007), the relative abundance of coarse POC (woody debris) versus fine POC needs to be further investigated. The ramped oxidation method used in this study provides a mean to quantify this relative abundance.

4.6 Materials and methods

4.6.1 Separation of organic carbon mixtures by ramped oxidation

We used the ramped oxidation method to identify the types and proportions of POC preserved in the turbidite sequence (Figure 4.3).

Sample preparation

All samples analysed in the ramped oxidation system were acidified by fumigation using 12 mol/L HCL for 72 hours at 60 °C in order to remove any potential carbonates.

General principle

The ramped oxidation method separates different carbon structures based on thermal lability by heating each sample in an oxygenated oven, thus combusting particulate carbon into CO₂ (Rosenheim et al., 2008; Hemingway et al., 2017). CO₂ concentrations were measured by an infrared gas analyser in part per million (ppm). The energy required to activate combustion was modelled following Hemingway et al. (2017). Resulting ppm CO₂ were plotted against energy of activation (Ea) in a “thermogram”.

Trapping and quantification of gas fractions

The CO₂ produced from combustion in the oven was transferred through a vacuum line to a series of cryogenic traps, and was split between user-defined temperature intervals. For each sample we collected between 3 and 5 CO₂ gas fractions which were then quantified based on pressure measurements and were sealed into pre-combusted pyrex tubes containing 100mg CuO and 10mg Ag pellets. All sealed tubes were finally combusted at 525 °C for 1 h in order to remove any trace contaminant gas. The proportion (%) of each gas fraction compared to the initial sample was calculated based on the total amount of CO₂ combusted from a given sample.

Isotope measurement

Each sealed fraction was measured for stable carbon isotope ratios (¹³C/¹²C) and radiocarbon isotopes ratios (¹⁴C / ¹²C) at the National Ocean Sciences Accelerator Mass

Spectrometry (Woods Hole Oceanographic Institution, USA). Stable carbon isotope ratios are reported in $\delta^{13}\text{C}$ relative to the Vienna Pee Dee Belemnite and were measured using an Isotope Ratio Mass Spectrometer as described in McNichol, Osborne, Gagnon, Fry and Jones (1994). Small splits issued from the ramped oxidation fractions were graphitized following the established methods of the NOSAMS facility (McNichol, Jones, Hutton, Gagnon and Key, 1994). Radiocarbon isotopes were then measured on these fractions and on process blanks using an Accelerator Mass Spectrometer. Radiocarbon isotopes are expressed as Fraction modern (Fm). Fraction modern is a measurement of the deviation of the ($^{14}\text{C}/^{12}\text{C}$) ratio of a sample from *modern*. *Modern* is defined as 95 % of the radiocarbon concentration in 1950 of Oxalic Acid I normalized to $\delta^{13}\text{C} = -19\text{‰}$.

4.6.2 Identification of organic carbon types and calculation of their proportions for the turbidite

Below we describe the methods used to identify POC types preserved in the turbidite sequence and to quantify their relative proportions compared to the overall sequence (Figure 4.4, suppl. Figure 4.7).

Identification of POC types per sample

We use results of ^{14}C , Ea and $\delta^{13}\text{C}$ in order to define three types of POC (suppl. Figure 4.7). A gas fraction was defined as:

A. “young biospheric carbon” if (in order of priority):

1. $\text{Fm} > 1$, and
2. $\text{Ea} > 200 \text{ KJ/mol}$, and
3. $\delta^{13}\text{C}$ $[-30 \text{ to } -26\text{‰}]$

B. “old biospheric carbon” if (in order of priority):

1. $\text{Fm}]0 - 1]$, and
2. $\text{Ea} < 220 \text{ KJ/mol}$, and
3. $\delta^{13}\text{C}$ $[-30 \text{ to } -26\text{‰}]$

C. “Petrogenic carbon” if (in order of priority):

1. $\text{Fm} = 0$, and
2. $\text{Ea} > 220 \text{ KJ/mol}$, and
3. $\delta^{13}\text{C}$ $[-30 \text{ to } -26\text{‰}]$

The limit young versus old biospheric carbon was set at 200 kJ/mol because we ran pure debris of wood into the RPO and they finished the combustion before 200 KJ/mol. Petrogenic carbon was set at 220 KJ/mol based on the analysis of OC-poor river and Ta unit sands in turbidites. Our threshold is slightly higher than the one used in Hemingway et al. 2018 (185 kJ/mol) for petrogenic carbon in Taiwan. This is because the granitic rocks in our river catchments have lower concentrations and more highly refractory petrogenic C than the Taiwanese rocks analysed in (Hemingway et al., 2018).

If a gas fraction did not satisfy the three criteria, its expression on the thermogram was further divided into sub-fractions in order to satisfy the three conditions of one POC type. For example, fraction 3 of Bouma Tb sample (suppl. Figure 4.7) originally had a $F_m = 0.44$ and an E_a that ranged from 150 to 275 KJ/mol. As it satisfies the old biospheric criteria 1 ($F_m \geq 0 - 1$) but it does not satisfy old biospheric criteria 2 ($E_a < 220$ KJ/mol), we divided this peak spectrum into sub-fractions F3a (< 220 KJ/mol in green on suppl. Figure 4.7) and F3b (> 220 KJ/mol in brown on suppl. Figure 4.7). Since F3b is radiocarbon free ($F_m = 0$), we recalculated the F_m of F3a by using the average value of fraction 3 ($F_m = 0.44$), with a weight corresponding to the area above 220 KJ/mol.

Calculation of a carbon budget for the entire sequence

Once the carbon types proportions were defined for each sample, we estimated a global budget for the entire turbidite sequence based on: 1) the sedimentary volume of each Bouma unit compared to the whole sequence; 2) the total organic carbon content for each Bouma unit (see Table 4.2).

	a = Thickness (cm)	b = Unit part in total deposit (%) $a/Σ(a)*100$	c = TOC (%)	d = Carbon part per Bouma unit $b*c/100$	e = Part of petrogenic carbon in unit TOC (%) (based on RPO results, Fig. S7)	f = Part of old biospheric carbon in unit TOC (%) (based on RPO results, Fig. S7)	g = Part of young biospheric carbon in unit TOC (%) (based on RPO results, Fig. S7)	h = part of petrogenic carbon in total deposit TOC $e*d/100$	i = part of old biospheric carbon in total deposit TOC $f*d/100$	j = part of young biospheric carbon in total deposit TOC $g*d/100$
Ta	2.0	6.7	0.1	0.0	24.9	73.6	0.0	0.002	0.005	0.000
Tb	18.0	60.0	0.2	0.1	7.0	93.0	0.0	0.006	0.084	0.000
Td1	1.0	3.3	4.5	0.2	0.0	12.0	88.0	0.000	0.018	0.132
Td2	7.0	23.3	2.0	0.5	0.1	9.7	90.2	0.001	0.045	0.421
Te	2.0	6.7	0.5	0.0	0.1	99.9	0.0	0.000	0.033	0.000
								0.009	0.185	0.553
								1.2	24.8	74
								0.75 Sum		
								%		

TABLE 4.2: Values and calculations used to obtain the proportions of organic carbon types in a turbidite.

4.6.3 Comparison of TOC fluxes between sandy channel and fines outside the channel

Surface areas

The surface areas of the sandy channel/lobe and the rest of the fjord were estimated in ArcGis based on a bathymetry map acquired in 2008 which covers the whole fjord (Conway et al., 2012).

Total organic carbon (TOC) content

TOC for the sandy channel corresponds to the weighted average of TOC contained in each sedimentary unit of the studied turbidite (suppl. Figure 4.7), according to their relative thickness. We assume the rest of the fjord is covered by fine sediment only as a broad approximation. Grab samples and sediment cores collected outside of the sandy channel show that these sediments have mostly similar grain size and TOC content as the mud cap of the turbidites. Fines outside of the channel are sourced either from the turbidity current over spills or from slow settling of the river plumes in the proximal parts of the fjord. Fines related to the turbidity current over spills are inferred to have a similar organic carbon composition as the mud cap (i.e. mostly old biospheric organic carbon). However, organic carbon composition in the fines related to slow settling from the plumes remains unresolved.

Sedimentation rate

Syvitski et al. (1986) provide a range of 1 – 300 mm/year depending on the location in Bute Inlet. Given this wide range, we further estimated sedimentation rates for the fines outside the channel and for the sandy channel based on other approaches. First, we used a value of 1 cm/year as the sedimentation rate for the fines outside the channel, as estimated on long cores dominated by mud in a distal location of Howe Sound, i.e. a fjord similar (in terms of sedimentary processes and connection with rivers) and close to Bute Inlet (Stacey et al., 2019). Second, we used the Homathko River annual sediment load (4.3×10^6 t/yr, Milliman and Syvitski, 1992) to estimate the amount of sand (with a density of 1800 kg/m^3) delivered to the sandy channel and lobe areas (58 km^2). This conservative approach resulted into a sedimentation rate of 41 mm/year (Table 4.1), i.e. nearly one order of magnitude lower compared to the maximum value provided by Syvitski et al., (1985).

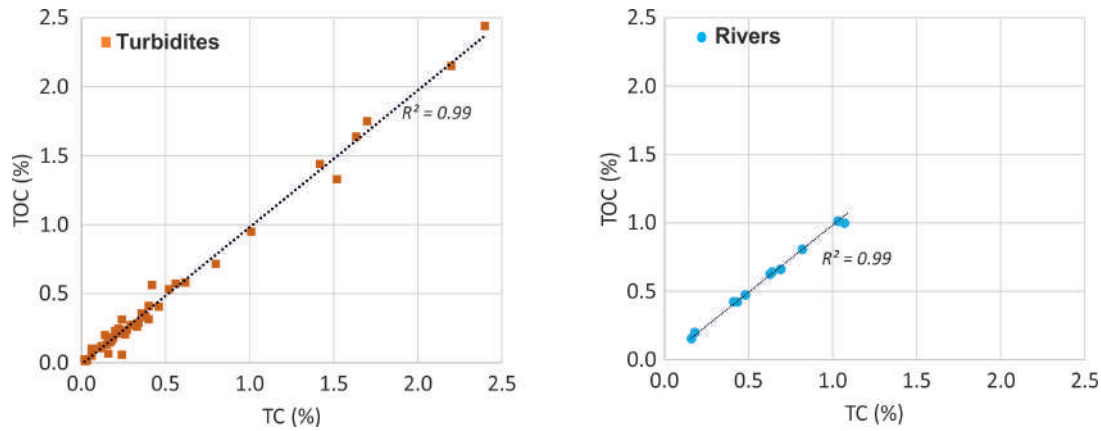


FIGURE 4.5: Total Organic Carbon (TOC) content versus Total Carbon (TC) content in turbidite and river samples. TC was measured by a VarioMax Elemental CNS Macro Elemental Analyzer. TOC was measured by LECO elemental carbon analyzer after acidification by rinsing with 4mol/L hydrochloric acid.

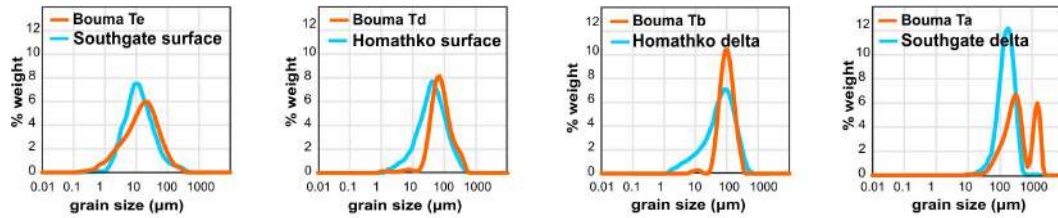


Figure 6: Grain Size distributions of samples analysed by ramped oxidation and displayed in Fig. 3

FIGURE 4.6: Grain Size distributions for river and turbidite samples displayed in Figure 4.3. Measurements were performed using a Malvern Master sizer 2000 at the National Oceanography Centre Southampton (UK). %weight corresponds to the relative amount of particles by mass relative to the total sample.

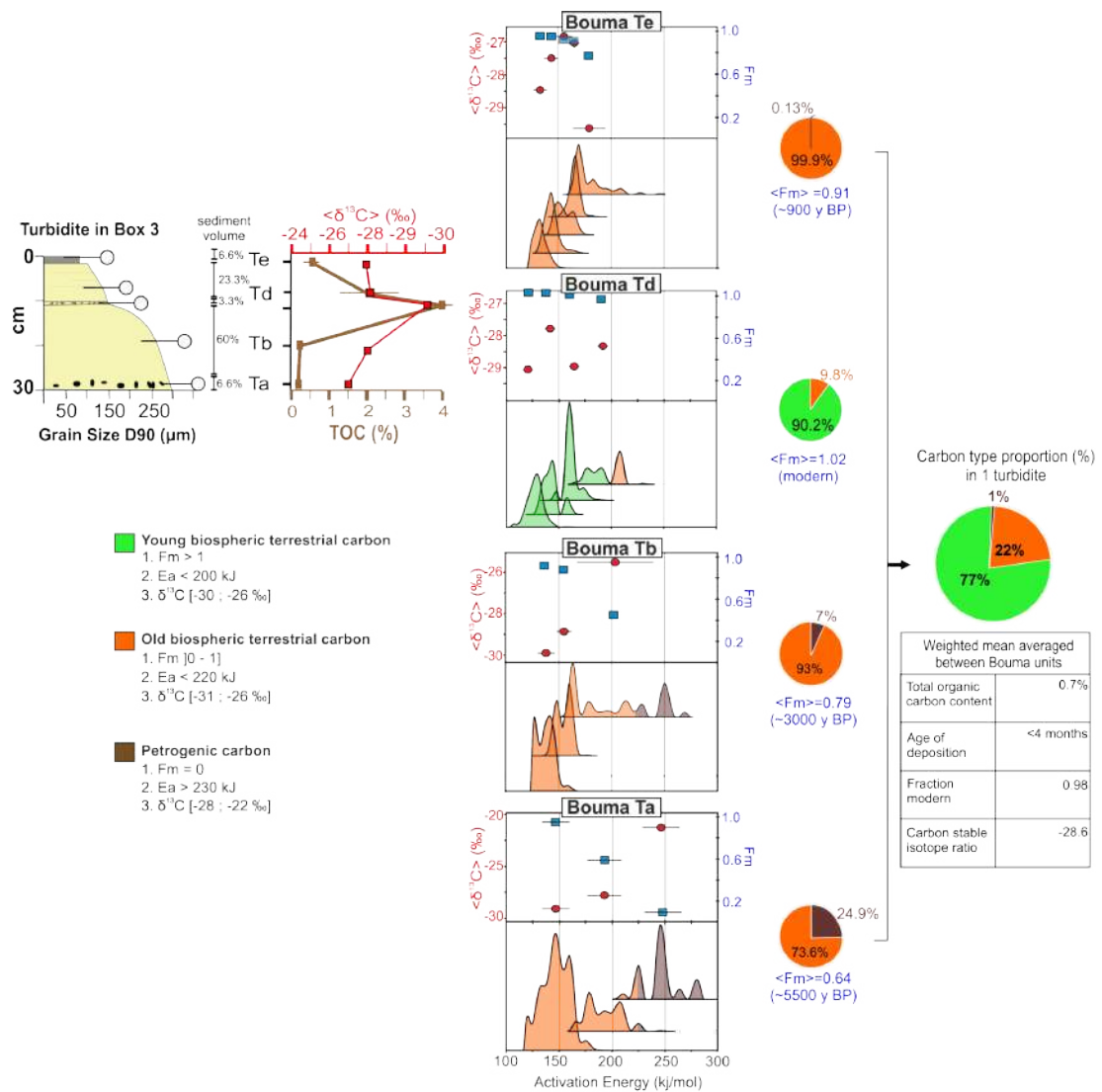


FIGURE 4.7: Identification of organic carbon types included in one turbidite. The following parameters were taken into account: Turbidite unit volumes, total organic carbon content per unit, thermograms performed on each unit by ramped oxidation and radiocarbon and carbon stable isotopes ratios measured for each fraction. F_m = Fraction modern (age), E_a = Activation of energy in kilojoules per mol (kJ/mol), $\delta^{13}\text{C}$ = Carbon stable isotope ratio in ‰

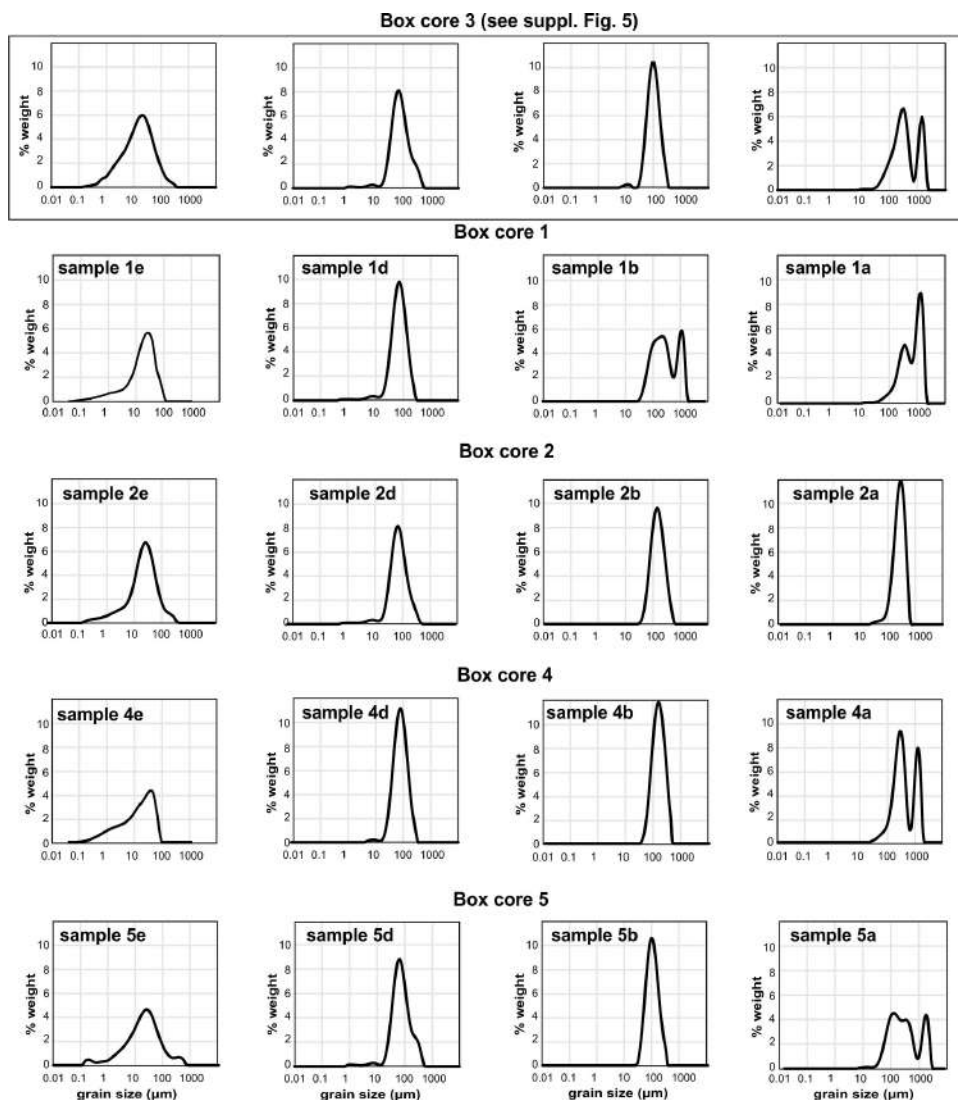


FIGURE 4.8: Grain size distributions measured on samples from the 5 box cores displayed in Fig. 4.1.

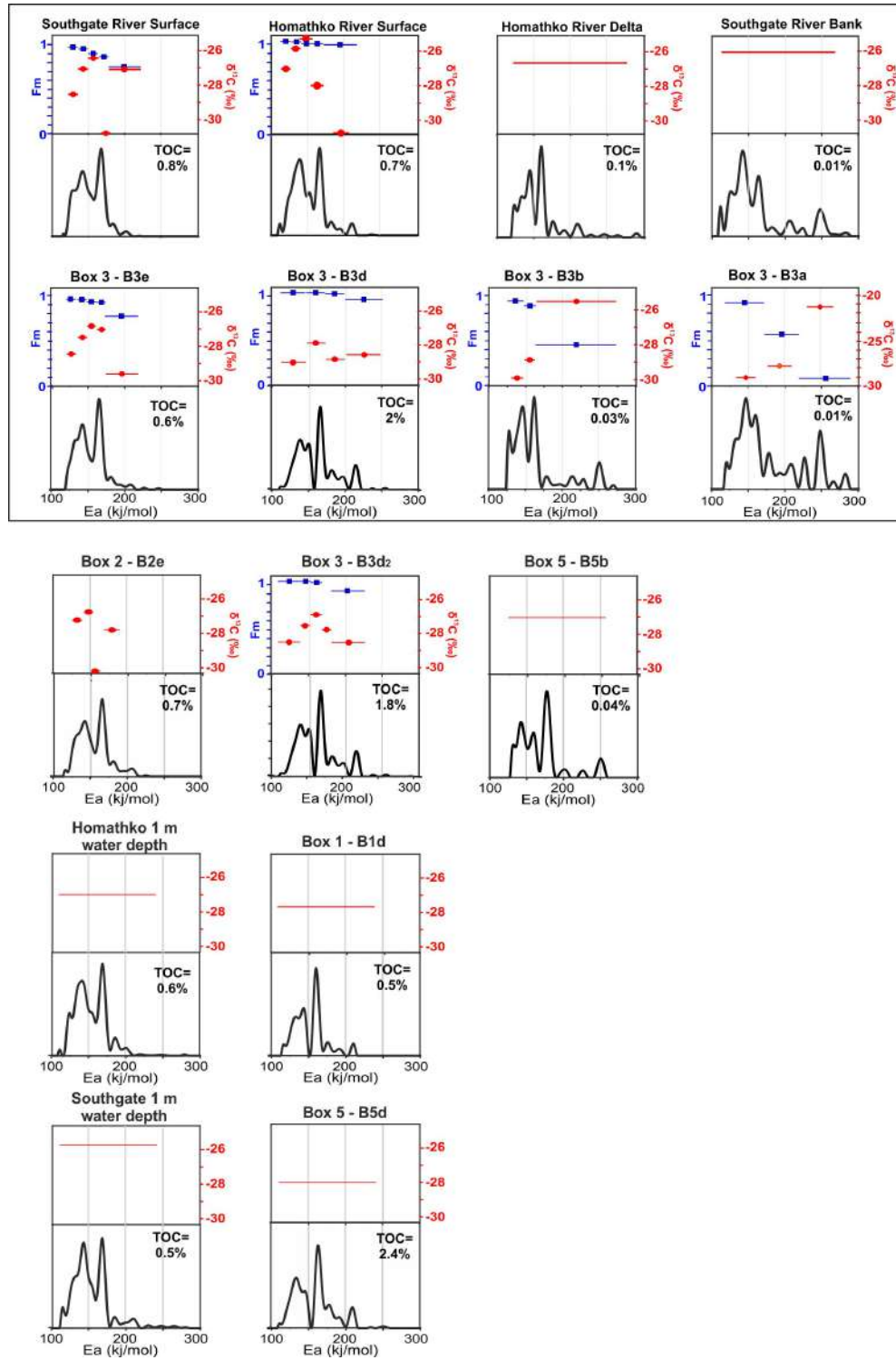


FIGURE 4.9: Additional thermograms and isotope data on turbidite and river samples displayed in Fig. 4.1

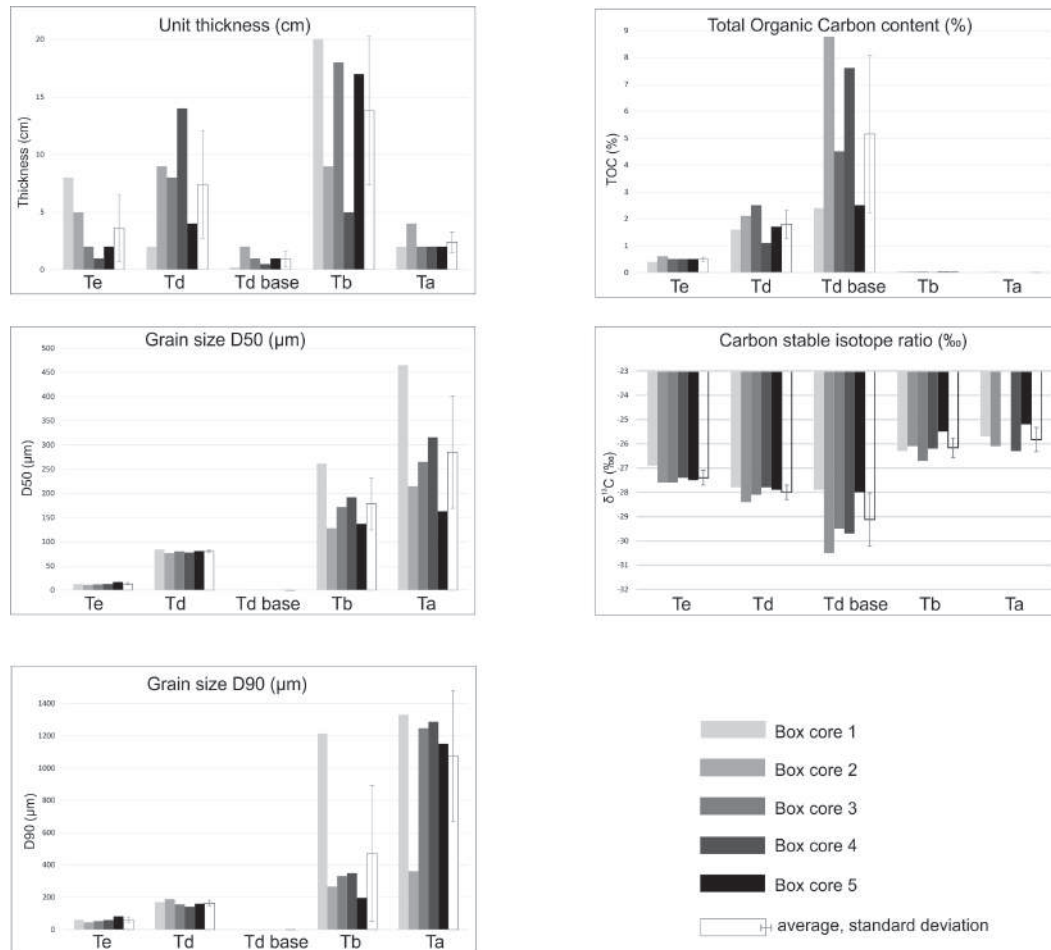


FIGURE 4.10: Measurements made on each Bouma unit of the turbidite samples from the 5 box cores displayed in Fig. 4.1. D50 and D90 = median and 90th percentile of the grain size distribution for each sample. TOC = Total organic carbon content; $\delta^{13}\text{C}$ = carbon stable isotope ratios.

Cruise code	Original sample ID	Julian Day - UTC Time	Latitude	Longitude	Core name in paper	Bouma unit in paper	TC (%)	TOC (%)	$\delta^{13}\text{C}$ (‰)	Grain Size D50 (μm)	Grain Size D90 (μm)
PGC2016007	STN010 (2cm)	284 - 20:13	50.864799	-124.867605	Box core 2	Td	0.61	0.58	-27.60	11.3	45.8
PGC2016007	STN010 (6cm)	284 - 20:13	50.864799	-124.867605	Box core 2	Td	2.15	2.1	-28.40	77.4	189.05
PGC2016007	STN010 (15cm)	284 - 20:13	50.864799	-124.867605	Box core 2	Td	1.42	1.44	-27.00		
PGC2016007	STN010 (wood)	284 - 20:13	50.864799	-124.867605	Box core 2	Td	7.6	7.6	-30.50	n/a	n/a
PGC2016007	STN010 (20cm)	284 - 20:13	50.864799	-124.867605	Box core 2	Tb	0.03	0.026	-26.10	128	267
PGC2016007	STN010 (26cm)	284 - 20:13	50.864799	-124.867605	Box core 2	Tb	0.02	0.02			
PGC2016007	STN010 (28cm)	284 - 20:13	50.864799	-124.867605	Box core 2	Ta	0.02	0.02	-25.50	215	362
PGC2016007	STN019 (1cm)	287 - 14:54	50.762583	-124.914604	Box core 3	Te	0.5	0.51	-27.60	11.7	51.9
PGC2016007	STN019 (4cm)	287 - 14:54	50.762583	-124.914604	Box core 3	Td	0.52	0.43	-27.70	59.3	171.3
PGC2016007	STN019 (10cm)	287 - 14:54	50.762583	-124.914604	Box core 3	Td	2.5	2.52	-27.80	80	157
PGC2016007	STN019 (wood)	287 - 14:54	50.762583	-124.914604	Box core 3	Td	4.97	4.97	-28.80	n/a	n/a
PGC2016007	STN019 (13cm)	287 - 14:54	50.762583	-124.914604	Box core 3	Tb	0.02	0.027	-26.70	172.4	332.3
PGC2016007	STN019 (20cm)	287 - 14:54	50.762583	-124.914604	Box core 3	Tb	0.06	0.1			
PGC2016007	STN019 (28cm)	287 - 14:54	50.762583	-124.914604	Box core 3	Ta	0.02	0.02	-25.40	265.2	1247.5
PGC2016007	STN025 (1cm)	287 - 23:02	50.704372	-124.867859	Box core 4	Te	0.5	0.52	-27.40	13	59
PGC2016007	STN025 (6cm)	287 - 23:02	50.704372	-124.867859	Box core 4	Td	1.21	1.1	-27.80	70.4	144.8
PGC2016007	STN025 (10cm)	287 - 23:02	50.704372	-124.867859	Box core 4	Tb	0.03	0.02	-26.30	78.5	141.7
PGC2016007	STN025 (15cm)	287 - 23:02	50.704372	-124.867859	Box core 4	Tb	0.02	0.02	-26.20	108.6	208.8
PGC2016007	STN025 (18cm)	287 - 23:02	50.704372	-124.867859	Box core 4	Ta	0.02	0.02	-26.00	192.7	350
PGC2016007	STN025 (22cm)	287 - 23:02	50.704372	-124.867859	Box core 4	Ta	0.015	0.01	-26.70	316	1288.6
PGC2016007	STN028 (1cm)	288 - 14:27	50.904482	-124.833942	Box core 1	Te	0.41	0.4	-26.90	13	60
PGC2016007	STN028 (6cm)	288 - 14:27	50.904482	-124.833942	Box core 1	Td	1.34	1.6	-27.70	84.3	169
PGC2016007	STN028 (wood)	288 - 14:27	50.904482	-124.833942	Box core 1	Td	2.88	2.88	-28.90		
PGC2016007	STN028 (9cm)	288 - 14:27	50.904482	-124.833942	Box core 1	Tb	0.06	0.05	-26.30	262.2	1214
PGC2016007	STN028 (12cm)	288 - 14:27	50.904482	-124.833942	Box core 1	Tb	0.03		-25.70	624.4	1347.5
PGC2016007	STN028 (18cm)	288 - 14:27	50.904482	-124.833942	Box core 1	Tb	0.04		-25.70	465.8	1332.8
PGC2016007	STN028 (32cm)	288 - 14:27	50.904482	-124.833942	Box core 1	Ta	0.02		-26.30	413.3	1328.5

TABLE 4.3: Data table showing cruise code, location, time, sample code and measurements made on samples collected from box cores in Bute Inlet (part 2)

Cruise code	Original sample ID	Julian Day - UTC Time	Latitude	Longitude	Core name in paper	Bouma unit in paper	TC (%)	TOC (%)	$\delta^{13}\text{C}$ (‰)	Grain Size D50 (µm)	Grain Size D90 (µm)
PGC2016007	STN036 (1cm)	288 - 22:29	50.632996	-124.881341	Box core 5	Te	0.56	0.57	-27.60	23.4	103.5
PGC2016007	STN036 (2cm)	288 - 22:29	50.632996	-124.881341	Box core 5	Te	0.42	0.42	-26.70	44.8	173.8
PGC2016007	STN036 (3cm)	288 - 22:29	50.632996	-124.881341	Box core 5	Td	1.52	1.53	-27.40	17.0	82.5
PGC2016007	STN036 (4cm)	288 - 22:29	50.632996	-124.881341	Box core 5	Td	2.4	2.44	-27.90	61.4	179.4
PGC2016007	STN036 (wood)	288 - 22:29	50.632996	-124.881341	Box core 5	Td	8.75	8.75	-29.80	n/a	n/a
PGC2016007	STN036 (6cm)	288 - 22:29	50.632996	-124.881341	Box core 5	Tb	0.05	0.04	-26.50	81.5	160.3
PGC2016007	STN036 (10cm)	288 - 22:29	50.632996	-124.881341	Box core 5	Tb	0.03		-25.20	145.2	297.8
PGC2016007	STN036 (15cm)	288 - 22:29	50.632996	-124.881341	Box core 5	Tb	0.08		-26.90	137.2	296.3
PGC2016007	STN036 (20cm)	288 - 22:29	50.632996	-124.881341	Box core 5	Tb	0.08		-27.00	115.6	278.9
PGC2016007	STN036 (24cm)	288 - 22:29	50.632996	-124.881341	Box core 5	Ta	0.03		-25.50	163.6	1150.9

TABLE 4.4: Data table showing cruise code, location, time, sample code and measurements made on samples collected from box cores in Bute Inlet
(part 2)

Cruise code	Original sample ID	Julian Day - UTC Time	Latitude	Longitude	Environment type	TC (%)	TOC (%)	$\delta^{13}\text{C}$ (‰)	Grain Size D50 (μm)	Grain Size D90 (μm)
PGC2017005	STN06 - RD	298 - 22:10	50.917464	-124.850457	Homathko delta	0.18	0.20	-26.71	75	230
PGC2017005	STN08 - RD	298 - 22:22	50.91905	-124.847667	Homathko delta	0.09	0.10	-27.21	347	770
PGC2017005	STN012 - RD	299 - 01:01	50.890661	-124.804308	Southgate delta	0.41	0.42	-26.23	37.2	159
PGC2017005	STN014 - RD	299 - 01:29	50.894877	-124.799608	Southgate delta	0.57	0.60	-26.74	183	493
PGC2017005	STN016 - RB	299 - 01:41	50.94125	-124.8573	Homathko bank	0.09	0.10	-27.04	104	207
PGC2017005	STN017 - RB	299 - 01:42	50.943767	-124.857583	Homathko bank	0.97	1.00	-28.21	37	193
PGC2017005	STN018 - RB	299 - 01:43	50.9482	-124.860933	Homathko bank	0.17	0.16	-26.78	77.8	185
PGC2017005	STN018 - RW	299 - 01:43	50.9482	-124.860933	Homathko water	0.48	0.47	-25.05	45.3	155
PGC2017005	STN020a - RW	299 - 01:45	50.934267	-124.8629	Homathko water	0.63	0.63	-26.5	31	150
PGC2017005	STN022 - RB	299 - 01:47	50.940917	-124.857267	Homathko bank	0.25	0.26	-27.19	65.3	172
PGC2017005	STN023a - RW	299 - 01:48	50.88605	-124.796817	Southgate water	1.03	1.01	-25.241		
PGC2017005	STN023b - RW	299 - 01:48	50.88605	-124.796817	Southgate water	0.85	0.80	-25.828	13.3	55.8
PGC2017005	STN023c - RW	299 - 01:48	50.88605	-124.796817	Southgate water	0.91	0.91	-25.559		
PGC2017005	STN023d - RW	299 - 01:48	50.88605	-124.796817	Southgate water	0.43	0.42	-25.9061	38.6	209
PGC2017005	STN024 - RB	299 - 01:49	50.887633	-124.796817	Southgate bank	0.02	0.01	-26.47	173	331

TABLE 4.5: Data table showing cruise code, location, time, sample code and measurements made on samples collected from rivers connected to Bute Inlet

Chapter 5

Conclusions and research perspectives

The overarching objective of this thesis is to bridge the gap between turbidity current processes and products using observations of the seafloor and of flows in action. To fulfil this objective, I used direct measurements of turbidity currents, repeated bathymetric surveys and samples of the deposits in two fjords in British Columbia: Howe Sound and Bute Inlet. Three research questions have been addressed:

- *Chapter 2: How do extremely dilute river plumes generate turbidity currents?*
- *Chapter 3: What are the diagnostic deposits of crescentic bedforms formed by super-critical turbidity currents?*
- *Chapter 4: How is young terrestrial organic carbon preserved in turbidites?*

Sections 5.1., 5.2 and 5.3 aim to answer these questions, discuss future research possibilities, and propose sites where the applicability of the fjord-related findings presented here can be tested in the deep-sea.

5.1 How do extremely dilute river plumes generate turbidity currents?

It was generally thought that rivers needed to exceed a specific suspended sediment concentration threshold (e.g. 40 g/L, 1 g/L; Mulder and Syvitski, 1995; Parsons et al., 2001) to be capable of directly generating turbidity currents at their mouth. Chapter 2 demonstrates that rivers with sediment concentrations well below this threshold (0.07g/L) can also generate turbidity currents under certain conditions. These conditions are low water spring tide, relatively high river discharge, a turbidity maximum

being forced out on a steep delta front and the availability of loose-packed fine sediment on the seabed. These findings are important because they suggest that a much wider range of the world's rivers can directly generate turbidity currents than previously thought. Predicting how and when rivers generate turbidity currents enables us to constrain how and where terrestrial particles are transported into the sea. This transport is particularly relevant given the current levels of ocean pollution (e.g. Pham et al., 2014; Pierdomenico et al., 2019; Kane and Clare, 2019).

5.1.1 Limitations and future research

Future research on turbidity current generation by dilute rivers should concentrate on at least two knowledge gaps. First, there is a need to characterise the loose-packed sediment layer overlying the seabed that chapter 2 suggests to be one of the conditions needed for a flow to be triggered. Characterization of this layer is challenging using acoustic Doppler current profilers (ADCPs) due to their tilted beams which cause interference with the surrounding seabed morphology close to the bed, thus preventing the near-bed layer from being imaged properly. An alternative to ADCPs would be to use acoustic instruments with a vertical and narrow beam. It would be useful to combine instruments with different frequencies in order to characterize the hypothesized loose-packed layer, as different frequencies respond differently to different substrate properties (Thorne et al., 1991; Hurther et al., 2011). Second, the observations used in chapter 2 were collected for five days which do not cover the full range of conditions that characterize the river/submarine system. Collection of river and turbidity current data for a longer timescale in Squamish would enable our findings to be tested in a statistically more robust manner.

5.1.2 Test site

The Congo submarine canyon appears to be a particularly relevant site to interrogate how dilute river plumes could generate turbidity currents that flow into the deep-sea. Turbidity currents in the Congo canyon have been observed to last for several days (Azpiroz-Zabala et al., 2017). It was shown that although these flows are linked to periods of elevated river discharge (Azpiroz-Zabala et al., 2017), their exact initiation process remains elusive. Similarly to Squamish, the Congo river estuary is characterised by very low suspended sediment concentrations ($<1\text{g/L}$) and by tides of up to 2 metres amplitude. However, in contrast to the steep sandy delta studied in Squamish, the Congo river estuary is mud-rich and characterized by a gentle slope ($<1^\circ$; Babonneau, 2002). It would thus be interesting to test the role of the Congo river plume and tides in generating turbidity currents despite the absence of a significant slope in the Congo canyon.

5.2 What are the diagnostic deposits of crescentic bed-forms formed by supercritical turbidity currents?

The question addressed in chapter 4 is timely because there was a discrepancy between the deposits produced in experimental models (regular back-stepping beds of sediment, e.g. Kostic, 2011; Cartigny et al., 2014) and the observations described in outcrops interpreted as supercritical flow deposits (irregular lens-shaped beds of massive sands, e.g. Bain and Hubbard, 2016; Dietrich et al., 2016). Chapter 3 resolves this discrepancy using a combination of: 1) flow monitoring, 2) repeated seafloor mapping, and 3) sediment cores in a modern system (Squamish submarine delta). Using these observations from a modern system, chapter 3 shows that supercritical flow deposits range between two end-members. One end member corresponds to low preservation by supercritical flows which results in lens-shaped scours filled with massive sands. The other end member correspond to high preservation by supercritical flows which results in regular back-stepping beds. Importantly, these results provide diagnostic criteria for recognizing supercritical flow deposits in the sedimentary record. Such deposits are important to understand as stacks of turbidite deposits record past fluxes of sediment, organic carbon and nutrients into the ocean, and additionally these deposits host a significant share of the global oil and gas resources. Chapter 3 ends with a comparison between the presented results and a large number of deposits described elsewhere, which suggest that supercritical flows have been abundant throughout geological time.

5.2.1 Limitations and future research

Future work on recognition of supercritical flow deposits could focus on the micro-scale facies that characterizes the massive sands. Although the sands described in chapter 3 appear massive and structureless on a visual basis, micro-structures (e.g. flames, fainted laminae as suggested by Postma et al., 2014) might be revealed based on a more detailed imagery. This could be achieved on the sediment cores acquired in Squamish using techniques such as traditional X-rays, magnetic resonance imagery, or impregnation by lacquer peel which can highlight micro-scale sediment structures (Douillet et al., 2018). Identifying such structures could help further recognition of supercritical flow deposits, especially in settings where sediment cores are the only source of information available. Second, the three dimensional architecture of supercritical flow deposits has not been fully constrained in chapter 3, as this chapter focused on a single stratigraphic profile oriented along the channel. It would be useful to provide diagnostic criteria in strike and oblique oriented profiles in the Squamish submarine channels to help recognition of supercritical flow deposits in outcrops irrespective of the orientation of the outcrop.

5.2.2 Test site

I suggest that crescentic bedforms observed in the Monterey canyon could serve as a deep-sea test site for the here presented fjord results. Sediment cores collected in Monterey canyon indeed show striking similarities with our deposits (Paull et al., 2011). It would be interesting to combine these sediment cores from Monterey with a reconstruction of the architecture based on repeated bathymetrical surveys in order to test whether our results in Squamish match these deep-sea geometries.

5.3 How is young terrestrial organic carbon preserved in turbidites?

To answer this question, I combined 1) direct observations of turbidity currents, 2) sampling of their deposits (including samples into the river sources) and 3) detailed analysis of the organic carbon composition and age found in those deposits using a novel ramped oxidation method (Hemingway et al., 2017). Based on this combination of data, chapter 4 demonstrates that 77 % of the organic carbon buried by turbidity currents on the seabed of Bute Inlet is made of young organic carbon consisting of woody debris buried within the fine sands. This contrasts with the current paradigm that most organic carbon buried in marine sediments is associated with muddy sediments. Chapter 4 thus suggests that global carbon fluxes could have been globally underestimated both in fjords and oceans. Constraining these coarser grained fluxes is important as burial of young terrestrial organic carbon removes CO₂ from the atmosphere and thus controls the climate over geological timescales.

5.3.1 Limitations and future research

Future investigation on organic carbon in Bute Inlet can focus on at least three objectives. First, the sedimentary sources could be better constrained. The river samples used in chapter 4 were collected in October 2017. It would be useful to sample these rivers again at a different time in the year in order to cover a wider range of river discharge conditions which can impact the organic matter composition. Second, another unresolved issue is the ratio of organic carbon burial by turbidity currents versus the organic carbon during background sedimentation outside the turbidity current channel. This would require detailed characterization of the organic carbon composition found in the different geomorphological areas of the fjord seabed, i.e. terraces, levees, distal lobe, flanks. Sedimentation rates would need to be determined in these different areas. Third, the efficiency of longer-term preservation of organic carbon is still unconstrained. The sediment cores presented in chapter 4 cover maximum four months of stratigraphic preservation, based on the repeated bathymetrical surveys carried out in summer 2016.

Several longer piston cores (up to 8 m long) have also been collected in the distal areas of the fjord (Fig. A2 in Appendix) and could help address the longer-term burial question.

5.3.2 Test sites

Burial of large woody debris over the last 19 million years has recently been described in turbidite sands 2000 km offshore from the Ganges River (Lee et al., 2019). This woody debris has probably been emplaced by similar hydrodynamic sorting processes as described in chapter 4. It would be interesting to test whether turbidity currents are still currently active in the Bengal fan, as the Bengal Fan contains 10-20 % of the total terrestrial organic carbon buried in marine sediments worldwide (Galy et al., 2007).

Furthermore, the longer-term implications of the findings demonstrated in chapter 4 could also be tested in geological outcrops. For instance woody debris was described in Eocene to Oligocene turbidites in the Gres d'Annot system, SE France (McArthur et al., 2016) and in the Marnoso-Arenacea Formation, northern Italy (McArthur et al., 2017). These studies have focussed on burial of woody debris from a hydrocarbon point of view, but it would be interesting to also investigate the implications of these woody debris buried in rocks for the global carbon cycle over geological timescales.

5.4 Broader research perspectives on turbidity current processes and products

There are still several exciting open research questions on the link between turbidity current processes and products in general. I will here conclude with four perspectives that naturally follow up on the science presented in this thesis.

First, despite the recent advent in technologies used to study the seabed, there are still parts of the turbidity currents that require further technological development to enable accurate measurements. This is particularly true for the near-bed layer of turbidity currents (as mentioned in section 5.1). The character of this near-bed layer is key to constrain not only for understanding the initiation of turbidity currents (chapter 2) but also for constraining the role of such layer in the formation of crescentic bedforms (Hughes Clarke, 2016, chapter 3).

Second, this thesis uses two of the very few marine sites from which direct observations of turbidity currents and their deposits are available. The data form a welcome addition to the classic data available from the depositional record. However, there is a strong case to now extend these seafloor observations over a much wider range of sites and over longer time scales. In the case of Howe Sound and Bute Inlet, the results from the

modern day seafloor observations could be extended further back in time by collecting longer sedimentary sequences through vibracoring or drilling.

Third, I suggested that the findings demonstrated in all three chapters in fjords may also well apply in some deep-sea settings. There is thus an obvious line of investigations to be conducted in the deep-sea in order to test whether the three scientific findings demonstrated in this thesis indeed apply to such deeper water settings.

Finally, a natural continuation of this thesis would be to capture the full pathway of a turbidity current triggered from a river, its interaction with the seabed and its deposits in a single data set. This would require systematic sampling of the river, sampling in the flow itself, as well as repeated seafloor mapping and direct coring into the seabed just after occurrence of the flow. Collection of such a data set would enable us to constrain sediment and organic carbon fluxes from source to sink in real time. Constraining such fluxes would help to assess how past fluxes of particles and organic carbon would have evolved throughout geological times.

Appendix A

Appendix

The following three appendices aim to provide further detail on:

- 1) the field campaigns that have enabled acquisition of the data presented in this thesis (Appendix A1),
- 2) the general processing for the data acquired by acoustic Doppler current profilers shown in all three science chapters (Appendix A2),
- 3) the inversion method used to invert ADCP backscatter into suspended sediment concentration presented in chapter 2 (Appendix A3).

A.1 Field campaigns

A.1.1 Squamish 2015

This appendix presents the four field campaigns that have enabled acquisition of the data used in this thesis.

A six-day long monitoring program (funded by NERC grant NE/M007138/1) was carried out by the Sedimentology Research Group of the National Oceanography Centre Southampton in conjunction with the Ocean Mapping Group from the University of New Brunswick. This field campaign aimed to characterise turbidity current properties (e.g. dimensions, velocities, sediment concentration), their initiation mechanisms and the interaction with the seafloor. Data collection was focused on the central channel downstream of Squamish Delta. One turbidity current was monitored during the study period (investigated in chapters 2 and 3). Two research vessels were involved (Figure A.1).

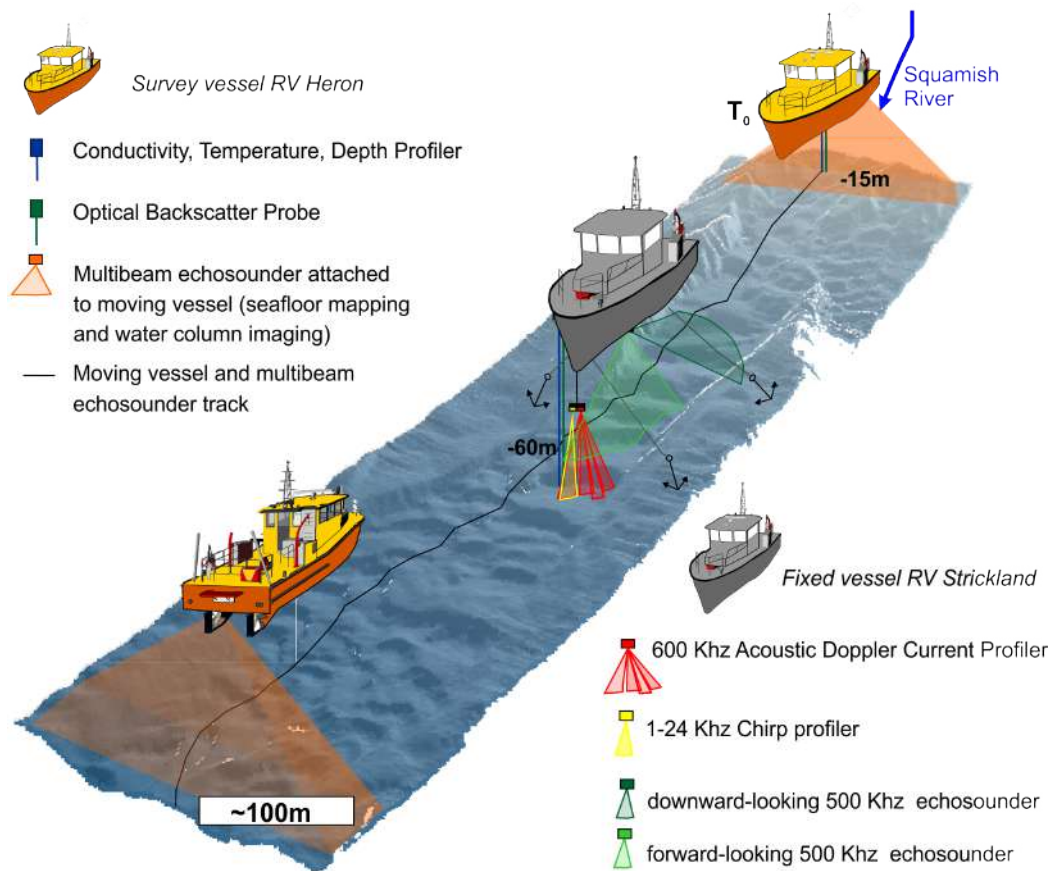


FIGURE A.1: Overview of the field experiment (vessels and instruments deployment) carried out in Squamish in June 2015

A.1.1.1 Moving vessel Heron

The first vessel repeatedly mapped (i.e. every 12 min) the central channel using a EM 70-100 kHz multibeam system (50 cm of horizontal resolution and 20 cm of vertical resolution). This repeated mapping was aimed at detecting any migration of the bedforms due to turbidity currents initiated from the Squamish Delta. From the same boat was also deployed a 500 KHz M3 sonar aimed at imaging the water column. Finally, Conductivity Temperature and Depth (CTD) as well as Optical Backscatter (OBS) profilers were deployed systematically at 15, 30 and 60 meters of water depth in order to characterise the water column composition. The OBS probe was calibrated using suspended sediment samples in order to derive the suspended sediment concentration in the water column.

A.1.1.2 Stationary Vessel RV Strickland

The second vessel was moored using four anchors, 100 m downstream of the delta lip at 60 m of water depth. We deployed four acoustic instruments 30 m below the anchored

vessel to detect turbidity currents. First, a 600 kHz Acoustic Doppler Current Profiler measured internal velocities of turbidity currents (3.5 sec of time interval and 50 cm of vertical resolution). The backscatter returned by the four beams of this instrument provides a proxy for the volume and grain size of sediments suspended in both the stationary water column and in the turbidity currents (see Appendix A3). Second, a Chirp sub-bottom profiler operating at low frequencies (1-12 KHz) was aimed at imaging through turbidity currents in order to characterise the near-bed layer. Third, two 500 KHz echosounders (one looking forward with a 45° angle and one looking downward) captured images of turbidity currents in plan view and cross sections (time interval = 1sec). These images were combined together as movies which show turbidity currents in three dimensions (see suppl. Material of chapter 3).

A.1.2 Squamish 2016 (Geological Survey of Canada cruise 2016003PGC)

We collected a set of piston and box cores in June 2016 in the same section of the central channel as the one investigated in June 2015. These sediment cores were acquired aboard the Canadian Coast Guard Research Vessel Vector by scientists from the Canadian Geological Survey and the Sedimentology Research Group of the National Oceanography Centre Southampton. We logged, scanned (e.g. magnetic susceptibility, density) and photographed these sediment cores (Figures A.2 to A.9) in the sediment lab of the Institute of Ocean Sciences in Sidney, Vancouver Island (Canada). I use this set of sediment cores in chapter 3 to characterise the sediment facies associated with upstream migrating bedforms and supercritical turbidity currents.

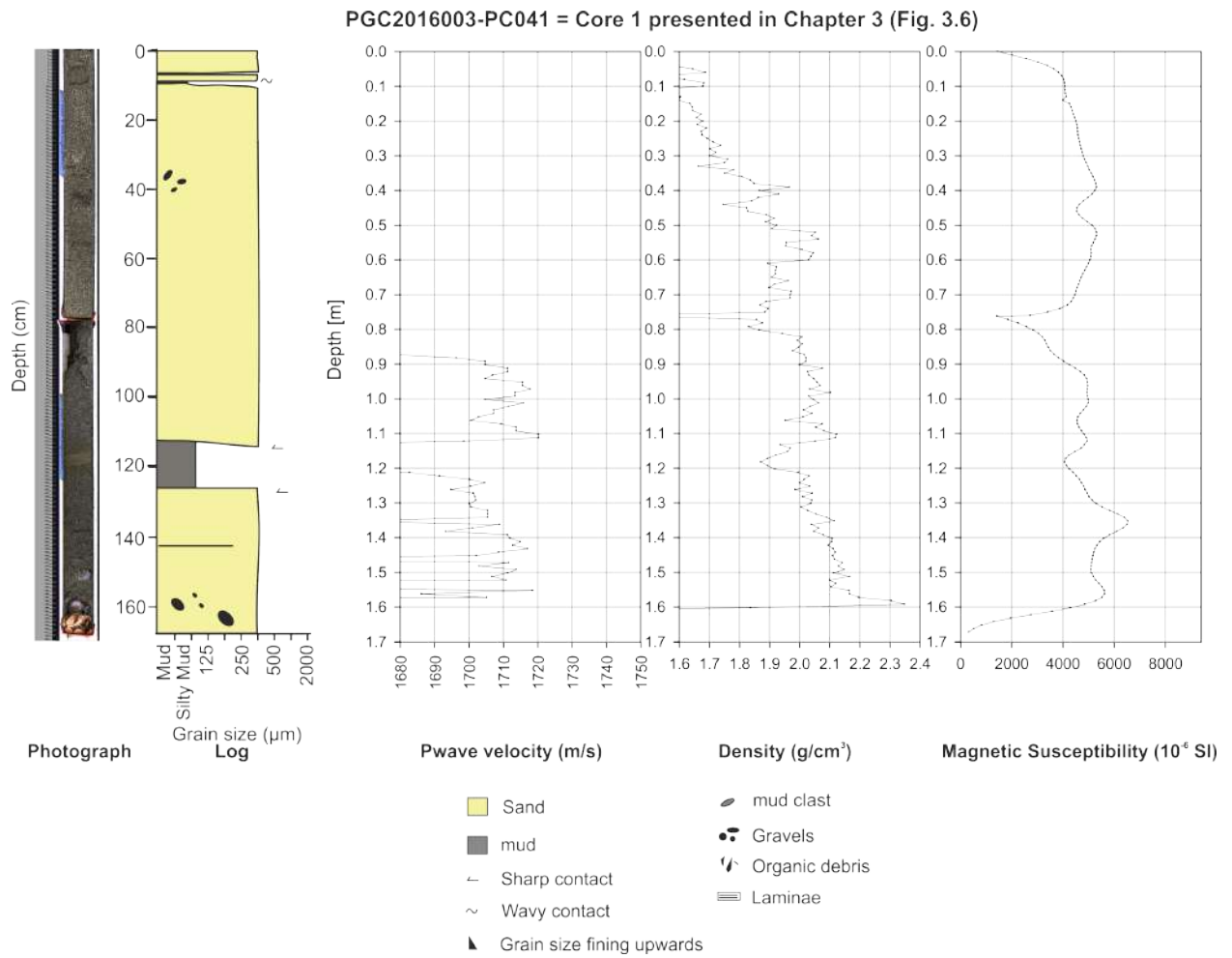


FIGURE A.2: Photograph, log and physical properties for piston core 1 collected in Squamish (Howe Sound) and presented in Chapter 3 (Fig. 3.6)

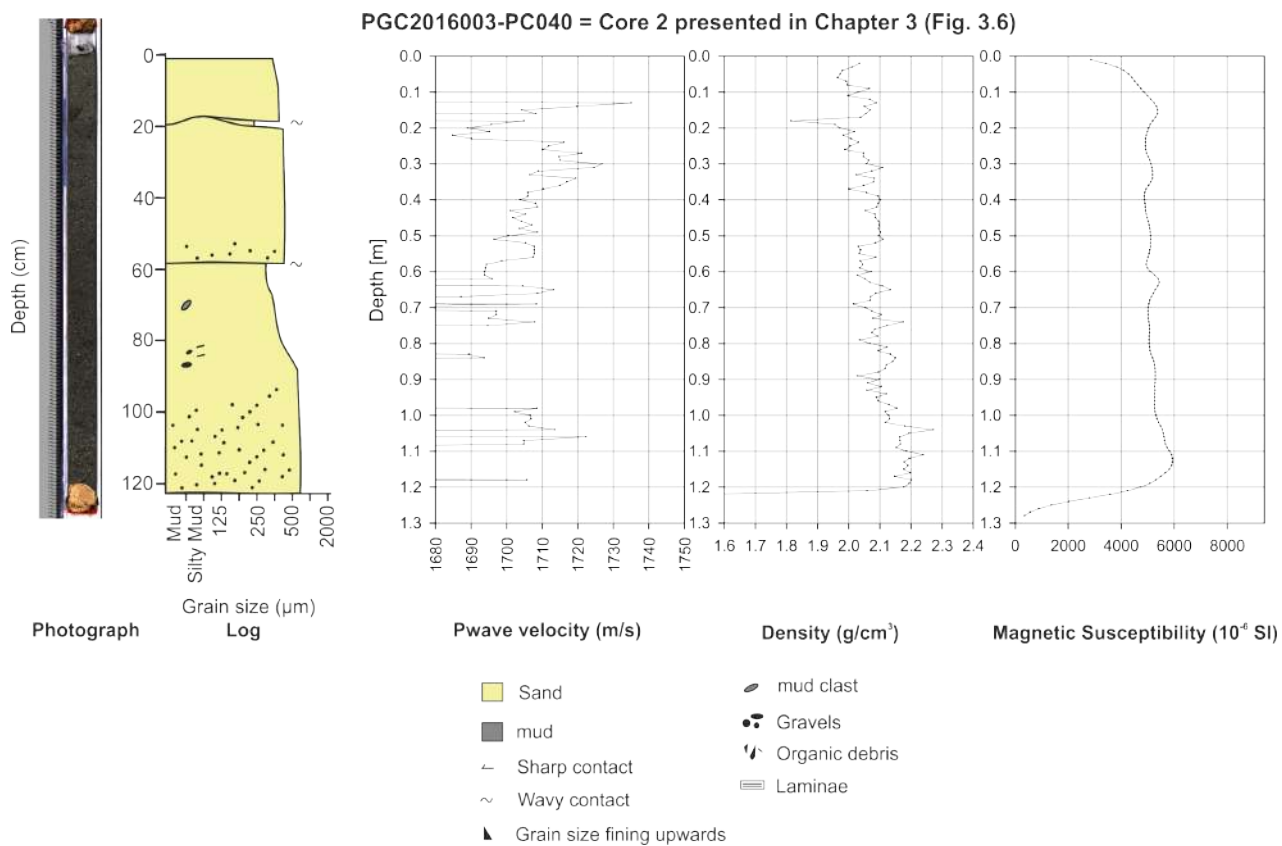


FIGURE A.3: Photograph, log and physical properties for piston core 2 collected in Squamish (Howe Sound) and presented in Chapter 3 (Fig. 3.6)

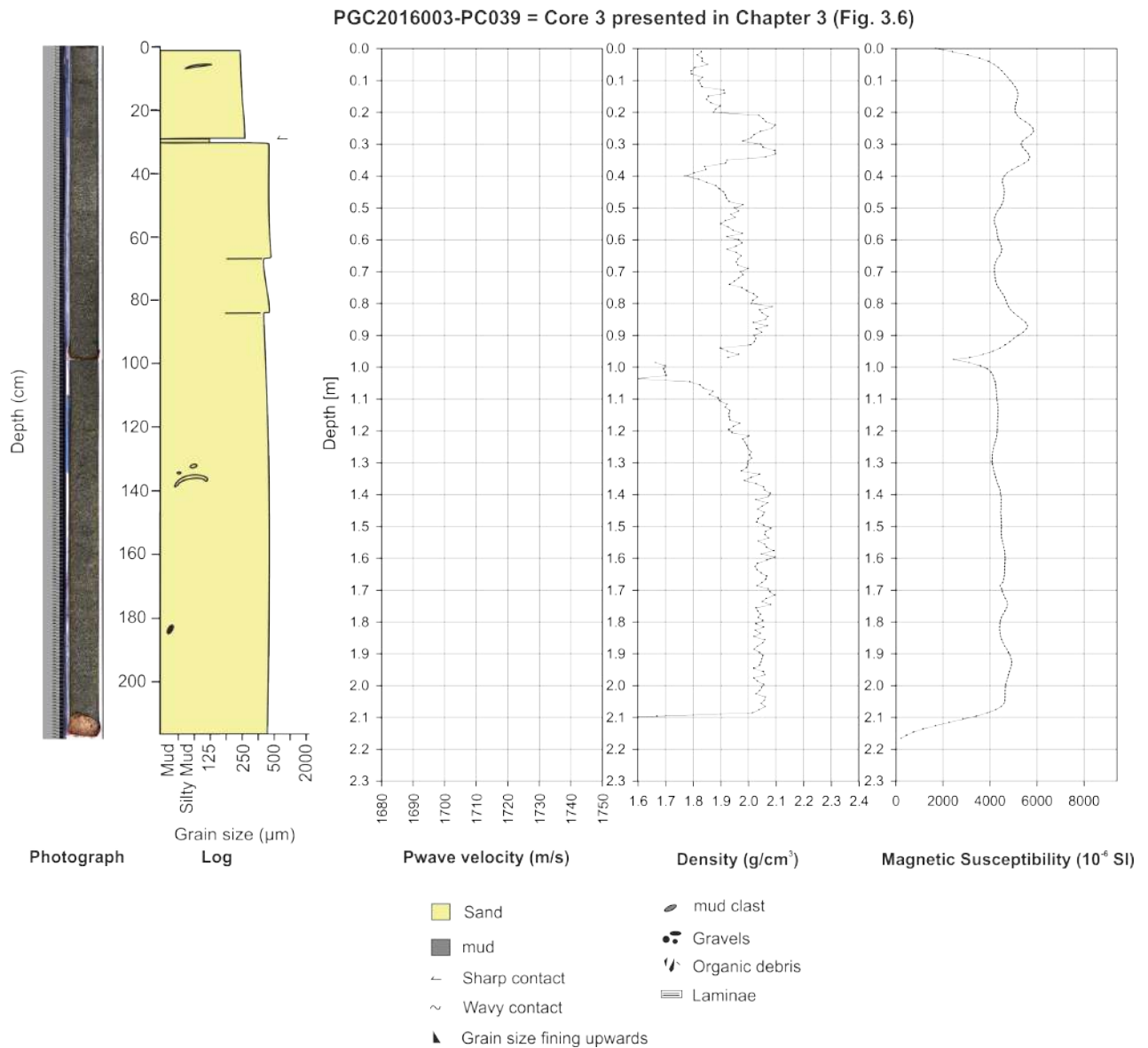


FIGURE A.4: Photograph, log and physical properties for piston core 3 collected in Squamish (Howe Sound) and presented in Chapter 3 (Fig. 3.6)

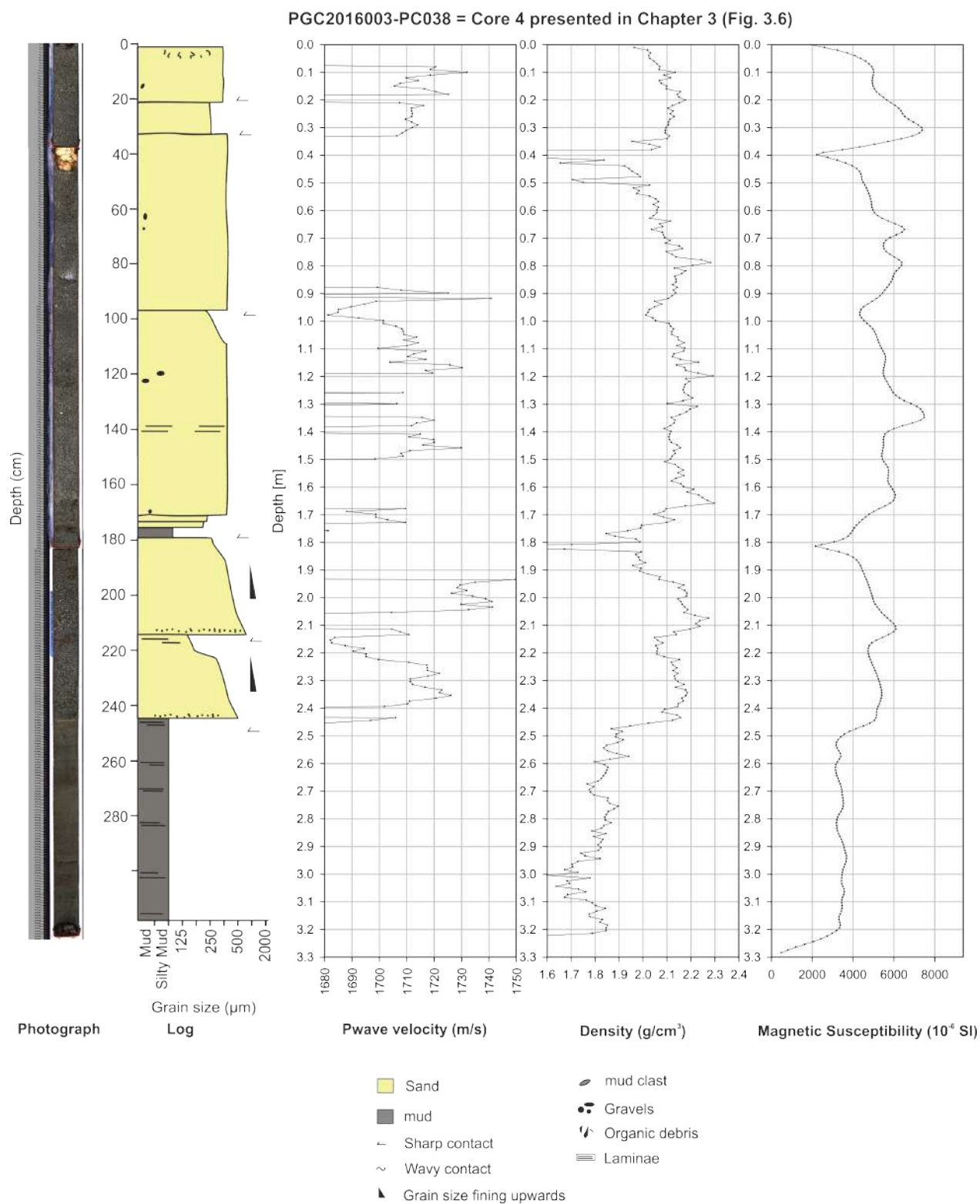


FIGURE A.5: Photograph, log and physical properties for piston core 4 collected in Squamish (Howe Sound) and presented in Chapter 3 (Fig. 3.6)

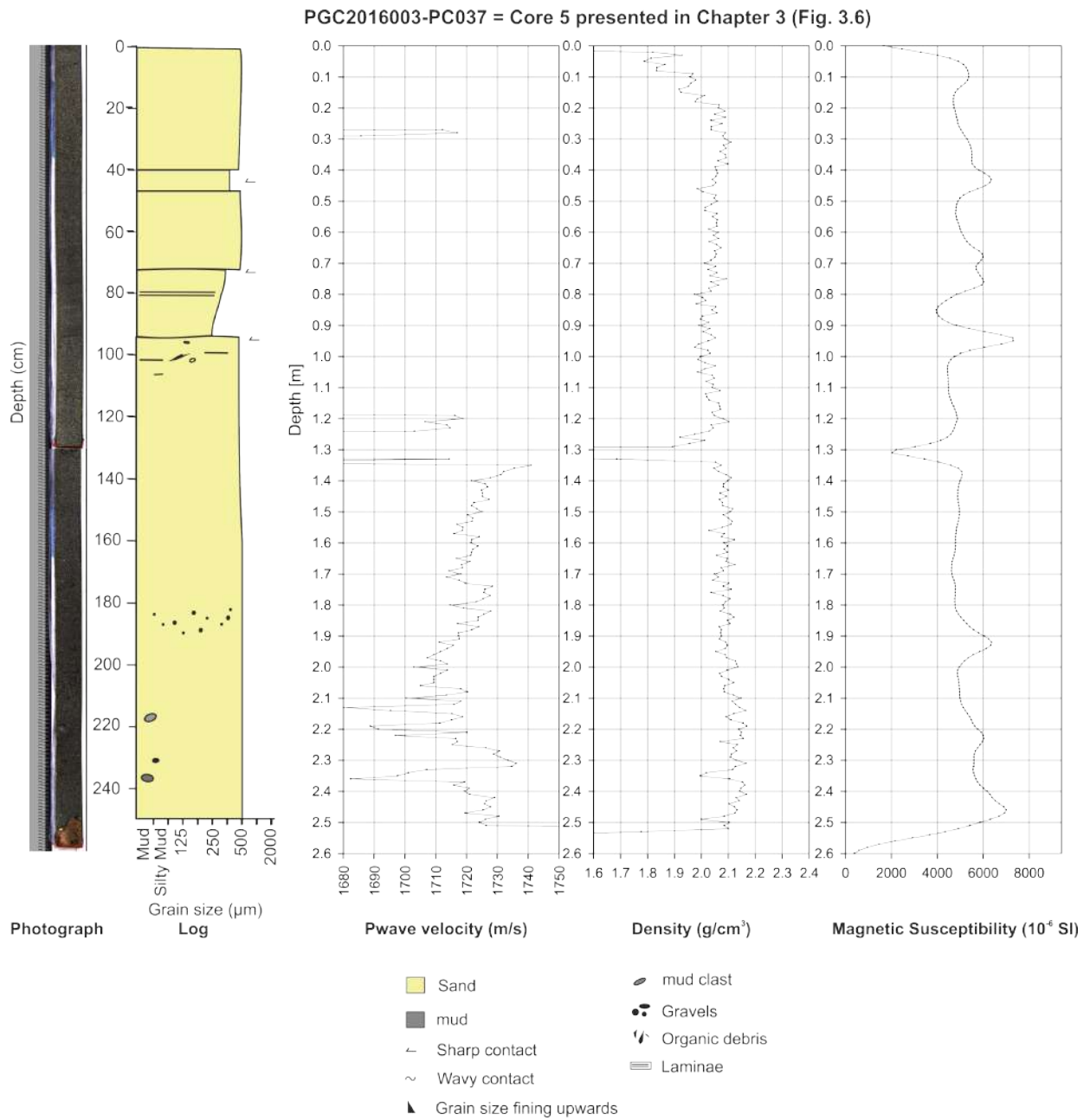


FIGURE A.6: Photograph, log and physical properties for piston core 5 collected in Squamish (Howe Sound) and presented in Chapter 3 (Fig. 3.6)

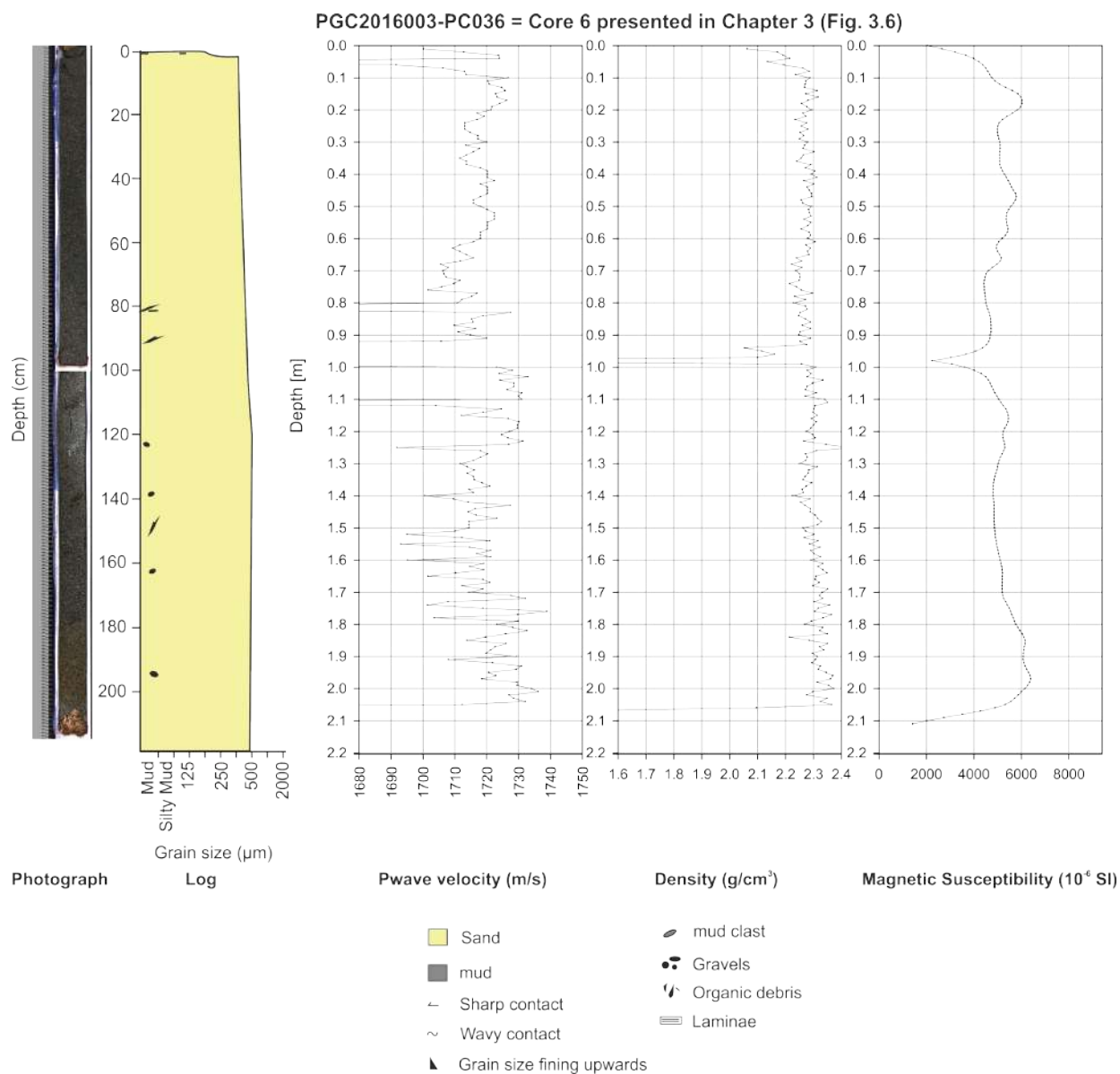


FIGURE A.7: Photograph, log and physical properties for piston core 6 collected in Squamish (Howe Sound) and presented in Chapter 3 (Fig. 3.6)

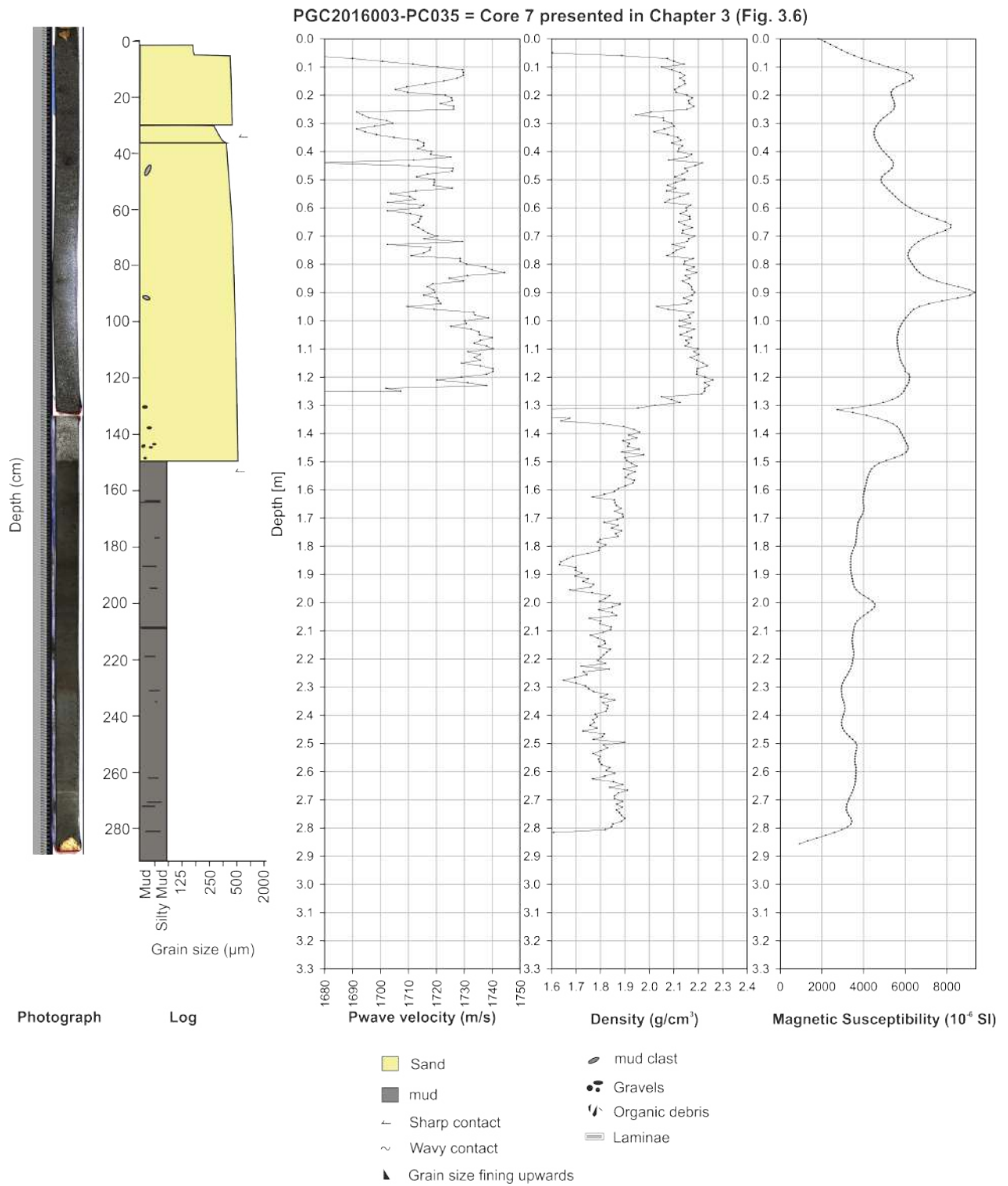


FIGURE A.8: Photograph, log and physical properties for piston core 7 collected in Squamish (Howe Sound) and presented in Chapter 3 (Fig. 3.6)

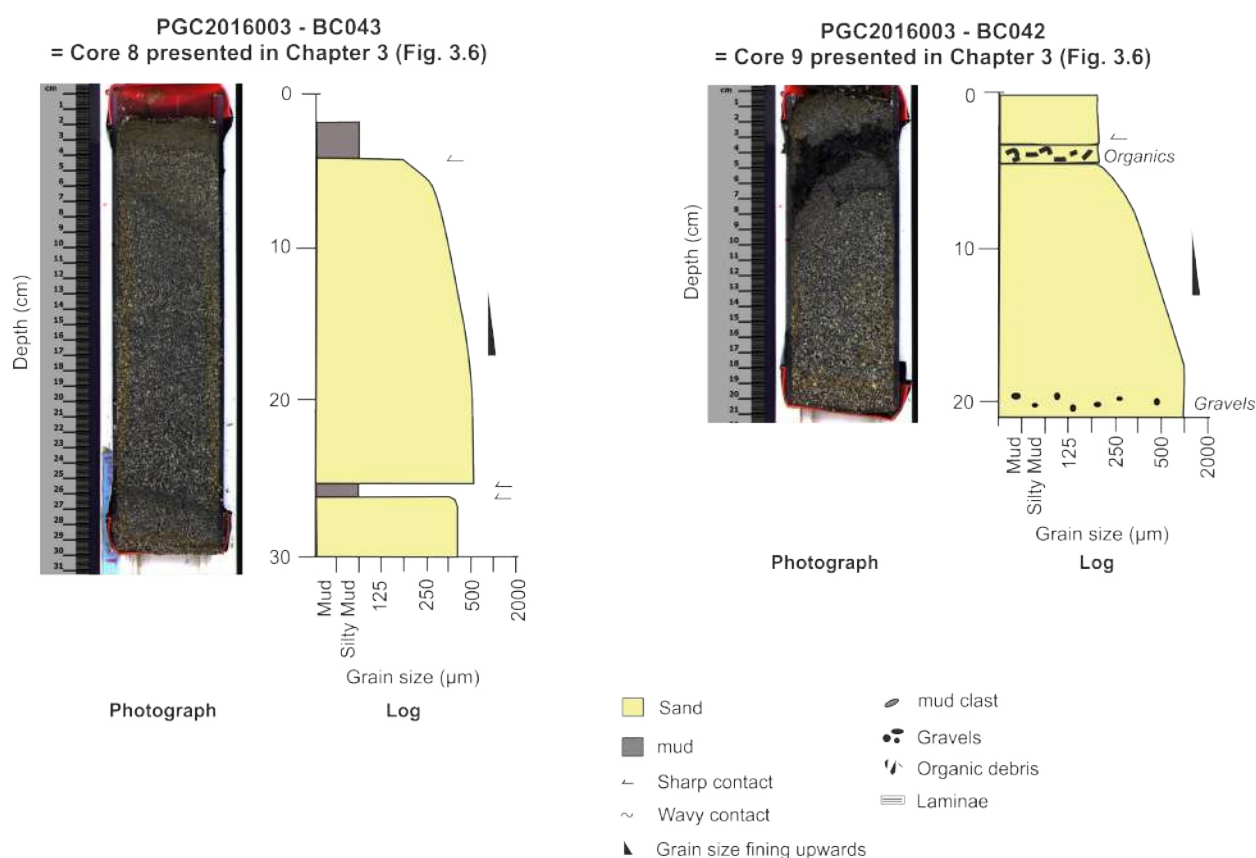


FIGURE A.9: Photographs and logs for box cores 8 and 9 collected in Squamish (Howe Sound) and presented in Chapter 3 (Fig. 3.6)

A.1.3 Bute Inlet 2016 (Geological Survey of Canada cruise 2016003PGC and 2016007PGC)

A four-month long monitoring program (funded by NERC grant NE/M017540/1) was carried out in 2016 by the Sedimentology Research Group of the National Oceanography Centre Southampton and the Canadian Geological Survey. This program involved two research cruises (in June and October 2016) which aimed to link turbidity currents, their impact on the seafloor and the associated deposits across the whole fjord. I use some of the flow observations and a set of sediment cores taken during the two research cruises as part of chapter 4 (Figure 4.1).

The first cruise occurred in June 2016 where two vessels were mobilised (Canadian Coast Guard Ship Vector and Research Vessel Strickland). This mobilisation had three aims. First, we suspended four 600 kHz and two 300 kHz Acoustic Doppler Current Profilers at six locations 20 metres above the submarine channel thalweg. These ADCPs were left in the fjord for 4 months in order to measure turbidity current activity during the freshet period. Second, we mapped the fjord seafloor using an EM710 70-100 kHz multibeam echosounder (2 meters of horizontal resolution, <5 % of water depth (m) of vertical

resolution). Third, we collected 25 sediment cores using a piston coring system, in order to characterise the sedimentary deposits from the head to the distal lobe of the fjord.

The second cruise occurred in October 2016 aboard the CCGS Vector and had three aims. First we recovered the six ADCPs deployed in June 2016. More than 15 turbidity currents were measured by the ADCPs (following the processing described in Appendix 2). Second, we mapped again the fjord seafloor in order to characterise the morphological evolution resulting from this turbidity current activity. Third, we sampled the sedimentary deposits left by the turbidity currents. 27 sediment cores were recovered from the ADCP locations and the adjacent levees using a box coring system as the piston coring failed at sampling those sandy deposits.

We logged, scanned and photographed all sediment cores (Figures A.10 to A.14) in the sediment lab of the Institute of Ocean Sciences in Sidney, Vancouver Island (Canada). All sediment core logs were digitized (Figure ??) and some of them were sampled. I performed several sets of measurements on some of these sediment samples. First, they were analysed for grain size using a Malvern Mastersizer 2000 at the National Oceanography Centre Southampton. Second, they were analysed for organic carbon (see methods in supplementary material of Chapter 4).

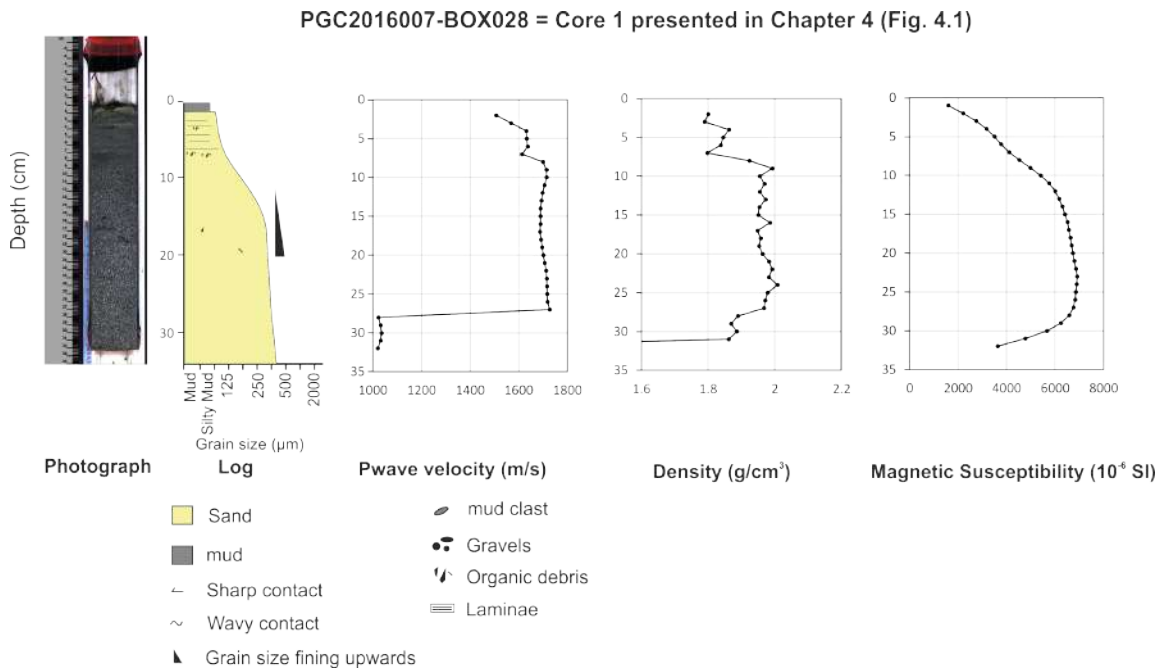


FIGURE A.10: Photograph, log and physical properties for box core 1 collected in Bute Inlet and presented in Chapter 4 (Fig. 4.1)

PGC2016007-BOX010 = Core 2 presented in Chapter 4 (Fig. 4.1)

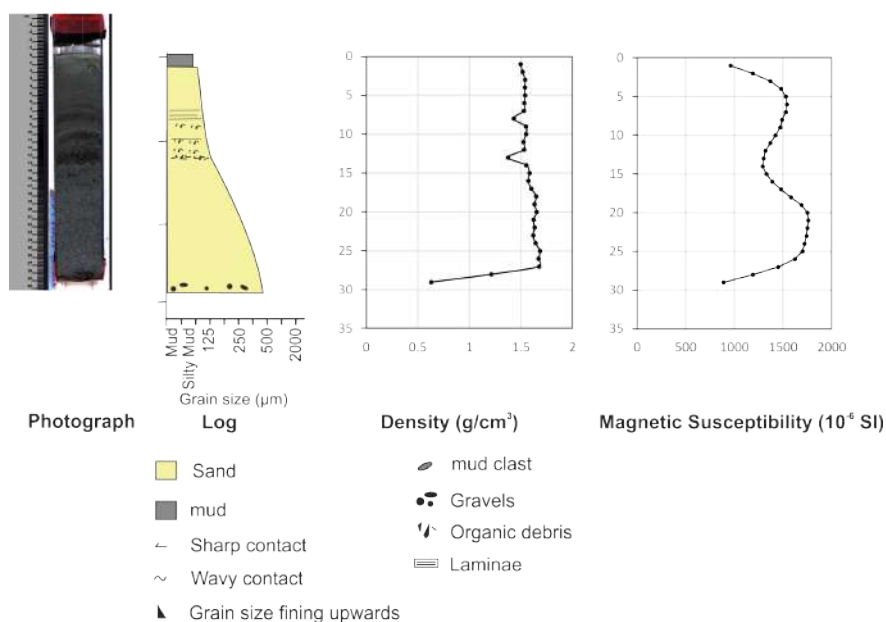


FIGURE A.11: Photograph, log and physical properties for box core 2 collected in Bute Inlet and presented in Chapter 4 (Fig. 4.1)

PGC2016007-BOX019 = Core 3 presented in Chapter 4 (Fig. 4.1)

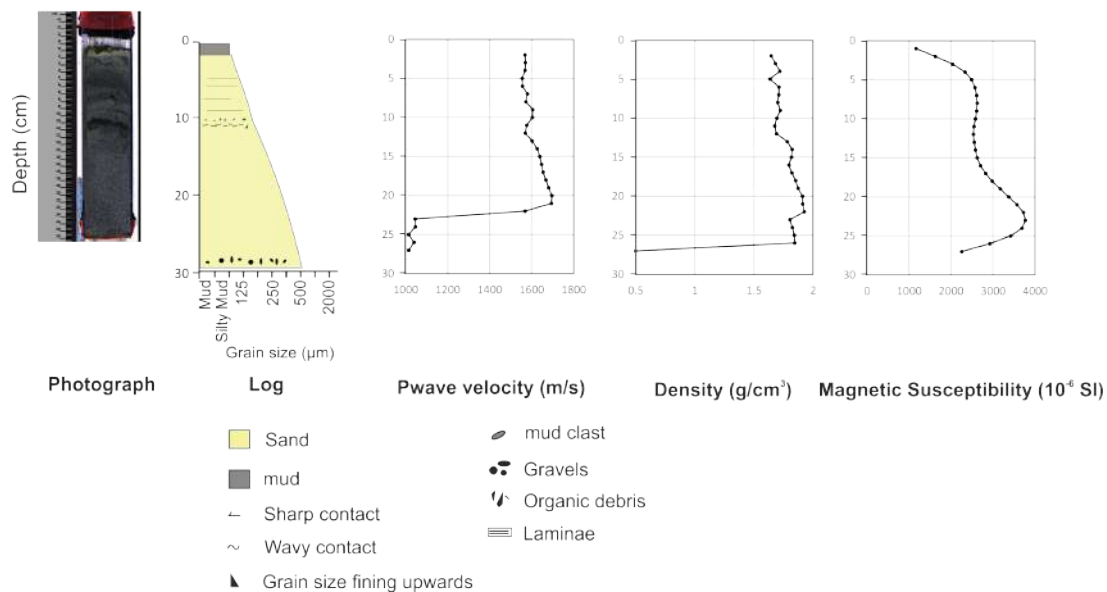


FIGURE A.12: Photograph, log and physical properties for box core 3 collected in Bute Inlet and presented in Chapter 4 (Fig. 4.1)

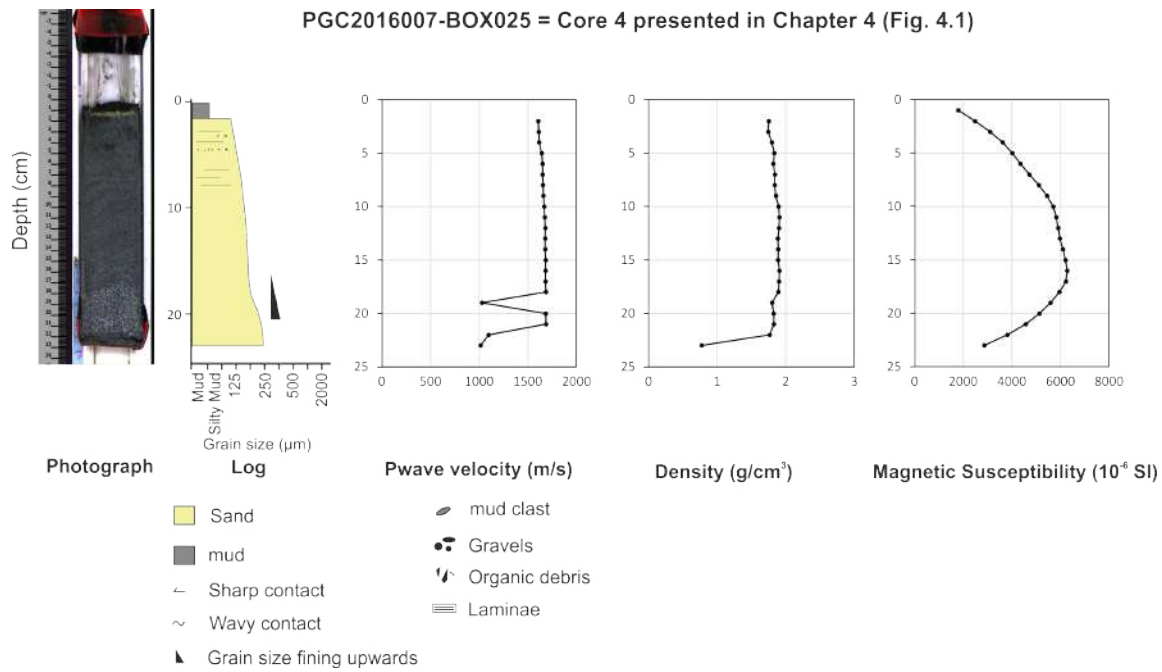


FIGURE A.13: Photograph, log and physical properties for box core 4 collected in Bute Inlet and presented in Chapter 4 (Fig. 4.1)

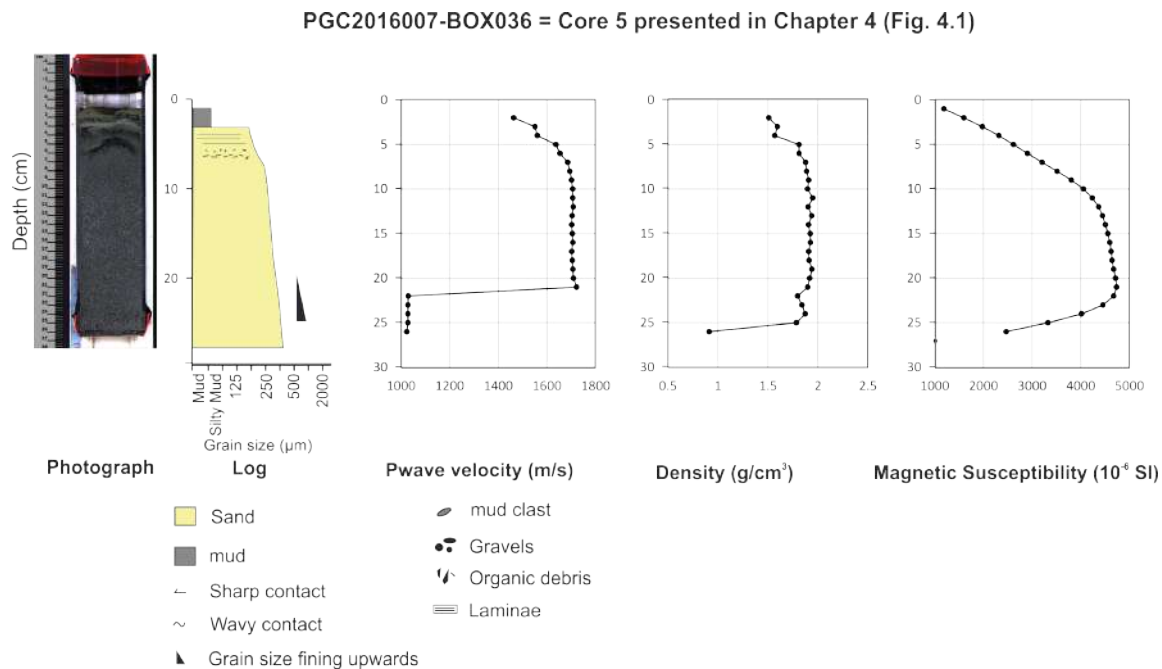


FIGURE A.14: Photograph, log and physical properties for box core 5 collected in Bute Inlet and presented in Chapter 4 (Fig. 4.1)

A.1.4 Bute Inlet October 2017 (Geological Survey of Canada cruise 2017005PGC)

A research cruise aboard the CCGS Vector enabled collection of sediment samples in the Homathko and Southgate rivers in order to characterize the composition of the sediment flushed into Bute Inlet. We sampled the river banks, the river deltas and the suspended sediment load through depth profiles (see sample locations in A.15). All samples were analysed for grain size and organic carbon in order to compare their composition with the sediment cores collected in the summer of 2016.

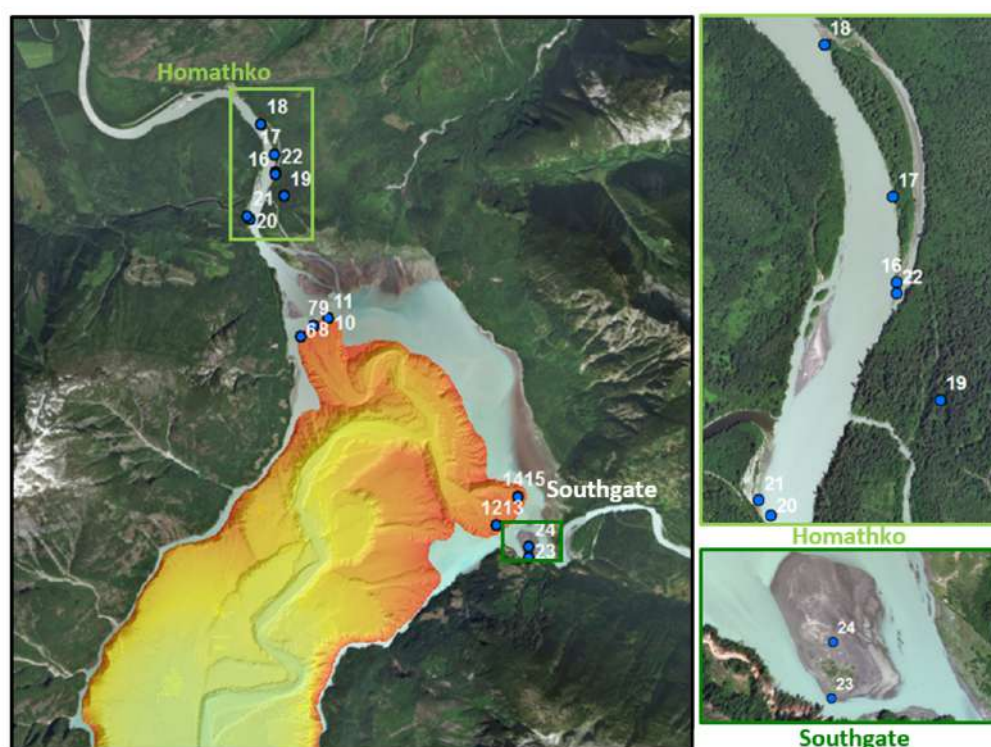


FIGURE A.15: Location maps for samples collected in Homathko and Southgate rivers in October 2017 and presented in Chapter 4

A.2 ADCP processing

A.2.1 General principle

ADCPs use the Doppler effect of sound waves reflected from particles in the water column to derive water current velocity (Teledyne, 2011). ADCPs contain a number of transducers (beams) that transmit and receive sound waves at a fixed frequency (Figure ??) . These reflected soundwaves enable derivation of the mean velocity of the particles at each vertical cell within the beams. The strength of the acoustic waves reflected from each cell, called echo intensity, can be correlated with suspended sediment concentration (see Appendix A3) under the assumption of a known and constant gran size. ADCP instruments can be upward-looking, i.e. settled on the seabed, or downward-looking, i.e. either mounted on a vessel or anchored in a mooring.

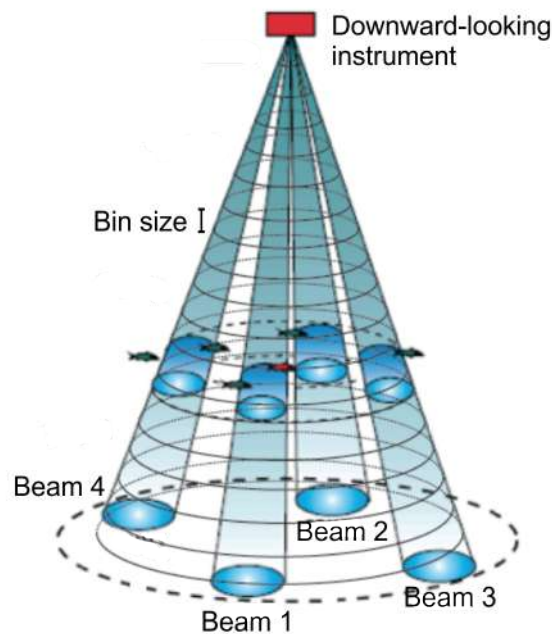


FIGURE A.16: schematic of an acoustic doppler current profiler (Teledyne, 2011)

All ADCPs used in the context of this thesis contain four downward-looking beams (30 m and 20 m above the seabed in Squamish and Bute Inlet respectively) fixed either from a vessel (in Squamish) or in a mooring buoy (in Bute). Velocity and echo intensity data collected by ADCPs in Squamish and Bute Inlet were first visualized into the software WinADCP. Text files were then exported from WinADCP in order to be imported into the Matlab software which enables easier data processing and visualisation of large matrices. The chart below (Figure ??) describes the steps used to process and visualize raw data from ADCPs based on a series of six matlab scripts written in conjunction with Maria Azpiroz-Zabala.

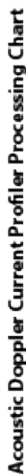


FIGURE A.17: Processing chart for acoustic doppler current profiler data (Maria Azpiroz-Zabala and Sophie Hage)

A.2.2 Limitations and corrections

Both Howe Sound and Bute Inlet are characterised by up to 5 m of tidal range (Water Survey of Canada, 2018), which resulted in the suspended ADCPs floating at variable distances from the seafloor. These fluctuations can clearly be seen on the seafloor which

is represented by the highest raw echo intensity (e.g. Figure ??a). A correction was applied to the ADCP data by adding to each matrix a number of vertical cells equals to the tidal amplitude at that time (Figure ??b).

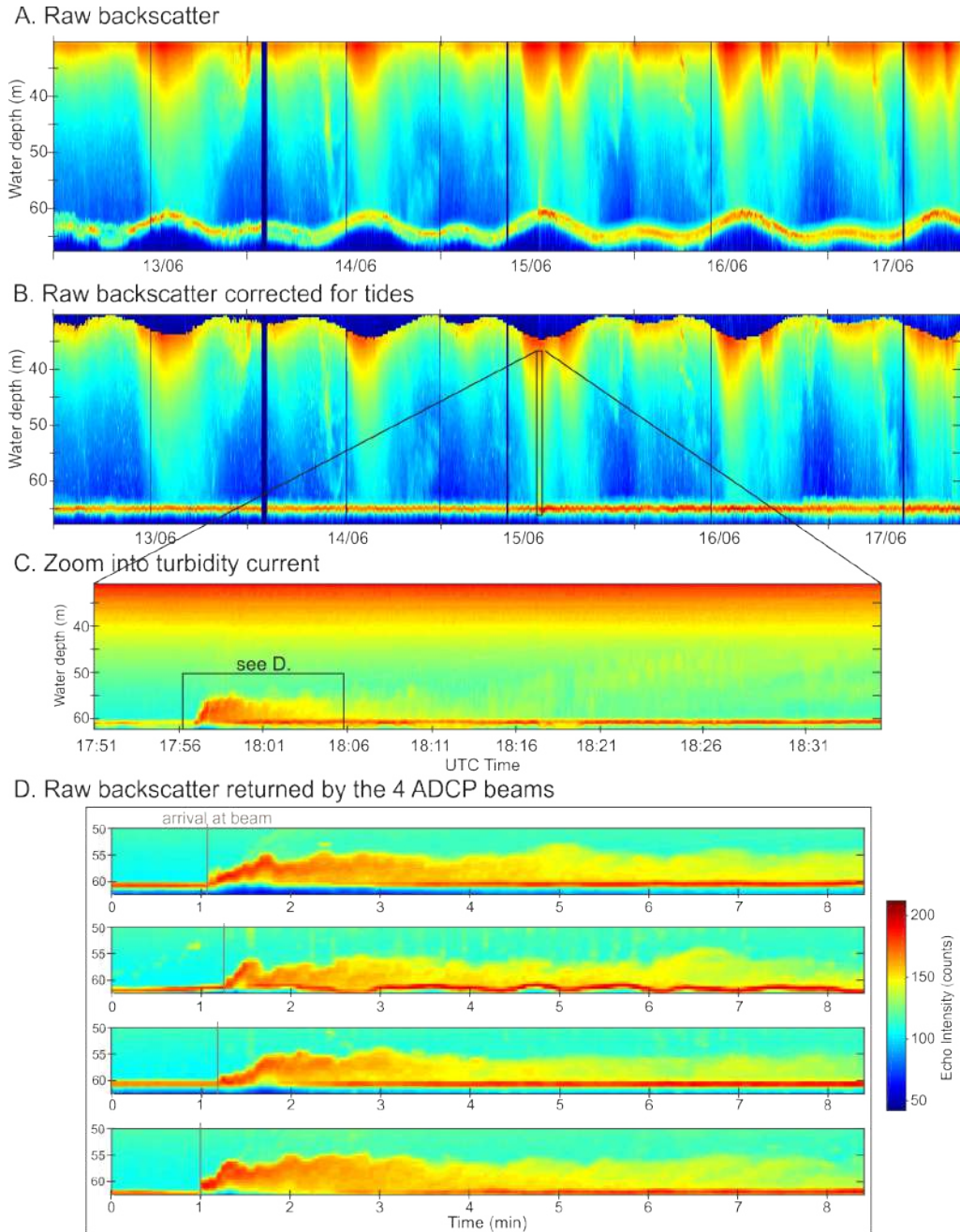


FIGURE A.18: Raw backscatter obtained by a 600 KHz ADCP in Squamish in June 2015. Backscatter is expressed in echo intensity counts **a**. Raw backscatter from 13th to 17th June. **b**. Raw backscatter from 13th to 17th June 2015. **c**. Zoom into the 15th June 2015 turbidity current (averaged backscatter between four ADCP beams). **d**. raw backscatter returned by the 4 ADCP beams during the 15th June turbidity current. Differential flow arrival time at each beam enables calculation of a front speed.

Another issue with ADCP is that the velocity is based on measurements provided by the four beams which can be spaced of several meters. For instance, the four beams

used in the Squamish 2015 deployment were spaced of 25 m on the seafloor as they were suspended 30 m above the seafloor with a 20° angle between them. The frontal velocity of the turbidity current monitored in Squamish could thus not be measured because the flow did not reach each beam at the same time. Difference in arrival time of the flow at each beam was thus used to derive the frontal flow velocity (Figure ??d).

ADCP performance is further limited by an effect called the side lobe interference, which occurs in the near-bed zone (Teledyne, 2011). This effect is due to the acoustic beams having side lobes that reflect from the seafloor before the main beam is reflected. The area influenced by the side lobe interference depends on the size of the beam and on the height above the seafloor at which the instrument is deployed. This effect was calculated for all data sets based on the instrument height and the vertical bin size. For example, the first meter above the seabed was ignored in the Squamish 2015 dataset.

A.2.3 Sediment concentration inversion

Echo intensity counts were inverted into suspended sediment concentrations for the Squamish 2015 deployment and are presented in chapter 2. The inversion method used is based on an implicit approach which involves two unknowns: the sediment concentration and the attenuation due to the sediment in the water column (Downing et al., 1995; Moate and Thorne, 2012).

A major assumption in this implicit method is that grain size distribution is uniform through the water column. Therefore, in order to better account for grain size patterns I used the implicit inversion separately for the background conditions and the turbidity current. I used a grain size distribution centred on 40 microns in background conditions and a grain size distribution centred on 200 microns within the turbidity current. These values are consistent with suspended sediment samples taken at the same time within the water column and the turbidity current.

A Matlab script following this method was written in collaboration with Age Vellinga and Maria Azpiroz-Zabala. Further inputs were provided by Stephen Simmons. The detailed steps of the inversion are described Appendix A3.

A.3 Procedure for ADCP implicit inversion into sediment concentration

The overall process of acoustic inversion is based on an implicit iterative approach and is governed by equations A1, A2 and A3. M is the sediment concentration (g/L) and α_s is the attenuation due to the sediment in the water. Once the iterative process for which $\alpha_{n=0} = \alpha_w$ reaches a convergent state, a value for M is obtained.

$$M = \left\{ \frac{V_{\text{rms}} \phi^r}{k_s k_t} \right\}^2 e^{4r \alpha} \quad (\text{A.1})$$

$$\alpha = \alpha_s + \alpha_w \quad (\text{A.2})$$

$$\alpha_s = \frac{1}{r} \int_0^r \xi(r) M(r) dr \quad (\text{A.3})$$

In order to complete this loop, a series of parameters needs to be specified as described in the following sections.

A.3.1 Raw backscatter to voltage V

Echo counts of the ADCP backscatter are converted into a voltage following (Deines, 1999):

$$V = 10^{K_c (E - E_r)/10} \quad (\text{A.4})$$

where:

E is the echo in counts

E_r is the noise level, set at a value of 40

K_c is an instrument-specific parameter set at 0.4241

A.3.2 Range to the transceiver r

The distance between the instrument transceiver and the middle of each ADCP bin (cell) needs to be corrected because the four ADCP beams are slanted at a 20° angle (Figure ??), following:

$$r = \frac{r_1 + n * \text{binsize}}{\cos(20\pi/180)} \quad (\text{A.5})$$

where:

r is the distance of the middle of each bin to the transceiver

r_1 is the mean distance of the first bin to the transceiver

n is the total number of bins

A.3.3 Near-field correction factor ϕ

The field near the transducer needs to be corrected for non-spherical spreading of the particles ϕ , following (Downing et al., 1995):

$$\lambda = \frac{c}{f} \quad (\text{A.6})$$

$$r_n = \frac{\pi * a_t^2}{\lambda} \quad (\text{A.7})$$

$$z = \frac{r}{r_n} \quad (\text{A.8})$$

$$\phi = \frac{1 + 1.35z + (2.5z)^{3.2}}{1.35z + (2.5z)^{3.2}} \quad (\text{A.9})$$

where:

λ is the sound wavelength

f is the sound frequency

z is the normalised range dependance

A.3.4 Backscatter properties of sediment K_s

K_s is the backscatter property of the suspended sediment, which is function of sediment grain-size and distribution.

A.3.4.1 Creation of a normalised frequency distribution of grain size diameter f

A normalised frequency distribution of grain size diameter (f) is computed based on the D_{50} and the standard deviation of samples.

First we need to define the absolute standard deviation Dev_{Abs} based on the relative standard deviation Dev_{Rel} and the grain size median D_{50} .

$$Dev_{Abs} = Dev_{Rel} * D_{50} \quad (A.10)$$

Second, we create D_p i.e. the assigned particle diameter based on the minimum and maximum grain size:

$$D_p = d_{min} + (d_{max} - d_{min}) \quad (A.11)$$

Third, we create a log-normal distribution of grain sizes:

$$\omega = \sqrt{\log(Dev_{Rel}^2 + 1)} \quad (A.12)$$

$$m_o = \sqrt{\log\left(\frac{D_{50}^2}{D_{50}^2 + Dev_{Abs}^2}\right)} \quad (A.13)$$

$$dNd = \sqrt{\frac{1}{D_p * 2\pi\omega} e^{-\log(D_p - m_o)^2 / 2\omega^2}} \quad (A.14)$$

Finally, the normalised frequency distribution of grain size with diameter D_p is created:

$$f = \frac{dNd}{\sum dNd} \quad (A.15)$$

A.3.4.2 Creation of a form function and scattering cross-section for all grain sizes ffa

Below we compute ffa i.e. the scattering cross-section for all grain sizes (Moate and Thorne, 2012):

$$ffa = \frac{\sum(f * a) \sum(f * a^2 * f f^2)^{0.5}}{\sum(f * a^3)} \quad (A.16)$$

where:

a is the grain radius

f is the normalised frequency distribution of grain size

ff is the form function calculated as follows:

$$ff = \frac{(1 - d_1 e^{\frac{x-d_2^2}{d_3}})(1 + d_4 e^{\frac{x-d_5^2}{d_6}})(1 + d_7 e^{\frac{x-d_8^2}{d_9}})x^2}{d_{10} + d_{11}x^2} \quad (\text{A.17})$$

where:

d_1 to d_{11} are specific to each sand mineral esstimated in (Moate and Thorne, 2012)

$$x = \frac{2\pi}{\lambda}a \quad (\text{A.18})$$

A.3.5 Instrument-specific constant K_t

The K_t value is a calibration constant that is specific to each instrument. It is set at 7.7080*105

A.3.6 Attenuation of sound due to water α_t

The attenuation of sound due to water α_t is computed as follows (Francois and Garrison, 1982):

$$\alpha_w = \frac{A_1 f_1 f r^2}{f_1^2 f r^2} + \frac{A_2 f_2 f r^2}{f_2^2 f r^2} + A_3 P_3 f r^2 \quad (\text{A.19})$$

where:

$$A_1 = 1.03 * 10^{-8} + 2.36 * 10^{-10}T - 5.22 * 10^{-12}T^2 = 1.11 * 10^{-8} \quad (\text{A.20})$$

$$A_2 = 5.62 * 10^{-8} + 7.52 * 10^{-10}T = 5.9 * 10^{-8} \quad (\text{A.21})$$

$$A_3 = (55.9 - 2.37T + 4.77 * 10^{-2}T^2 - 3.48 * 10^{-4}T^3) * 10^{-15} = 4.77 * 10^{-14} \quad (\text{A.22})$$

$$f_1 = 1.32 * 10^3 (T + 273.1) e^{\frac{-1700}{T+273.1}} = 787 \quad (\text{A.23})$$

$$f_1 = 1.55 * 10^7 (T + 273.1) e^{\frac{-3052}{T+273.1}} = 7.00 * 10^4 \quad (\text{A.24})$$

$$P_2 = 1 - 10.3 * 10^{-4} P + 3.7 * 10^{-7} P^2 = 0.82 \quad (\text{A.25})$$

$$P_3 = 1 - 3.84 * 10^{-4} P + 7.57 * 10^{-8} P^2 = 0.93 \quad (\text{A.26})$$

where:

T is the water temperature

P is the water pressure

fr is the instrument frequency

A.3.7 Attenuation constant ξ

The attenuation constant ξ needs to be determined in order to obtain α_s (see equation A.3). ξ corresponds to the sum of the viscous absorption of the sound wave by the sediment ξ_{viscous} and the scattering ξ_{scatter} :

$$\xi = \xi_{\text{viscous}} + \xi_{\text{scatter}} \quad (\text{A.27})$$

A.3.7.1 calculation of ξ_{viscous}

ξ_{viscous} is calculated as follows (Urick, 1948):

$$\xi_{\text{viscous}} = \sum \left[\frac{k_\alpha}{2\rho s} * \frac{s}{s^2 + (\sigma + \tau)^2} \right] \quad (\text{A.28})$$

where:

$$s = \frac{9}{4} \left(\frac{1}{\beta a} \right) \left(1 + \frac{1}{\beta a} \right) \quad (\text{A.29})$$

$$k_{\alpha} = 0.18 \quad (\text{A.30})$$

$$\tau = \frac{1}{2} + \frac{9}{4} \left(\frac{1}{\beta a} \right) \quad (\text{A.31})$$

$$\beta = \sqrt{\pi * \frac{fr}{1.52 * 10^{-6}}} \quad (\text{A.32})$$

A.3.7.2 calculation of ξ_{scatter}

ξ_{scatter} is calculated as follows:

$$\xi_{\text{scatter}} = \frac{3\chi}{4\alpha\rho_s} \quad (\text{A.33})$$

where:

$$\chi = \frac{\sum(f * a) \sum(f * a^2 * xx)}{\sum(f * a^3)} \quad (\text{A.34})$$

$$xx = \frac{\rho_{\text{sed}} * 0.09 * x^4}{1380 + 560x^2 + 150x^4} \quad (\text{A.35})$$

where:

f is the fraction of grain particles

ρ is the sediment density

Bibliography

- Allen, G., Salomon, J., Bassoullet, P., Du Penhoat, Y. and De Grandpre, C. (1980), ‘Effects of tides on mixing and suspended sediment transport in macrotidal estuaries’, *Sedimentary Geology* **26**(1-3), 69–90.
URL: [https://doi.org/10.1016/0037-0738\(80\)90006-8](https://doi.org/10.1016/0037-0738(80)90006-8)
- Ayranci, K. D., Lintern, G., Hill, P. R. and Dashtgard, S. (2012), ‘Tide-supported gravity flows on the upper delta front, fraser river delta, canada’, *Marine Geology* **326-328**, 166–170.
URL: <https://doi.org/10.1016/j.margeo.2012.09.007>
- Azpiroz-Zabala, M., Cartigny, M. J. B., Talling, P. J., Parsons, D. R., Sumner, E. J., Clare, M. A., Simmons, S. M., Cooper, C. and Pope, E. L. (2017), ‘Newly recognized turbidity current structure can explain prolonged flushing of submarine canyons’, *Science Advances* **3**(e1700200).
URL: <http://dx.doi.org/10.1126/sciadv.1700200>
- Babonneau, N. (2002), Mode de fonctionnement d’un chenal turbiditique méandrique : Cas du Système Turbiditique Actuel du Zaïre, Thesis.
- Bain, H. and Hubbard, S. M. (2016), ‘Stratigraphic evolution of a long-lived submarine channel system in the late cretaceous nanaimo group, british columbia, canada’, *Sedimentary Geology* **337**, 113–132.
URL: <https://doi.org/10.1016/j.sedgeo.2016.03.010>
- Berner, R. A. (1982), ‘Burial of organic carbon and pyrite sulfur in the modern ocean: its geochemical and environmental significance.’, *American Journal of Science* **282**, 451–473.
URL: <https://doi.org/10.2475/ajs.282.4.451>
- Biscara, L., Mulder, T., Martinez, P., Baudin, F., Etcheber, H., Jouanneau, J.-M. and Garlan, T. (2011), ‘Transport of terrestrial organic matter in the ogoué deep sea turbidite system (gabon)’, *Marine and Petroleum Geology* **28**, 1061–1072.
URL: <https://doi.org/10.1016/j.marpetgeo.2010.12.002>

- Blair, N. L. and Aller, R. C. (2012), 'The fate of terrestrial organic carbon in the marine environment', *Annual Review of Marine Science* **4**, 401–423.
URL: <https://doi.org/10.1146/annurev-marine-120709-142717>
- Bornhold, B., Ren, P. and Prior, D. (1994), 'High-frequency turbidity currents in british columbia fjords', *Geo-Marine Letters* **14**, 238–243.
URL: <https://doi.org/10.1007/BF01274059>
- Bouma, A. (1962), 'Sedimentology of some flysch deposits: A graphic approach to facies interpretation.', *Elsevier, Amsterdam/New York* p. 168 pp.
- Bouma, A. H., Normark, W. R. and Barnes, N. E. (2012), *Submarine Fans and Related Turbidite Systems*.
URL: <https://doi.org/10.1007/978-1-4612-5114-91>
- Bowen, A. J., Normark, W. and Piper, D. (1984), 'Modelling on turbidity currents on navy submarine fan, california continental borderland', *Sedimentology* **31**, 169–185.
URL: <https://doi.org/10.1111/j.1365-3091.1984.tb01957.x>
- Brucker, S., Hughes Clarke, J. E., Beaudoin, J., Lessels, C., Czotter, K., Loschiavo, R., Iwanowska, K. and Hill, P. (2007), 'Monitoring flood-related change in bathymetry and sediment distribution over the squamish delta, howe sound, british columbia.'
- Buckley, J. R. (1977), The currents, winds and tides of Northern Howe Sound, Thesis.
- Burdige, D. J. (2007), 'Preservation of organic matter in marine sediments: controls, mechanisms, and an imbalance in sediment organic carbon budgets?', *Chemical Reviews* **107**, 467–485.
URL: <https://doi.org/10.1021/cr050347q>
- Cantero, M. I., Cantelli, A., Pirmez, C., Balachandar, S., Mohrig, D., Hickson, T. A., Yeh, T.-h., Naruse, H. and Parker, G. (2012), 'Emplacement of massive turbidites linked to extinction of turbulence in turbidity currents', *Nature Geoscience* **5**(1), 42.
URL: <https://doi.org/10.1038/ngeo1320>
- Carter, L., Gavey, R., Talling, P. and Li, J. T. (2014), 'Insights into submarine geohazards from breaks in subsea telecommunication cables.', *Oceanography* **27**(2), 58–67.
URL: <http://dx.doi.org/10.5670/oceanog.2014.40>
- Cartigny, M. J. B., Eggenhuisen, J. T., Hansen, E. W. M. and Postma, G. (2013), 'Concentration-dependent flow stratification in experimental high-density turbidity currents and their relevance to turbidite facies models', *Journal of Sedimentary Research* **83**(12), 1046–1064.
URL: <http://dx.doi.org/10.2110/jsr.2013.71>
- Cartigny, M. J. B., Postma, G., van den Berg, J. H. and Mastbergen, D. R. (2011), 'A comparative study of sediment waves and cyclic steps based on geometries, internal

- structures and numerical modeling', *Marine Geology* **280**(1–4), 40–56.
URL: <http://www.sciencedirect.com/science/article/pii/S0025322710003117>
- Cartigny, M. J. B., Ventra, D., Postma, G., van Den Berg, J. H. and Venditti, J. (2014), 'Morphodynamics and sedimentary structures of bedforms under supercritical-flow conditions: New insights from flume experiments', *Sedimentology* **61**(3), 712–748.
URL: <http://dx.doi.org/10.1111/sed.12076>
- Clare, M., Hughes Clarke, J., Talling, P., Cartigny, M. and Pratomo, D. (2016), 'Pre-conditioning and triggering of offshore slope failures and turbidity currents revealed by most detailed monitoring yet at a fjord-head delta', *Earth and Planetary Science Letters* **450**, 208–220.
URL: <https://doi.org/10.1016/j.epsl.2016.06.021>
- Clark, K. E., Malhi, Y., New, M., Hilton, R. G., West, A. J., Grocke, D. R., Bryant, C. L., Ascough, P. L. and Caceres, A. R. (2013), 'New views on “old” carbon in the amazon river: Insight from the source of organic carbon eroded from the peruvian andes', *Geochemistry, Geophysics, Geosystems* **14**(5), 1644–1659.
URL: <http://doi.org/10.1002/ggge.20122>
- Conway, K. W., Barrie, J. V., Picard, K. and Bornhold, B. D. (2012), 'Submarine channel evolution: active channels in fjords, british columbia, canada', *Geo-Marine Letters* **32**(4), 301–312.
URL: <https://doi.org/10.1007/s00367-012-0280-4>
- Covault, J. A., Kostic, S., Paull, C. K., Ryan, H. F., Fildani, A. and Talling, P. (2014), 'Submarine channel initiation, filling and maintenance from sea-floor geomorphology and morphodynamic modelling of cyclic steps', *Sedimentology* **61**(4), 1031–1054.
URL: <https://doi.org/10.1111/sed.12084>
- Covault, J. A., Kostic, S., Paull, C. K., Sylvester, Z. and Fildani, A. (2017), 'Cyclic steps and related supercritical bedforms: Building blocks of deep-water depositional systems, western north america', *Marine Geology* **393**, 4–20.
URL: <https://doi.org/10.1016/j.margeo.2016.12.009>
- Cui, X., Bianchi, T. S., Jaeger, J. M. and Smith, R. W. (2016), 'Biospheric and petrogenic organic carbon flux along southeast alaska', *Earth and Planetary Science Letters* **452**, 238–246.
URL: <http://dx.doi.org/10.1016/j.epsl.2016.08.002>
- Cui, X., Bianchi, T. S. and Savage, C. (2017), 'Erosion of modern terrestrial organic matter as a major component of sediments in fjords', *Geophysical Research Letters* **44**, 1457–1465.
URL: <http://dx.doi.org/10.1002/2016GL07226>

- Cui, X., Bianchi, T. S., Savage, C. and Smith, R. W. (2016), ‘Organic carbon burial in fjords: Terrestrial versus marine inputs’, *Earth and Planetary Science Letters* **451**, 40–51.
URL: <https://doi.org/10.1016/j.epsl.2016.07.003>
- Daly, R. A. (1936), ‘Origin of submarine canyons’, *American Journal of Science* (186), 401–420.
URL: <http://dx.doi.org/10.2475/ajs.s5-31.186.401>
- de Leeuw, J., Eggenhuisen, J. and Cartigny, M. (2016), ‘Morphodynamics of submarine channel inception revealed by new experimental approach’, *Nature Communications* **7**.
URL: <http://dx.doi.org/10.1038/ncomms10886>
- Deines, K. (1999), ‘Backscatter estimation using broadband acoustic doppler current profilers’.
- Dietrich, P., Ghienne, J.-F., Normandeau, A. and Lajeunesse, P. (2016), ‘Upslope-migrating bedforms in a proglacial sandur delta: Cyclic steps from river-derived underflows?’, *Journal of Sedimentary Research* **86**, 11–12.
URL: <http://dx.doi.org/10.2110/jsr.2016.4>
- Douillet, G. A., Kueppers, U., Mato, C., Chaffaut, Q., Bouysson, M., Reschetizka, R., Hoelscher, I., Witting, P., Hess, K.-U. and Cerwenka, A. (2018), ‘Revisiting the lacquer peels method with pyroclastic deposits: sediment plates, a precise, fine scale imaging method and powerful outreach tool’, *Journal of applied volcanology* **7**(1), 11.
URL: <https://doi.org/10.1186/s13617-018-0080-2>
- Downing, A., Thorne, P. D. and Vincent, C. E. (1995), ‘Backscattering from a suspension in the near field of a piston transducer’, *Acoustic Society of America* **97**, 1614–1620.
URL: <https://doi.org/10.1121/1.412100>
- Dyer, K. (1997), *Estuaries: A Physical Introduction.*, New York, NY.
- Farrow, G., Syvitski, J. and Tunnecliffe, V. (1983), ‘Suspended particulate loading on the macro-benthos in a highly turbid fjord; knight inlet, british columbia.’, *Canadian Journal of Fisheries and Aquatic Science* **40**(1), 273–288.
URL: <https://doi.org/10.1139/f83-289>
- Fildani, A., Hubbard, S., Covault, J. A., Maier, K. L., Romanse, B. W., Traer, M. and Rowland, J. C. (2013), ‘Erosion at inception of deep-sea channels’, *Marine and Petroleum Geology* **41**, 48–61.
URL: <https://doi.org/10.1016/j.marpetgeo.2012.03.006>
- Fildani, A., Normark, W., Kostic, S. and Parker, G. (2006), ‘Channel formation by flow stripping: large-scale scour features along the monterey east channel and their relation

- to sediment waves', *Sedimentology* .
URL: <https://doi.org/10.1111/j.1365-3091.2006.00812.x>
- Forel, M. (1885), 'Ravins sous-lacustres des fleuves glaciaires', *C.R. Acad. Sci. Paris* **101**, 725–728.
- Francois, R. and Garrison, G. (1982), 'Sound absorption based on ocean measurements: Part i: pure water and magnesium sulfate contributions', *Journal of the Acoustical Society of America* **72**, 896–907.
URL: <https://doi.org/10.1121/1.388170>
- Gaillardet, J., Dupre, B., Louvat, P. and Allegre, C. A. (1999), 'Global silicate weathering and co₂ consumption rates deduced from the chemistry of large rivers.', *Chemical Geology* **159**, 3–30.
URL: [https://doi.org/10.1016/S0009-2541\(99\)00031-5](https://doi.org/10.1016/S0009-2541(99)00031-5)
- Gaines, S. M., Eglinton, G. and Rullkotter, J. (2009), *Echoes of life: what fossil molecules reveal about earth history*, Oxford University Press.
- Gales, J. A., Talling, P. J., Cartigny, M. J., Hughes Clarke, J., Lintern, G., Stacey, C. and Clare, M. A. (2019), 'What controls submarine channel development and the morphology of deltas entering deep-water fjords?', *Earth Surface Processes and Landforms* **44**(2), 535–551.
URL: <http://dx.doi.org/10.1002/esp.4515>
- Galy, V., Beyssac, O., France-Lanord, C. and Eglinton, T. I. (2008), 'Recycling of graphite during himalayan erosion: a geological stabilization of carbon in the crust', *Science* **322**, 943–945.
URL: <https://doi.org/10.1126/science.1161408>
- Galy, V., France-Lanord, C., Beyssac, O., Faure, P., Kudrass, H. and Palhol, F. (2007), 'Efficient organic carbon burial in the bengal fan sustained by the himalayan erosional system', *Nature* **450**(7168), 407–410. 10.1038/nature06273.
URL: <http://dx.doi.org/10.1038/nature06273>
- Galy, V. V., France-Lanord, C. and Lartiges, B. (2008), 'Loading and fate of particulate organic carbon from the himalaya to the ganga–brahmaputra delta', *Geochimica et Cosmochimica Acta* **72**, 1767–1787.
- Galy, V. V., Peucker-Ehrenbrink, B. and Eglinton, T. (2015), 'Global carbon export from the terrestrial biosphere controlled by erosion', *Nature Letter* **521**.
URL: <https://doi.org/10.1038/nature14400>
- Girardclos, S., Hilbe, M., Corella, J., Loizeau, J.-L., Kremer, K., Delsontro, T., Argantegui, A., Moscariello, A., Arlaud, F., Akhtman, Y., Anselmetti, F. and Lemmin, U. (2012), 'Searching the rhone delta channel in lake geneva since françois–alphonse forel.', *Archives Science* **65**, 103–118.

- Hage, S., Cartigny, M. J. B., Clare, M. A., Sumner, E. J., Vendettuoli, D., Hughes Clarke, J. E., Hubbard, S. M., Talling, P. J., Lintern, D. G., Stacey, C. D., Englert, R. G., Vardy, M. E., Hunt, J. E., Yokokawa, M., Parsons, D. R., Hizzett, J. L., Azpiroz-Zabala, M. and Vellinga, A. J. (2018), 'How to recognize crescentic bedforms formed by supercritical turbidity currents in the geologic record: Insights from active submarine channels', *Geology* **46**(6), 563–566. 10.1130/G40095.1.
URL: <http://dx.doi.org/10.1130/G40095.1>
- Hartnett, H. E., Keil, R. G., Hedges, J. I. and Devo, A. H. (1998), 'Influence of oxygen exposure time on organic carbon preservation in continental margin sediments', *Nature* **391**, 572–574.
URL: <https://doi.org/10.1038/35351>
- Hayes, J. M. and Waldbauer, J. R. (2006), 'The carbon cycle and associated redox processes through time', *Philosophical Transactions of the Royal Society B* **351**, 931–950.
URL: <https://doi.org/10.1098/rstb.2006.1840>
- Hemingway, J. D., Hilton, R. G., Hovius, N., Eglington, T. I., Haghipour, N., Wacker, L., Chen, M.-C. and Galy, V. V. (2018), 'Microbial oxidation of lithospheric organic carbon in rapidly eroding tropical mountain soils', *Science* **360**(6385), 209–212.
URL: <https://doi.org/10.1126/science.aao6463>
- Hemingway, J. D., Rothman, D., Rosengard, S. Z. and Galy, V. (2017), 'Technical note: An inverse method to relate organic carbon reactivity to isotope composition from serial oxidation', *Biogeosciences* **14**, 5099–5114.
URL: <http://hdl.handle.net/1721.1/115260>
- Hemingway, J., Rothman, D., Grant, K., Rosengard, S., Eglington, T., Derry, L. and Galy, V. (2019), 'Mineral protection regulates the long-term global preservation of natural organic carbon', *Nature* **570**.
URL: <https://doi.org/10.1038/s41586-019-1280-6>
- Hickin, J. E. (1989), 'Contemporary squamish river sediment flux to howe sound, british columbia', *Canadian Journal of Earth Sciences* **26**, 1953–1963.
URL: <https://doi.org/10.1139/e89-165>
- Hilton, R. G., Galy, A., Hovius, N., Kao, S.-K., Horng, M.-J. and Chen, H. (2012), 'Climatic and geomorphic controls on the erosion of terrestrial biomass from subtropical mountain forest', *Global Biogeochemical Cycles* **26**(GB3014).
URL: <https://doi.org/10.1029/2012GB004314>
- Hizzett, J. L., Hughes Clarke, J. E., Sumner, E. J., Cartigny, M. J. B., Talling, P. J. and Clare, M. A. (2018), 'Which triggers produce the most erosive, frequent, and longest runout turbidity currents on deltas?', *Geophysical Research Letters* **45**, 855–863.
URL: <https://doi.org/10.1002/2017GL075751>

Hoyal, D., Bursik, M. and Atkinson, J. (1999a), ‘Settling-driven convection: A mechanism of sedimentation from stratified fluids’, *Journal of Geophysical Research* **104**, 7952–7966.

URL: <https://doi.org/10.1029/1998JC900065>

Hoyal, D. C. J. D., Bursik, M. I. and Atkinson, J. (1999b), ‘The influence of diffusive convection on sedimentation from buoyant plumes’, *marine geology* **159**.

URL: [https://doi.org/10.1016/S0025-3227\(99\)00005-5](https://doi.org/10.1016/S0025-3227(99)00005-5)

Hubbard, S. M., Covault, J. A., Fildani, A. and Romans, B. W. (2014), ‘Sediment transfer and deposition in slope channels: Deciphering the record of enigmatic deep-sea processes from outcrop’, *Geological Society of America Bulletin* **126**(5/6), 857–871.

URL: <https://doi.org/10.1130/B30996.1>

Hughes Clarke, J., Brucker, S., Muggah, J., Hamilton, T., Cartwright, D., Church, I. and Kuus, P. (2012), ‘Temporal progression and spatial extent of mass wasting events on the squamish prodelta slope’.

Hughes Clarke, J. E. (2016), ‘First wide-angle view of channelized turbidity currents links migrating cyclic steps to flow characteristics’, *Nature Communications* **7**.

URL: <http://dx.doi.org/10.1038/ncomms11896>

Hughes Clarke, J., Vidiera Marques, C., and Pratomo, D. (2014), ‘Imaging active mass-wasting and sediment flows on a fjord delta, squamish, british columbia’, *Submarine Mass Movements and Their Consequences, Advances in Natural and Technological Hazards Research* **37**.

Hunt, J. E., Wynn, R. B., Masson, D. G., Talling, P. J. and Teagle, D. A. (2011), ‘Sedimentological and geochemical evidence for multistage failure of volcanic island landslides: A case study from icod landslide on north tenerife, canary islands’, *Geochemistry, Geophysics, Geosystems* **12**(12).

URL: <http://dx.doi.org/10.1029/2011GC003740>

Hunt, J. E., Wynn, R. B., Talling, P. J. and Masson, D. G. (2013), ‘Frequency and timing of landslide-triggered turbidity currents within the agadir basin, offshore nw africa: Are there associations with climate change, sea level change and slope sedimentation rates?’, *Marine Geology* **346**, 274–291.

URL: <https://doi.org/10.1016/j.margeo.2013.09.004>

Hurther, D., Thorne, P. D., Bricault, M., Lemmin, U. and Barnoud, J.-M. (2011), ‘A multi-frequency acoustic concentration and velocity profiler (acvp) for boundary layer measurements of fine-scale flow and sediment transport processes’, *Coastal Engineering* **58**(7), 594–605.

URL: <https://doi.org/10.1016/j.coastaleng.2011.01.006>

- Inman, D. L., Nordstrom, C. E. and Flick, R. E. (1976), 'Currents in submarine canyons: An air-sea-land interaction', *Annual Review of Fluid Mechanics* **8**(1), 275–310.
URL: <http://dx.doi.org/10.1146/annurev.fl.08.010176.001423>
- Jambeck, J. R., Geyer, R., Wilcox, C., Siegler, T. R., Perryman, M., Andrady, A., Narayan, R. and Law, K. L. (2015), 'Plastic waste inputs from land into the ocean', *Science* **347**(6223), 768–771.
URL: <http://dx.doi.org/10.1126/science.1260352>
- Jazi, S. D. and Wells, M. (2016), 'Enhanced sedimentation beneath particle-laden flows in lakes and the ocean due to double-diffusive convection', *Geophysical Research Letters* **43**, **1**(10), 10,883–10,890.
URL: <http://doi.org/10.1002/2016GL069547>
- Kane, I. A. and Clare, M. A. (2019), 'Dispersion, accumulation, and the ultimate fate of microplastics in deep-marine environments: A review and future directions', *Frontiers in Earth Science* **7**(80).
URL: <https://www.frontiersin.org/article/10.3389/feart.2019.00080>
- Kane, I. and Hodgson, M. (2015), 'Supercritical-flow structures on a late carboniferous delta front: Sedimentologic and paleoclimatic significance', *Geology (comment)* **43**, e374.
URL: <https://dx.doi.org/doi:10.1130/G37231C.1>
- Kao, S.-J., Hilton, R. G., Selvaraj, K., Dai, M., Zehetner, F., Huang, J.-C., Hsu, S.-C., Sparkes, R., Liu, J., Lee, T.-Y., Yang, J.-Y. T., Galy, A., Xu, X. and Hovius, N. (2014), 'Preservation of terrestrial organic carbon in marine sediments offshore taiwan: mountain building and atmospheric carbon dioxide sequestration', *Earth Surf. Dynam.* **2**, 127–139.
URL: <http://dx.doi.org/10.5194/esurf-2-127-2014>
- Keil, R. G., Mayer, L. M., Quay, P. D., Richey, J. E. and Hedges, J. I. (1997), 'Loss of organic matter from riverine particles in deltas', *Geochimica et Cosmochimica acta* **61**(7), 1507–1511.
URL: [https://doi.org/10.1016/S0016-7037\(97\)00044-6](https://doi.org/10.1016/S0016-7037(97)00044-6)
- Khripounoff, A., Crassous, P., Bue, N. L., Dennielou, B. and Jacinto, R. S. (2012), 'Different types of sediment gravity flows detected in the var submarine canyon (north-western mediterranean sea)', *Progress in Oceanography* **106**, 138–153.
URL: <http://dx.doi.org/10.1016/j.pocean.2012.09.001>
- Kineke, G. C., Sternberg, R. W., Geyer, W. R. and Trowbridge, J. H. (1995), 'Fluid-mud processes on the amazon continental shelf', *Continental Shelf Research* **16**.
URL: [https://doi.org/10.1016/0278-4343\(95\)00050-X](https://doi.org/10.1016/0278-4343(95)00050-X)

BIBLIOGRAPHY

- Kostic, S. (2011), 'Modeling of submarine cyclic steps: Controls on their formation, migration, and architecture', *Geosphere* **7**(2), 294–304.
URL: <https://doi.org/10.1130/GES00601.1>
- Kostic, S. and Parker, G. (2006), 'The response of turbidity currents to a canyon–fan transition: internal hydraulic jumps and depositional signatures', *Journal of Hydraulic Research* **44**, 631–653.
URL: <https://doi.org/10.1080/00221686.2006.9521713>
- Kuenen, P. (1950), 'Turbidity currents of high density: Report.'
- Lang, J., Brandes, C. and Winsemann, J. (2017), 'Erosion and deposition by supercritical density flows during channel avulsion and backfilling: Field examples from coarse-grained deepwater channel–levée complexes (sandino forearc basin, southern central america)', *Sedimentary Geology* **349**, 79–102.
URL: <https://doi.org/10.1016/j.sedgeo.2017.01.002>
- Lang, J. and Winsemann, J. (2013), 'Lateral and vertical facies relationships of bedforms deposited by aggrading supercritical flows: From cyclic steps to humpback dunes', *Sedimentary Geology* **296**, 36–54.
URL: <http://www.sciencedirect.com/science/article/pii/S0037073813001474>
- Lee, H., Galy, V., Fend, X., P., C., Galy, A., France-Lanord, C. and Feakins, S. (2019), 'Sustained wood burial in the bengal fan over the last 29 million years.', *Proceedings of the National Academy of Sciences of the United States of America* **116**(45), 22518–22525.
URL: <https://doi.org/10.1073/pnas.1913714116>
- Lintern, D. G., Hill, P. R. and Stacey, C. (2016), 'Powerful unconfined turbidity current captured by cabled observatory on the fraser river delta slope, british columbia, canada', *Sedimentology* **63**.
URL: <https://doi.org/10.1111/sed.12262>
- Liu, J. T., Kao, S.-J., Huh, C.-A. and Hung, C.-C. (2013), 'Gravity flows associated with flood events and carbon burial: Taiwan as instructional source area', *Annual Review of Marine Science* **5**, 47–68.
URL: <https://doi.org/10.1146/annurev-marine-121211-172307>
- Liu, J., Wang, Y.-H., Yang, R., Hsu, R., Kao, S.-J., Lin, H.-L. and Kuo, F. (2012), 'Cyclone induced hyperpycnal turbidity currents in a submarine canyon.', *Journal of Geophysical Research* **117**(C04033).
URL: <http://dx.doi.org/10.1029/2011JC007630>
- Lowe, D. R. (1982), 'Sediment gravity flows: Li depositional models with special reference to the deposits of high-density turbidity currents', *Journal of Sedimentary Research*

52(1).

URL: <https://doi.org/10.1306/212F7F31-2B24-11D7-8648000102C1865D>

Mayer, L. M. (1994), 'Relationships between mineral surfaces and organic carbon concentrations in soils and sediments', *Chemical Geology* **114**, 347–363.

URL: [https://doi.org/10.1016/0009-2541\(94\)90063-9](https://doi.org/10.1016/0009-2541(94)90063-9)

McArthur, A., Kneller, B., Wakefield, M., Souza, P. and Kuchle, J. (2016), 'Palynofacies classification of the depositional elements of confined turbidite systems: Examples from the gres d'annot, se france', *Marine and Petroleum Geology* **77**, 1254–1273.

URL: <http://dx.doi.org/10.1016/j.marpetgeo.2016.08.020>

McNichol, A., Jones, G., Hutton, D., Gagnon, A. and Key, R. (1994), 'The rapid preparation of seawater co2 for radiocarbon analysis at the national ocean sciences ams facility', *Radiocarbon* **36**(2), 237–246.

URL: <https://doi.org/10.1017/S0033822200040522>

McNichol, A., Osborne, E., Gagnon, A., Fry, B. and Jones, G. (1994), 'Tic, toc, dic, doc, pic, poc—unique aspects in the preparation of oceanographic samples for 14c-ams', *Nuclear Instruments and Methods in Physics Research Section B: Beam Interactions with Materials and Atoms* **92**(1-4), 162–165.

URL: [https://doi.org/10.1016/0168-583X\(94\)95998-6](https://doi.org/10.1016/0168-583X(94)95998-6)

Middleton, G. V. (1966), 'Experiments on density and turbidity currents: Ii. uniform flow of density currents.', *Canadian Journal of Earth Sciences* **3**, 627–637.

Middleton, G. V. and Hampton, M. A. (1973), 'Part i. sediment gravity flows: mechanics of flow and deposition', In *Turbidites and Deep Water Sedimentation, editions G. V. Middleton, A. H. Bouma, SEPM Pacific Section Short Course Notes Anaheim California: SEPM*, 38p.

Migeon, S., Mulder, T., Savoye, B. and Sage, F. (2012), 'Hydrodynamic processes, velocity structure and stratification in natural turbidity currents: Results inferred from field data in the var turbidite system', *Sedimentary Geology* **245-246**, 48–62.

URL: <https://doi.org/10.1016/j.sedgeo.2011.12.007>

Migeon, S., Savoye, B., Zanellac, E., Mulder, T., Faugeres, J.-C. and Weber, O. (2001), 'Detailed seismic-reflection and sedimentary study of turbidite sediment waves on the var sedimentary ridge (se france): significance for sediment transport and deposition and for the mechanisms of sediment-wave construction', *Marine and Petroleum Geology* **18**, 179–208.

URL: [https://doi.org/10.1016/S0264-8172\(00\)00060-X](https://doi.org/10.1016/S0264-8172(00)00060-X)

Milliman, J. D. and Meade, R. H. (1983), 'World-wide delivery of river sediment to the oceans.', *The Journal of Geology* **91**(1), 1–21.

URL: <https://doi.org/10.1086/628741>

- Milliman, J. D. and Syvitski, P. (1992), 'Geomorphic/tectonic control of sediment discharge to the ocean: The importance of small mountainous rivers', *The Journal of Geology* **100**, 525–544.
URL: <https://doi.org/10.1086/629606>
- Moate, B. and Thorne, P. (2012), 'Interpreting acoustic backscatter from suspended sediments of different and mixed mineralogical composition', *Continental Shelf Research* **46**, 67–82.
- Moernaut, J., Van Daele, M., Heirman, K., Fontijn, K., Strasser, M., Pino, M., and De Batist, M. (2014), 'Lacustrine turbidites as a tool for quantitative earthquake reconstruction: New evidence for a variable rupture mode in south central chile.', *Journal of Geophysical Research* **119**, 1607–1633.
URL: <https://doi.org/10.1002/2013JB010738>
- Mulder, T. and Syvitski, J. P. M. (1995), 'Turbidity currents generated at river mouths during exceptional discharges to the world oceans', *Journal of Geology* **103**(3), 285.
URL: <https://doi.org/10.1086/629747>
- Mutti, E., Tinterri, R., Benevelli, G., di Biase, D. and Cavanna, G. (2003), 'Deltaic, mixed and turbidite sedimentation of ancient foreland basins', *Marine and Petroleum Geology* **20**, 733–755.
URL: <https://doi.org/10.1016/j.marpetgeo.2003.09.001>
- Normandeau, A., Lajeunesse, P., G Poiré, A. and Francus, P. (2016), 'Morphological expression of bedforms formed by supercritical sediment density flows in four fjord-lake deltas of the south-eastern canadian shield (eastern canada)', *Sedimentology* **63**(7), 2106–2129.
URL: <https://doi.org/10.1111/sed.12298>
- Normark, W. R. and Piper, D. J. (1972), 'Sediments and growth pattern of navy deep-sea fan, san clemente basin, california borderland', *The Journal of Geology* **80**(2), 198–223.
URL: <https://doi.org/10.1086/627725>
- Obelcz, J., Xu, K., Georgiou, I. Y., Maloney, J., Bentley, S. J. and Miner, M. D. (2017), 'Sub-decadal submarine landslides are important drivers of deltaic sediment flux: insights from the mississippi river delta front', *Geology* **45**(7), 703–706.
URL: <https://doi.org/10.1130/G38688.1>
- Ono, K. and Bjorklund, P. P. (2017), 'Froude supercritical flow bedforms in deepwater slope channels? field examples in conglomerates, sandstones and fine-grained deposits', *Sedimentology* **65**, 639–669.
URL: <https://doi.org/10.1111/sed.12396>

Parsons, J., Bush, J. and Syvitski, J. (2001), ‘Hyperpycnal plume formation from riverine outflows with small sediment concentrations’, *Sedimentology* **48**, 465–478.

URL: <https://doi.org/10.1046/j.1365-3091.2001.00384.x>

Paull, C., Caress, D., Ussler, W., Lundsten, E. and Meiner-Johnson, M. (2011), ‘High-resolution bathymetry of the axial channels within monterey and soquel submarine canyons, offshore central california’, *Geosphere* **7**(1077-1101).

URL: <https://doi.org/10.1130/GES00636.1>

Paull, C. K., Talling, P. J., Maier, K. L., Parsons, D., Xu, J., Caress, D. W., Gwiazda, R., Lundsten, E. M., Anderson, K., Barry, J. P., Chaffey, M., O’Reilly, T., Rosenberger, K. J., Gales, J. A., Kieft, B., McGann, M., Simmons, S. M., McCann, M., Sumner, E. J., Clare, M. A. and Cartigny, M. J. (2018), ‘Powerful turbidity currents driven by dense basal layers’, *Nature Communications* **9**(1), 4114.

URL: <https://doi.org/10.1038/s41467-018-06254-6>

Paull, C., Ussler, W., Greene, H., Keaten, R., Mitts, P. and Barry, J. (2002), ‘Caught in the act: the 20 december 2001 gravity flow event in monterey canyon’, *Geo-Marine Letters* **22**(4), 227–232.

URL: <https://doi.org/10.1007/s00367-003-0117-2>

Pham, C. K., Ramirez-Llodra, E., Alt, C. H., Amaro, T., Bergmann, M., Canals, M., Davies, J., Duineveld, G., Galgani, F. and Howell, K. L. (2014), ‘Marine litter distribution and density in european seas, from the shelves to deep basins’, *PloS one* **9**(4), e95839.

Pickard, G. L. and Giovando, L. (1960), ‘Some observations of turbidity currents in british columbia inlets’, *Limnology and Oceanography* **5**(2), 162–170.

URL: <https://doi.org/10.4319/lo.1960.5.2.0162>

Pickering, K. and Hilton, V. (1998), *Turbidite Systems of Southeast France: Application to Hydrocarbon Prospectivity*, Vallis Press.

URL: <https://books.google.co.uk/books?id=vWDwAAAAMAAJ>

Pierdomenico, M., Casalbore, D. and Chiocci, F. L. (2019), ‘Massive benthic litter funnelled to deep sea by flash-flood generated hyperpycnal flows’, *Scientific Reports* **9**(1), 5330.

URL: <https://doi.org/10.1038/s41598-019-41816-8>

Piper, D. J., Cochonat, P. and Morrison, M. L. (1999), ‘The sequence of events around the epicentre of the 1929 grand banks earthquake: initiation of debris flows and turbidity current inferred from sidescan sonar’, *Sedimentology* **46**(1), 79–97.

URL: <https://doi.org/10.1046/j.1365-3091.1999.00204.x>

- Piper, D. J. W. and Normark, W. R. (2009), 'Processes that initiate turbidity currents and their influence on turbidites : a marine geology perspective', *Journal of Sedimentary Research* **79**(6), 347–362.
URL: <https://doi.org/10.2110/jsr.2009.046>
- Piper, D. and Savoye, B. (1993), 'Processes of late quaternary turbidity-current flow and deposition on the var deep-sea fan, north-west mediterranean sea.', *Sedimentology* **40**, 557–582.
URL: <https://doi.org/10.1111/j.1365-3091.1993.tb01350.x>
- Ponce, J. J. and Carmona, N. (2011), 'Coarse-grained sediment waves in hyperpycnal clinof orm systems, miocene of the austral foreland basin, argentina', *Geology* **39**(8), 763–766.
URL: <https://doi.org/10.1130/G31939.1>
- Postma, G. and Cartigny, M. J. B. (2014), 'Supercritical and subcritical turbidity currents and their deposits:a synthesis', *Geology* **42**(11), 987–990.
URL: <https://doi.org/10.1130/G35957.1>
- Postma, G., Kleverlaan, K., Cartigny, M. J. B. and Mohrig, D. (2014), 'Recognition of cyclic steps in sandy and gravelly turbidite sequences, and consequences for the bouma facies model', *Sedimentology* **61**(7), 2268–2290.
URL: <https://doi.org/10.1111/sed.12135>
- Postma, G., Nemec, W. and Kleinspehn, K. L. (1988), 'Large floating clasts in turbidites: a mechanism for their emplacement', *Sedimentary geology* **58**(1), 47–61.
URL: [https://doi.org/10.1016/0037-0738\(88\)90005-X](https://doi.org/10.1016/0037-0738(88)90005-X)
- Prior, D. B., Bornhold, B. D. and Johns, M. W. (1986), 'Active sand transport along a fjord-bottom channel, bute inlet, british columbia', *Geology* **14**(7), 581–584.
URL: [https://doi.org/10.1130/0091-7613\(1986\)14%581:ASTAAF%2.0.CO;2](https://doi.org/10.1130/0091-7613(1986)14%581:ASTAAF%2.0.CO;2)
- Prior, D. B., Bornholdt, B. D., Wiseman, W. J. J. and Lowe, D. R. (1987), 'Turbidity current activity in a british columbia fjord', *Sciences, New Serie, American Association for the Advancement of Science* **237**(4820), 1330–1333.
URL: <http://www.jstor.org/stable/1700006>
- Prior, D. and Bornhold, B. (1984), 'Geomorphology of slope instability features; squamish harbour, howe sound, british columbia', *Geological Survey of Canada* .
- Reeder, M. S., Stow, D. A. and Rothwell, R. G. (2002), 'Late quaternary turbidite input into the east mediterranean basin: new radiocarbon constraints on climate and sea-level control', *Geological Society, London, Special Publications* **191**(1), 267–278.
URL: <https://doi.org/10.1144/GSL.SP.2002.191.01.18>

- Rosenheim, B. E., Day, M. B., Domack, E., Schrum, H., Benthien, A. and Hayes, J. M. (2008), 'Antarctic sediment chronology by programmed-temperature pyrolysis: Methodology and data treatment', *Geochemistry, Geophysics, Geosystems* **9**(4).
URL: <https://doi.org/10.1029/2007GC001816>
- Rothwell, R., Thomson, J. and Kähler, G. (1998), 'Low-sea-level emplacement of a very large late pleistocene 'megaturbidite' in the western mediterranean sea', *Nature* **392**(6674), 377.
URL: <https://doi.org/10.1038/32871>
- Saller, A., Lin, R. and Dunham, J. (2006), 'Leaves in turbidite sands: the main source of oil and gas in the deep-water kutei basin, indonesia.', *AAPG Bulletin* **90**(10), 1585–1608.
- Schnyder, J., Stetten, E., Baudin, F., Pruski, A. and Martinez, P. (2017), 'Palynofacies reveal fresh terrestrial organic matter inputs in the terminal lobes of the congo deep-sea fan', *Deep Sea Research II: Tropical studies in Oceanography* **142**, 91–208.
URL: <https://doi.org/10.1016/j.dsr2.2017.05.008>
- Shanmugam, G. (1980), 'Rhythms in deep sea, fine-grained turbidite and debris-flow sequences, middle ordovician, eastern tennessee', *Sedimentology* **27**(4), 419–432.
URL: <https://doi.org/10.1111/j.1365-3091.1980.tb01191.x>
- Smith, R. W., Bianchi, T. S., Allison, M., Savage, C. and Galy, V. (2015), 'High rates of organic carbon burial in fjord sediments globally', *Nature Geoscience* **8**.
URL: <https://doi.org/10.1038/ngeo2421>
- Sparkes, R. B., Lin, I.-T., Hovius, N., Galy, A., Liu, J. T., Xu, X. and Yang, R. (2015), 'Redistribution of multi-phase particulate organic carbon in a marine shelf and canyon system during an exceptional river flood: Effects of typhoon morakot on the gaoping river–canyon system', *Marine Geology* **363**, 191–201.
URL: <http://dx.doi.org/10.1016/j.margeo.2015.02.013>
- Spinewine, B., Sequeiros, O., Garcia, M., Beaubouef, R., Sun, T., Savoye, B. and Parker, G. (2009), 'Experiments on wedge-shaped deep sea sedimentary deposits in minibasins and/or on channel levees emplaced by turbidity currents part ii, morphodynamic evolution of the wedge and of the associated bedforms.', *Journal of sedimentary research* **79** (8), 608–628.
URL: <https://doi.org/10.2110/jsr.2009.065>
- Stacey, C. D., Hill, P. R., Talling, P. J., Enkin, R. J., Hughes Clarke, J. and Lintern, D. G. (2019), 'How turbidity current frequency and character varies down a fjord-delta system: Combining direct monitoring, deposits and seismic data', *Sedimentology* **66**(1), 1–31.
URL: <https://doi.org/10.1111/sed.12488>

- Stetten, E., Baudin, F., Reyss, J.-L., Martinez, P., Charlier, K., Schnyder, J., Rabouille, C., Dennielou, B., Coston-Guarini, J. and Pruski, A. (2015), 'Organic matter characterization and distribution in sediments of the terminal lobes of the congo deep-sea fan: evidence for the direct influence of the congo river.', *Marine Geology* **369**(182-195).
URL: <https://doi.org/10.1016/j.margeo.2015.08.020>
- Sumner, E. J., Amy, L. A. and Talling, P. J. (2008), 'Deposit structure and processes of sand deposition from decelerating sediment suspensions', *Journal of Sedimentary Research* **78**(8), 529–547.
URL: <https://doi.org/10.2110/jsr.2008.062>
- Sumner, E. J. and Paull, C. K. (2014), 'Swept away by a turbidity current in mendocino submarine canyon, california', *Geophysical Research Letters* **41**(21), 7611–7618.
URL: <http://dx.doi.org/10.1002/2014gl061863>
- Sumner, E. J., Talling, P. J., Amy, L. A., Wynn, R. B., Stevenson, C. J. and Frenz, M. (2012), 'Facies architecture of individual basin-plain turbidites: Comparison with existing models and implications for flow processes', *Sedimentology* **59**, 1850–1887.
URL: <https://doi.org/10.1111/j.1365-3091.2012.01329.x>
- Sun, T. and Parker, G. (2005), 'Transportational cyclic steps created by flow over an erodible bed. part 2. theory and numerical simulation', *Journal of Hydraulic Research* **43**(5), 502–514.
URL: <https://doi.org/10.1080/00221680509500148>
- Sutherland, B. R., Gingras, M., Knudson, C., Steverango, L. and Surma, C. (2018), 'Particle-bearing currents in uniform density and two-layer fluids.', *Physical Review Fluids* **3**(023801).
URL: <https://doi.org/10.1103/PhysRevFluids.3.023801>
- Symons, W. O., Sumner, E. J., Talling, P., Cartigny, M. J. and Clare, M. A. (2016), 'Large-scale sediment waves and scours on the modern seafloor and their implications for the prevalence of supercritical flow', *Marine geology* **371**, 130–148.
URL: <https://doi.org/10.1016/j.margeo.2015.11.009>
- Symons, W., Sumner, E. J., Paull, C. K., Cartigny, M. J. B., Xu, J., Maier, K. L., Lorenson, T. D. and J., T. P. (2017), 'A new model for turbidity current behavior based on integration of flow monitoring and precision coring in a submarine canyon', *Geology* .
URL: <https://doi.org/10.1130/G38764.1>
- Syvitski, J., Burrell, D. and Skei, J. (1987), *Fjords*, Springer-Verlag New York.
- Syvitski, J. P. M. and Murray, J. W. (1981), 'Particle interaction in fjord suspended sediment', *Marine Geology* **39**, 215–242.
URL: [https://doi.org/10.1016/0025-3227\(81\)90073-6](https://doi.org/10.1016/0025-3227(81)90073-6)

Syvitski, J. P. and Macdonald, R. D. (1982), 'Sediment character and provenance in a complex fjord; howe sound, british columbia', *Canadian Journal of Earth Sciences* **19**(5), 1025–1044.

URL: <https://doi.org/10.1139/cjes-2017-0223>

Talling, P. J. (2014), 'On the triggers, resulting flow types and frequencies of subaqueous sediment density flows in different settings', *Marine Geology* .

URL: <http://dx.doi.org/10.1016/j.margeo.2014.02.006>

Talling, P. J., Massin, Douglas, G., Sumner, E. J. and Malgesini, G. (2012), 'Subaqueous sediment density flows: Depositional processes and deposit types', *Sedimentology* **59**, 1937–2003.

URL: <https://doi.org/10.1111/j.1365-3091.2012.01353.x>

Talling, P., Wynn, R., Masson, D., Frenz, M., Cronin, B., Schiebel, R., Akhmetzhanov, A., Dallmeier-Tiessen, S., Benetti, S., Weaver, P., Georgiopoulou, A., Zühlsdorff, C. and Amy, L. (2007), 'Onset of submarine debris flow deposition far from original giant landslide', *Nature* **450**, 541–544.

URL: <https://doi.org/10.1038/nature06313>

Teledyne (2011), Acoustic doppler current profiler principles of operation a practical primer, Report.

Thorne, P. D. and Hurther, D. (2014), 'An overview on the use of backscattered sound for measuring suspended particle size and concentration profiles in non-cohesive inorganic sediment transport studies.', *Continental Shelf Research* **73**, 97–118.

URL: <https://doi.org/10.1016/j.csr.2013.10.017>

Thorne, P., Vincent, C., Hardcastle, P., Rehman, S. and Pearson, N. (1991), 'Measuring suspended sediment concentrations using acoustic backscatter devices', *Marine Geology* **98**(1), 7–16.

URL: [https://doi.org/10.1016/0025-3227\(91\)90031-X](https://doi.org/10.1016/0025-3227(91)90031-X)

Toniolo, H. and Cantelli, A. (2007), 'Experiments on upstream-migrating knickpoints', *Journal of Sedimentary Research* **77**, 772–783.

URL: <http://dx.doi.org/10.2110/jsr.2007.067>

Turowski, J., Badoux, A., Bunte, K., Rickli, C., Federspiel, N. and Jochner, M. (2013), 'The mass distribution of coarse particulate organic matter exported from an alpine headwater stream', *Earth Surface Dynamics* **1**, 1–11.

URL: <https://doi.org/10.5194/esurf-1-1-2013>

Turowski, J. M., Hilton, R. G. and Sparkes, R. (2016), 'Decadal carbon discharge by a mountain stream is dominated by coarse organic matter.', *Geology* **44**(1), 27–30.

URL: <http://doi.org/10.1130/G37192.1>

- Urick, R. (1948), 'The absorption of sound in suspensions of irregular particles', *The Journal of the Acoustical Society of America* **20**, 283–289.
URL: <https://doi.org/10.1121/1.1906373>
- Vellinga, A., Cartigny, M., Eggenhuisen, J. and Hansen, E. (2017), 'Morphodynamics and depositional signature of low-aggradation cyclic steps: New insights from a depth-resolved numerical model', *Sedimentology* **65**, 540–560.
URL: <https://doi.org/10.1111/sed.12391>
- Vendettuoli, D., Clare, M., Clarke, J. H., Vellinga, A., Hizzet, J., Hage, S., Cartigny, M., Talling, P., Waltham, D. and Hubbard, S. (2019), 'Daily bathymetric surveys document how stratigraphy is built and its extreme incompleteness in submarine channels', *Earth and Planetary Science Letters* **515**, 231–247.
URL: <https://doi.org/10.1016/j.epsl.2019.03.033>
- Ventra, D., Cartigny, M., Bijkerk, J. H. and Acikalin, S. (2015), 'Supercritical-flow structures on a late carboniferous delta front: Sedimentologic and paleoclimatic significance', *Geology* **43**, 731–734.
URL: <https://doi.org/10.1130/G36708.1>
- WaterSurveyCanada (2018), 'Historical hydrometric data'.
- Weimer, P. and Pettingill, H. (2007), 'A global overview of fields and discoveries in deep-water deposits.', In: *Atlas of Deepwater Outcrops* (Eds T. Nielsen, R.D. Shew, G.S. Steffens and J.R.J. Studlick), *AAPG Stud. Geol.* **56**, *Shell Exploration and Production and American Association of Petroleum Geologists*, 12–16. .
- West, A., Lin, C.-W., Lin, T.-C., Hilton, R., Liu, S.-H., Chang, C.-T., Lin, K.-C., Galy, A., Sparkes, R. and Hovius, N. (2011), 'Mobilization and transport of coarse woody debris to the oceans triggered by an extreme tropical storm', *Limnology and oceanography* **56**(1), 77–85.
URL: <https://doi.org/10.4319/lo.2011.56.1.0077>
- Wynn, R. B., Huvenne, V. A., Le Bas, T. P., Murton, B. J., Connelly, D. P., Bett, B. J., Ruhl, H. A., Morris, K. J., Peakall, J. and Parsons, D. R. (2014), 'Autonomous underwater vehicles (auvs): Their past, present and future contributions to the advancement of marine geoscience', *Marine Geology* **352**, 451–468.
URL: <https://doi.org/10.1016/j.margeo.2014.03.012>
- Xu, J., Barry, J. and Paull, C. (2013), 'Small-scale turbidity currents in a big submarine canyon', *Geology* **41**(2), 143–146.
URL: <http://dx.doi.org/10.1130/G33727.1>
- Xu, J., Noble, M. and Rosenfeld, L. (2004), 'In-situ measurements of velocity structure within turbidity currents', *Geophys. Res. Lett.* **31**.
URL: <http://doi.org/10.1029/2004GL019718>

Yokokawa, M., K., O., Nakamura, A., Muto, T., Miyata, Y., Naruse, H. and Parker, G. (2009), ‘Aggradational cyclic steps: Sedimentary structures found in flume experiments’, *Vancouver, Canada, Proceedings of the 33rd International Association for Hydro-Environment Engineering (IAHR) Congress* **81**, 5547–5554.

URL: <https://doi.org/10.1111/j.1365-3091.1991.tb00367.x>

Zavala, C., Arcuri, M. and Blanco Valiente, L. (2012), ‘The importance of plant remains as diagnostic criteria for the recognition of ancient hyperpycnites’, *Revue de Paléobiologie, Geneve* **11**, 457–469.

Zeng, J., Lowe, D., B., P. D., Wiseman, W. J. J. and Bornhold, B. (1991), ‘Flow properties of turbidity currents in bute inlet, british columbia’, *Sedimentology* **38**(6), 975–996.

URL: <https://doi.org/10.1111/j.1365-3091.1991.tb00367.x>